

Ultra-High Capacity Silicon Photonic Interconnects through Spatial Multiplexing

Christine P. Chen

Submitted in partial fulfillment of the
requirements for the degree
of Doctor of Philosophy
in the Graduate School of Arts and Sciences

COLUMBIA UNIVERSITY

2017

©2017

Christine P. Chen

All Rights Reserved

ABSTRACT

Ultra-High Capacity Silicon Photonic Interconnects through Spatial Multiplexing

Christine P. Chen

The market for higher data rate communication is driving the semiconductor industry to develop new techniques of writing at smaller scales, while continuing to scale bandwidth at low power consumption. The question arises of how to continue to sustain this trend.

Silicon photonic (SiPh) devices offer a potential solution to the electronic interconnect bandwidth bottleneck. SiPh leverages the technology commensurate of decades of fabrication development with the unique functionality of next-generation optical interconnects. Finer fabrication techniques have allowed for manufacturing physical characteristics of waveguide structures that can support multiple modes in a single waveguide. By refining modal characteristics in photonic waveguide structures, through mode multiplexing with the asymmetric y-junction and microring resonator, higher aggregate data bandwidth is demonstrated via various combinations of spatial multiplexing, broadening applications supported by the integrated platform.

The main contributions of this dissertation are summarized as follows. Experimental demonstrations of new forms of spatial multiplexing combined together exhibit feasibility of data transmission through mode-division multiplexing (MDM), mode-division and wavelength-division multiplexing (MDM-WDM), and mode-division and polarization-division multiplexing (MDM-PDM) through a C-band, Si photonic platform. Error-free operation through mode multiplexers and demultiplexers show how data can be viably scaled on multiple modes and with existing spatial domains simultaneously. This work opens up new avenues for scaling bandwidth capacity through leveraging orthogonal domains available on-chip, beyond what had previously been employed like WDM and time-division multiplexing (TDM).

Furthermore, we explore expanding device channel support from two to three arms. Finding that a slight mismatch in the third arm can increase crosstalk contributions considerably, especially when increasing data rate, we explore a methodical way to design the asymmetric y-junction device by considering its angles and multiplexer/demultiplexer arm width. By taking into consideration device fabrication variations, we turn towards optimizing device performance post-fabrication. Through ModePROP simulations, optimizing device performance dynamically post-fabrication is analyzed, through either electro-optical or thermo-optical means. By biasing the arm introducing the slight spectral offset, we can quantifiably improve device performance.

Scaling bandwidth is experimentally demonstrated through the device at 3 modes, 2 wavelengths, and 40 Gb/s data rate for 240 Gb/s aggregate bandwidth, with the potential to reduce power penalty per the device optimization process we described.

A main motivation for this on-chip spatial multiplexing is the need to reduce costs. As the laser source serves as the greatest power consumer in an optical system, mode-division multiplexing and other forms of spatial multiplexing can be implemented to push its potentially prohibitive cost metrics down. While the device introduces loss, through imperfect mode isolation, as device fabrication improves, tolerance can increase as well. Meanwhile, the rate that laser power consumption increases as supported wavelengths scales is shown to be much faster than the loss introduced by scaling on-chip bandwidth multimodally.

Future generations of ultra-high capacity devices through spatial multiplexing is explored. Already various systems can be implemented multimodally, with the design features serving as useful for other components. Central to photonic network-on-chips, a multimodal switch fabric, composed of microring resonators, is demonstrated to have error-free operation of 1x2 switching of 10 Gb/s data.

These contributions aim to scale bandwidth to ultra-high capacity, while ameliorating any imperfect design, through multiple routes conjoined with on-chip spatial multiplexing, and they constitute the bulk of this dissertation. For the latter part, we turn to the issue of integrating a photonic device for dynamic power reallocation in a system. Specifically, we utilize a 4x4 nonblocking switch fabric composed of Mach-Zehnder interferometers that

switch both electro-optically and thermo-optically at ns and μ s rates respectively.

In order to demonstrate an intelligent platform capable of dynamically multicasting data and reallocating power as needed by the system, we must first initialize the switch fabric to control with an electronic interface. A dithering mechanism, whereby exact cross, bar, and sub-percentage states are enforced through the device, is described here. Such a method could be employed for actuating the device table of bias values to states automatically. We then employ a dynamic power reallocation algorithm through a data acquisition unit, showing real-time channel recovery for channels experiencing power loss by diverting power from paths that could tolerate it. The data that is being multicast through the system is experimentally shown to be error-free at 40 Gb/s data rate, when transmitting from one to three clients and going from automatic bar/cross states to equalized power distribution.

For the last portion of this topic, the switch fabric was inserted into a high-performance computing system. In order to run benchmarks at 10 Gb/s data on top of the switch fabric, a newer model of the control plane was implemented to toggle states according to the command issued by the server. Such a programmable mechanism will prove necessary in future implementations of optical subsystems embedded inside larger systems, like data centers. Beyond the specific control plane demonstrated, the idea of an intelligent photonic layer can be applied to alleviate many kinds of optical channel abnormalities or accommodate for switching based on different patterns in data transmission.

Besides spatial-multiplexing, expanding on-chip bandwidth can be accomplished by extension of the wavelength detection regime to a longer regime. Experimental demonstration of photodetection at 1.9 μ m is shown with Si⁺-doped Si photodetectors at 1 Gb/s data operation featuring responsivities of .03 AW⁻¹ at 5 V bias. The same way of processing these Si ribbed waveguide photodetectors can garner even longer wavelength operation at 2.2 μ m wavelength.

Finally, the experimental demonstration of a coherent perfect absorption Si modulator is exhibited, showing a viable extinction ratio of 24.5 dB. Using this coherent perfect absorption mechanism to demodulate signals, there is the added benefit of differential reception. Currently, an automated process for data collection is employed at a faster time scale than instabilities present in fibers in the setup with future implementations eliminating the

off-chip phase modulator for greater signal stability.

The field of SiPh has developed to a stage where specific application domains can take off and compete according to industrial-level standards. The work in this dissertation contributes to experimental demonstration of a newly developing area of mode-division multiplexing for substantially increasing bandwidth on-chip. While implementing the discussed photonic devices in dynamic systems, various attributes of integrated photonics are leveraged with existing electronic technologies. Future generations of computing systems should then be designed by implementing both system and device level considerations.

Table of Contents

List of Figures	v
1 Introduction	1
1.1 Next Generation Optical Interconnects	1
1.1.1 Silicon Photonics	1
1.2 Integrated Photonic Link	2
1.2.1 Lasing Sources	3
1.2.2 Modulating Data	3
1.2.3 Photodetector	4
1.3 Spatial Multiplexing	4
1.3.1 Increasing Bandwidth: Telecommunications and PICs	4
1.4 Control Plane	6
1.5 Focus of Work	8
I On-Chip Spatial Multiplexing	10
2 Device Design of Multimode Waveguide	11
2.1 Background	11
2.1.1 Mode Multiplexing and Demultiplexing Designs	12
2.2 Asymmetric Y-junctions for Mode Multiplexer/ Demultiplexer	13
2.2.1 Theory for Multimode Support	13
2.2.2 Theory Extended to Three Modes	15
2.2.3 Device Fabrication	17

2.2.4	Three Mode Supporting Device	20
2.3	Microring Resonator for Mode Multiplexer/Demultiplexer	20
2.3.1	Background: Optical Resonators	20
2.3.2	Theory for Multimode Support	21
2.3.3	Design of the MM Regime	22
2.3.4	MDM System	22
2.4	Main Takeaways	23
3	Spatial Multiplexing for Ultra-high Bandwidth	24
3.1	Enabling Mode-division Multiplexing (MDM)	24
3.1.1	Experimental Setup	24
3.1.2	System Considerations	26
3.1.3	Data Results	26
3.2	MDM-WDM	28
3.2.1	Experimental Setup	28
3.2.2	Data Results	28
3.2.3	Discussion	29
3.3	MDM-PDM	29
3.3.1	Experimental Setup	30
3.3.2	Data Results	32
3.3.3	Simulations	33
3.4	Main Takeaways	34
4	Scaling MDM Capacity	35
4.1	Scaling MDM channels	35
4.1.1	Three Modes	36
4.1.2	Alleviating Imperfection in Multimode Device	37
4.1.3	Accuracy of Fabrication	40
4.1.4	Discussion of Need for Dynamic Adjustment	41
4.1.5	Introduce Variation in Arm vs. Multimode Regime	41
4.1.6	Thermo-optic Control for Three Modes	42

4.2	Scaling Capacity	45
4.3	Multimode Data Distribution via a Switch Fabric	48
4.4	Coupling and Packaging Considerations	50
4.4.1	Thermal Variations	51
4.5	Main Takeaways	53
5	Power Saving Analysis	55
5.1	Power Analysis in Optical System	55
5.2	Laser Power Analysis for MDM/PDM Channel Addition	56
5.3	Main Takeaways	59
II	Si Photonic Subsystems	61
6	Optical Network Architecture	62
6.1	The Optical Switch	62
6.1.1	2x2 MZI Switch	63
6.1.2	2x2 Switch Layout and Results	64
6.2	4x4 Switch Element	65
6.2.1	Initialization	65
6.2.2	Discussion of Non-Blocking Topology	66
6.3	Intelligent Power Algorithm for Power Reallocation	67
6.3.1	Control Plane for Demonstration of Power Equalization	68
6.3.2	Experimental Setup	70
6.3.3	Algorithmic Implementation	71
6.3.4	Demonstration of Dynamic Reconfiguration	75
6.3.5	Simulation Results and Discussion	77
6.4	High-Performance Computing through Silicon Photonics	79
6.4.1	Background	79
6.4.2	Demonstration	80
6.5	Main Takeaways	83

7	Optical Components for Future Applications	84
7.1	Moving into the Long Wavelength Regime	85
7.1.1	Applications of Long-Wavelength Detection	85
7.1.2	Background	86
7.1.3	Photodetector Design and Experimental Setup	87
7.1.4	Experimental Results	88
7.1.5	Improving Long Wavelength Photodetection and Extending Long Wave- length Detection Range	89
7.2	Coherent Reception: Performance Improvement	91
7.2.1	Main Terms	91
7.2.2	Device Theory	92
7.2.3	CPA Modulator Device Description	93
7.2.4	On-Chip CPA Demonstration	94
7.2.5	Discussion on Sampling	95
7.2.6	Device Measurements	96
7.2.7	Benefits of System	97
7.3	Main Takeaways	99
III	Conclusions	100
8	Conclusions	101
8.1	Overview	101
8.2	Future Work	102
8.3	Summary	104
	Bibliography	105
	Appendix: List of Publications	121

List of Figures

1.1	Fiber-optic bandwidth increasing by adopting new technologies depicted in [Richardson, 2013]	5
1.2	Illustration depicting the different dimensions data can propagate	6
1.3	Illustration of full scheme with MDM, WDM, and PDM operation in a system	7
1.4	Integrating control plane in optical system	7
2.1	Different examples of mode multiplexer/demultiplexers; a) asymmetrical directional coupler [Dai, 2013], b) mode interleaver [Chen, 2014e], c) tapered directional coupler [Ding].	12
2.2	Illustration of orthogonal modes coupled between two coupled waveguides. The ψ represents the electric field. The electric field of the even and odd modes evolve into the electric field mode supported by the waveguide. . . .	13
2.3	Simulated device	16
2.4	Makeup of the waveguide, constructed via standard fabrication procedure at Brookhaven National Laboratory (BNL)	18
2.5	a) Device and insulator layers b) after e-beam lithography c) after reactive ion etching d) after plasma enhanced chemical vapor deposition	18
2.6	SEM image of the 2MMWG asymmetric y-junction from top-down	19
2.7	a) Two mirror planar resonator that have "perfect" reflection [Saleh, 1991], where d denotes the optical path length. b) Microring resonator whose injected optical signal is coupled to the waveguide. Its resonance is described by the distance the light travels, respective of radius r , as well as the loss of the medium.	20

2.8	FSR can be seen in the spectral scan characterizing an optical device and full-width half maximum (FWHM) depicting bandwidth that device can support	21
2.9	Image of the MDM microring structure	22
3.1	Coupling setup and integration in the foreground. On the right side of the MMWG, sitting on the center platform, is a $38\text{-}\mu\text{m}$ radius pitch PROFA that couples light into all arms of the MMWG simultaneously. The light is recovered through a lensed tapered fiber (LTF) towards the left side of the figure.	25
3.2	BER measurement and eye diagrams for MDM data through two-MMWG .	27
3.3	2MDM-2WDM and 2MDM-3WDM BER measurement and eye diagrams .	29
3.4	Examples of on-chip polarization-related devices like: a) image of PBS induced through adiabatic transition in an asymmetric junction from [Su, 2014] b) SEM picture of subwavelength-grating polarizer from [Dai, 2016]	30
3.5	Experimental setup supporting polarization multiplexed data across MMWG. Two polarization modes are isolated using a PC and polarizer combination. Then, post chip traversal, the polarizations are similarly selected.	30
3.6	Measured crosstalk levels over wavelength obtained by subtracting the difference in power level between the power seen at the throughput with the power detected at the crossport for a given output port for a) one polarization and b) another polarization	31
3.7	BER measurement and eye diagram of MDM and MDM-PDM across this set link	32
3.8	a) is wavelength scan through one arm of device. b) is result of RSoft simulations of on-chip TE/TM propagation, with corresponding modal power seen at throughput. Boxed region in black depicts simulation resulting in comparison with actual scan in (a).	33
4.1	Top down image of 3-mode device	36
4.2	Crosstalk level of channels 1_s , 2_s , and 3_s going to 1_d , 2_d , and 3_d . Dashed lines indicate regions selected for best crosstalk levels across all three channels.	37

4.3	Experimental setup (left) and device dimensions (right) measured using an SEM	37
4.4	BER Measurement for 3-arm MMWG at 10 Gb/s operation and corresponding eye diagrams	38
4.5	Table of variation of angles for the MMWG device	39
4.6	Visualization of crosstalk for particular angle variations of the 3MMWG . .	39
4.7	Three modes simulated across device of detailed dimensions	40
4.8	a) SEM of the resultant three-armed multimode multiplexer device and b) Prewitt filter for edge detection to computationally measure the angles via length approximations	40
4.9	a) Spectrum when arm is thermally varied b) Spectrum when multimode body is thermally varied	42
4.10	MMWG supporting three modes with dimensions $\theta_1=0.75^\circ$, $\theta_2=0.585^\circ$, $w_1=0.55 \mu\text{m}$, $w_2=0.6 \mu\text{m}$, and $w_3=0.65 \mu\text{m}$, and $L=1.003 \text{ mm}$. w_3 arm is the Left Arm, w_2 arm is the Center Arm, and w_1 arm is the Right Arm. .	42
4.11	Crosstalk level at all arms of the device described here. The legend indicates the crosstalk contribution of the crossport arm on the throughport arm. The arm that is the main contributor to crosstalk has its crosstalk level drawn in bold. The spectral region investigated is boxed. By zooming in on that region, we see the resultant reduction in contribution to crosstalk by the right arm as it is thermo-optically induced.	43
4.12	a) Experimental setup to take the b) frequency response of the 3MMWG device, in reference to the pulse scan itself	45
4.13	Wavelength scan for the 3MMWG device, with the wavelengths of operation circled in each diagram	46
4.14	Experimental setup for 40 Gb/s data across three-MMWG	46
4.15	a) BER and b) eye diagrams of 3MDM-2WDM operation	47
4.16	Top down view of multimode switch layout with inputs and outputs labelled	49

4.17	Crosstalk measurements for the different channels. Spectral profiles at both outputs for each of the four input channels, compared with profiles from interfering channels. Signal and crosstalk were measured individually with a CW tunable laser for configurations with the highest intermodal crosstalk, showing that it is below <16.8 dB in all cases.	50
4.18	Eye diagrams and BER measurements for multimode switch	51
4.19	a) Experimental setup with thermal electric controller (TEC), b) wavelength scan at same temperature (0V bias to the TEC), and c) fit of sum of sine functions with both graphs matching fit parameters < 6 %	52
4.20	Normalized wavelength scan at varying bias, fit to smoothing spine parameter at <0.55 with specific TEC bias of 0.1 V and 0.9 V, with a general red-shifting trend, and the red arrow overlay on the graph indicating the measured shift over 30 degree change	52
5.1	Power Consumption Due to Each Component Geared Towards Passive MDM Setup	56
5.2	a) MDL from [Roelkens, 2010], noting the dark line and b) hybrid ring resonator from [Keyvainia, 2013] showing laser I-V characteristics to determine electrical power consumption	57
5.3	Power consumption of lasers for different multiplexing schemes	58
6.1	2x2 MZI carrier bonded to the socket	64
6.2	Using dither to find precise switch states. a) Near the inflection point at the transmission peak the optical modulation doubles in frequency due to the phase reversal. b) PD output connected to output 1 as MZ is dithered by a 100 mV _{pp} , 1 kHz signal. Detected modulation doubled to 2 kHz at precisely the peak transmission.	65

6.3	Incremental switching shown with basic 2x2 unit where light is injected at Input 1 and power seen at either outputs A and B are varied by biasing the junction. The resulting spectrum sweep is shown in (a) of Output B and (b) of Output A. The percentage labels are with respect to the peak power of Output B.	66
6.4	Switch layout and experimental setup. (a) 2x2 topology, single MZI with 4x4 topology having six MZIs configured into three stages, (b) setup for optical spectrum characterization of variable power allocation to output ports . . .	67
6.5	a) Microscope image of device. Center shows six 2x2 MZI switch stages with left and right arms. b) Benes switch topology: input/output and stage labeling convention for device. MZ6 is upper right MZI switch and MZ1 is lower left in a). c - d) Red and blue curves show normalized power detected at the two output ports of single switch stage as control voltage is adjusted. Switch normally starts in cross state with no voltage applied. PIN tuning in c) shows increased carrier induced losses increase at higher tuning voltages. Multicast operating points are near crossing point of curves.	68
6.6	a) Experimental setup; b) Eye diagrams, and c) corresponding BER measurements of 40 Gb/s error-free dynamic multicasting across the 4x4 optical switch fabric	69
6.7	Cartoon of MZI switch element embedded in 4x4 topology where multicasting (pink, dotted line) is performed	71
6.8	Switch latency	72
6.9	Flowchart implementing algorithm via control plane per the equalization method described in this section	73
6.10	Experimental setup for dynamic demo; b) Channel 2 state initially falls below threshold. It recovers when Channel 1 provides it power in real time. . . .	76
6.11	(a) Simulated setup with integrated switch fabric. (b) Simulation result of percentage of times signal is recovered vs. receiver sensitivity when dynamic power algorithm is employed. Each point in the graph is garnered from over 1000 simulations.	78

6.12	Cartoon of the switch interconnected with the server racks. The optical paths are bidirectional, with the addition of circulators.	80
6.13	Experimental setup of Flexfly topology	81
6.14	Switch latency indicating setup time	81
6.15	Dynamically reconfiguring the system done at second 15 of the exhibited graphs, with one extra global link provided between the two groups	82
7.1	Collection of mid-IR materials technology, where Si is referenced from [Geis, 2009][Grote, 2013]	85
7.2	Absorption Coefficient of Common Materials over Wavelength Range [Palik, 1985]	86
7.3	The center of the structure is intrinsic, and there are p and n doped regions on either side, forming a lateral p-i-n diode. Damage from the ion implantation makes the intrinsic region sensitive to light, which when present in the waveguide causes carrier generation.	87
7.4	PD device embedded in the high-speed system	88
7.5	a) BER measurement for 2 mm (with the corresponding eye diagram) and 3 mm PDs operating at 25 V bias and 1 Gb/s and 0.975 Gb/s respectively; b) Device Responsivity for 2 mm PD at 1.55 μm and 1.9 μm wavelength, with dark current two orders of magnitude lower in current	89
7.6	Modal confinement of different wavelength light through Si ribbed waveguides	90
7.7	a) Device schematic; b) Waveguide cross section with oxide clad coupler region and air clad Si+-implanted region; c) Top-down SEM image	93
7.8	a) Experimental setup for spectral response; b) Experimental setup for phase measurement	95
7.9	a) Power transmission vs. wavelength with $\Delta\phi=0$; b) Power transmission vs. phase shift at the resonant wavelength	96
7.10	DPSK block diagram with a) showing the same amplitude of two signals b) but the difference in phase, which is what DPSK leverages	98

Acknowledgments

I would like to thank the people who have helped me during my Ph.D journey. My greatest appreciation for Professor Keren Bergman for her guidance as my advisor. She provided me with the opportunity and freedom to explore in my research and academics, and, from her, I learned how to be a better researcher and think with an engineering mindset. She gave me valuable advice and direction when I most needed it, and for that I'll always be grateful. I would like to acknowledge Professor Osgood for teaching me about photonics integrated circuits and for guiding me through formative collaborations with his students. I would also like to thank the other members of my dissertation committee: Professor Lipson, for close collaborations and whose students I have collaborated with and learned from, Professor Hendon, my office neighbor and whose students I have spoken with on our floor consistently, and Professor Kilper, for interesting talks about the direction of optics in industry. I appreciate their helpful suggestions for improving my dissertation.

I would like to thank the students from our devices area of LRL who I've constantly consulted and worked with, especially in the beginning of my Ph.D: Noam Ophir, Johnnie Chan, Kishore Padmaraju, and Lee Zhu. In Professor Osgood's group: Jeffrey Driscoll, Brian Souhan, Richard Grote, Alex Meng, and Jacob Rothenberg. Their experience, advice, and encouragement helped me through tough research problems and form great memories in and out of lab.

From my various valuable discussions and collaborations, I've learned a lot from: Tingyi Gu, longtime officemate Ke Wen, who has partaken in many interesting research discussions, David Calhoun, Brian Stern, Atiyah Ahsan, Cathy Chen, Michael Wang, Howard Wang, Qi Li, Gouri Dongaonkar, Ying Li, Lian Wee Luo, Asif Ahmed, Nathan Abrams, Dessie Nikolova, Payman Samadi, Jerry Dadap, the research staff at Brookhaven: Aaron Stein, Ming Lu, and Gwen Wright for their patience and help, and Roe Hemenway, for his help

with starting the switch project. Thanks also to Caroline Lai and Odile Liboiron-Ladouceur for their discussions.

I would also like to acknowledge the newest members of LRL: Yishen Huang, Sasha Gazman, Meisam Bahadori, Yiwen Shen, Hang Guan, Natalie Janosik, Maarten Hattnik, Min Yee Teh, and Richard Dai. I'm excited to see you all make possible new areas in Si Ph research.

Thanks to Peter Bullen, Raj Singh-Moon, Yi Lin, and Nathan Abrams for being the best OSA officers I could ask for.

I am grateful to the friends I've met at Columbia: Jianyi Ren, Yitian Gu, Ying Wang, Jelena Marasevic, Ghazal Fazelnia, Saleh Soltan, Ammar Khan, Lisa Pinals, Jon Widawsky, Yuye Ling, Xinwen Yao, Yu Gao, Rob Margolies, Craig Gutterman, Tingjun Chen, Varun Gupta, Tugce Yazicigil, Esha John, Aseema Mohanty, Steven Miller, Romy Fain, Colm Browning, Wiem Samoud, Lillian Chik, and Oscar Pedrola. Also, thanks to Professor Massimino and Paul Stegall, Josh Cohen, and Mikayla Hoskins for our rewarding ongoing project.

Thanks to Professor Heinz for serving on my proposal committee and providing encouragement to me, Professor Wong, for collaborations in his lab, and Professor Feuer, Professor Wind, Professor Englund, and Ben Lee for their photonics teaching efforts. Thanks also to Professor Ziegler for his encouragement and broadening my writing scope, and Jason Wolfe for allowing me freedom in learning how to teach students effectively.

I would like to acknowledge Elsa Sanchez, Lydia Reyes, Chammali Josephs, Svitlana Samoilina, Jessica Rodriguez, Dario Vasquez, Brandy Maes, and all the EE Department and CISE staff for their help and advice over the years.

My Ph.D was supported by the Semiconductor Research Corporation (SRC) Intel Master's Scholarship, the SRC Intel Ph.D Fellowship, and the Wei Family Private Foundation Scholarship.

For my SRC Intel Fellowship, I would like to thank, in particular, Lee Ann Clewell, MaryLisabeth Rich, and Shannon Geddes for all their help and support, as well as Dr. Ravi Mahajan for being my Intel industry mentor. Finally, I would like to thank my undergraduate research mentor, Shane Cybart, and Sheila Humphreys, who have provided

encouragement throughout my Ph.D career.

Thanks last and foremost to my family and friends for their endless support, my mother Guey-Shiang Tsay and my father Dr. Ming-Yuan Chen, and all my aunts, uncles, cousins, and especially my grandmother for her stories and her strength.

To family and friends

Chapter 1

Introduction

1.1 Next Generation Optical Interconnects

The future of computing could lie in successfully integrating the photonic and electronic platform. Currently, computing—done on laptops, in supercomputers, and with mobile devices—has a wide range of applications and requirements [Patterson and Hennessey, 2007]. However, all of these computing platforms share the need for more bandwidth capacity at lower power and reduced cost.

While transistors might no longer be doubling every two years, in the spirit of Moore’s law [Moore, 1965], scientists and engineers continue to innovate semiconductor integrated circuits to be low cost and high performance. Rather than increasing clock rate, a thermally unsustainable path, multiple processor nodes were integrated on the computing platform with a memory node to support increasing aggregate data. The technology that will drive performance improvements must then operate in a multicore architecture, which shifts the burden of energy consumption onto the interconnects [Rodrigues *et al.*, 2013].

1.1.1 Silicon Photonics

Silicon (Si) photonics leverages CMOS-compatible technology to create high-index contrast Si waveguides on top of the silicon-on-insulator (SOI) platform. In Si waveguides, light propagates at a fraction of the wavelength, allowing for tight confinement of the propagating mode. Si photonic components can offer a host of functionality analogous to electronics, as

optical structures can be exploited for their resonant properties, their fast switch rate, and their small-area, low power modulators and filters.

While electrical wires have RC delays that scale linearly with distance, optical waveguides have no such constraint. However, engineering solutions unique to guiding light in the SOI platform must also be explored before it can reach its full manufacturing potential.

Several breakthroughs enabled Si photonic technology. Si waveguides with loss of 2.4 dB/cm for a 500 nm wire [Dumon *et al.*, 2004] was shown by deep ultraviolet radiation and dry etching in 2004. For a 1 μ m wide Si waveguide, 0.3 dB/cm [Cardenas *et al.*, 2008] has been shown through selective oxidation. Recent demonstrations include about 0.45 dB/cm for wires and 2 dB/cm for slot waveguides [Selvaraja *et al.*, 2014], the loss comparable to the electrical circuit wire model for loss [Rabaey *et al.*, 2003]. Alternate platforms, like Si on top of Si₃N₄ [Bauters *et al.*, 2013], have been explored due to silica losses being 100 to 1000 times lower than Si or III-V materials.

Waveguide crossings are essential for creating multiple subsystems on an integrated platform, but each crossing introduces loss, making it an essential metric to reduce. Crossing losses have been lowered to 0.4 dB [Chen and Poon, 2006] and further pushed to 0.1 dB [Luo *et al.*, 2012] by standard CMOS process.

Reverse tapers on the edge of the waveguide were introduced to improve coupling efficiency between the waveguide mode and fiber, which had been incurring high loss due to the mismatch in modal size and index between the fiber and the waveguide [Lipson, 2005].

1.2 Integrated Photonic Link

For integrated photonics to serve as a paradigm shift in computing systems, it will need to be supplied to consumers in its product form as irreducible units. We could envision reduction in off-chip complexity, eliminating coupling considerations, while device manufacturing could be viably scaled as we move towards creating an integrated photonic link.

Out of the toolbox of photonics, then, we examine the possibility of integrating discrete components, namely the lasing source, the modulator, and the photodetector to create a full communication link.

1.2.1 Lasing Sources

On-chip laser sources are an integral part of the integrated link, but several problems must be solved before they can be achieved. Lasing sources operate by stimulated emission. However, due to silicon's indirect bandgap, whereby the offset in valence and conduction bands at the same momentum vector make it so the photon is not directly emitted by an electron [Soref, 2006], it exhibits imperfect stimulation emission.

As such, monolithic integration of III-V materials has been investigated [Tanabe *et al.*, 2012], but the main challenge to this platform solution is the lattice constant mismatch between III-V materials and Si. Heterogeneous bonding of lasers on Si substrate has also been looked at, but yield needs to increase for adoption of such a method. Within this construct, front-end-of-line (FEOL) or back-end-of-line (BEOL) integration with Si is being considered [Lee and Lipson, 2013].

Among each of these cases, the lasing structure continues to be engineered to decrease modal loss and increase modal gain, while light confinement is enhanced to reduce the lasing threshold [Robinson *et al.*, 2008].

1.2.2 Modulating Data

A link transmitting data can utilize a modulator to impart a 1 or a 0 on a light signal for on-off keying or phase-shift keying. The information contained in the signal is likewise derived from the waveform's amplitude or its phase. Commonly-used optical modulators are made of LiNbO₃, which shifts the waveform by Pockels effect, but Si itself exhibits no Pockels effect.

Instead, modulation in the Si platform has been achieved in other ways. Refractive index of Si can be changed by the electro-optic effect. By coupling the mechanism with a modulator component having high-Q resonance, like microring structures, small bias can be applied to derive comparable modulation, while modulation by mach-zehnder interferometers exhibits better operational stability at higher bias values. The absorption coefficient in Si can also be varied through the Quantum Contained Stark Effect [cvi, 2003]. In either case, the rate of data modulation must be scaled beyond ns-rates to satisfy industry requirements at high-performance. In the case of the electro-optic effect, the limitation for

free carrier plasma dispersion arises mainly from how rapidly free carriers can be injected or removed [Liu *et al.*, 2007]. 50-Gb/s Silicon modulators have been demonstrated [Thomson *et al.*, 2012] with carrier-depletion in a mach-zehnder structure, and mechanisms continue to be introduced to increase modulation rate and improve modulation depth.

1.2.3 Photodetector

Link budget can be improved with a well-designed photodetector. Many of the obstacles encountered in integrating lasers on a Si platform arise with integrating photodetectors. Metrics like quantum efficiency, which is the number of photons converted to electrons, and responsivity, representing the amount of current given energy at a particular wavelength [Bhattacharya, 1997], define the performance of the photodetector. The Si photodetector is explored to improve these metrics for the convenience of monolithic integration, which offers reduced design complexity.

The signal itself can be enhanced by increasing the absorption coefficient of the photodetector. By placing germanium (Ge) on top of Si, its large absorption coefficient at telecom wavelengths can be leveraged. Engineering its placement to couple the optical mode into the substrate allows for the majority of response to be captured [Chen *et al.*, 2008]. Coupled with avalanche multiplication, which may lead to greater responsivities, operational speeds > 30 GHz have been achieved [Assefa *et al.*, 2010].

1.3 Spatial Multiplexing

1.3.1 Increasing Bandwidth: Telecommunications and PICs

The advances made in optical communications for telecom occurred interchangeably with the technological advances of photonic integrated circuits. While the considerations in device design for data propagating across these vastly different lengths might differ, similar motivational technologies can be examined. In order to increase data bandwidth, several domains have been explored.

Fig. 1.2 describes several of these domains. The primary way of increasing data per channel has been through wavelength-division multiplexing (WDM), where multiple wave-

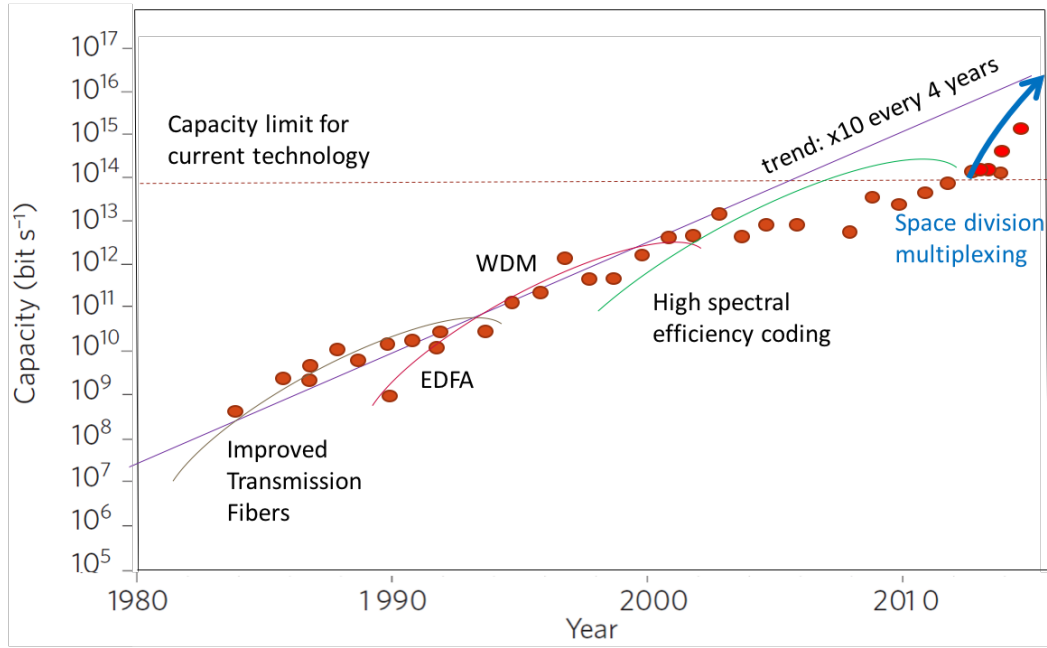


Figure 1.1: Fiber-optic bandwidth increasing by adopting new technologies depicted in [Richardson, 2013]

lengths are combined into a single fiber. Then, from the time domain, data can be time division multiplexed (TDM). In these domains, scientists soon reached a bandwidth bottleneck in continuing to scale data [Richardson *et al.*, 2013]. New methods of spatial multiplexing would have to be explored. In telecom, multicore fibers, multimode fibers, and few mode fibers have targeted increasing density per area.

Likewise, multi-mode supporting waveguides, from multiplexer/demultiplexer units to switches, are being extensively explored for the purpose of higher on-chip bandwidth. This can be combined in conjunction with other forms of spatial multiplexing, like polarization-division multiplexing (PDM). A diagram envisioning their future integration is shown in Fig. 1.3.

Other ways of increasing bandwidth can be through transmitting at higher data rates, transmitting at higher order data modulation [Abrams *et al.*, 2016], and transmitting across a broadband spectrum. However, by using each of these dimensions, certain complexities will arise.

For instance, by fitting a larger data bandwidth across a designated bandwidth, there

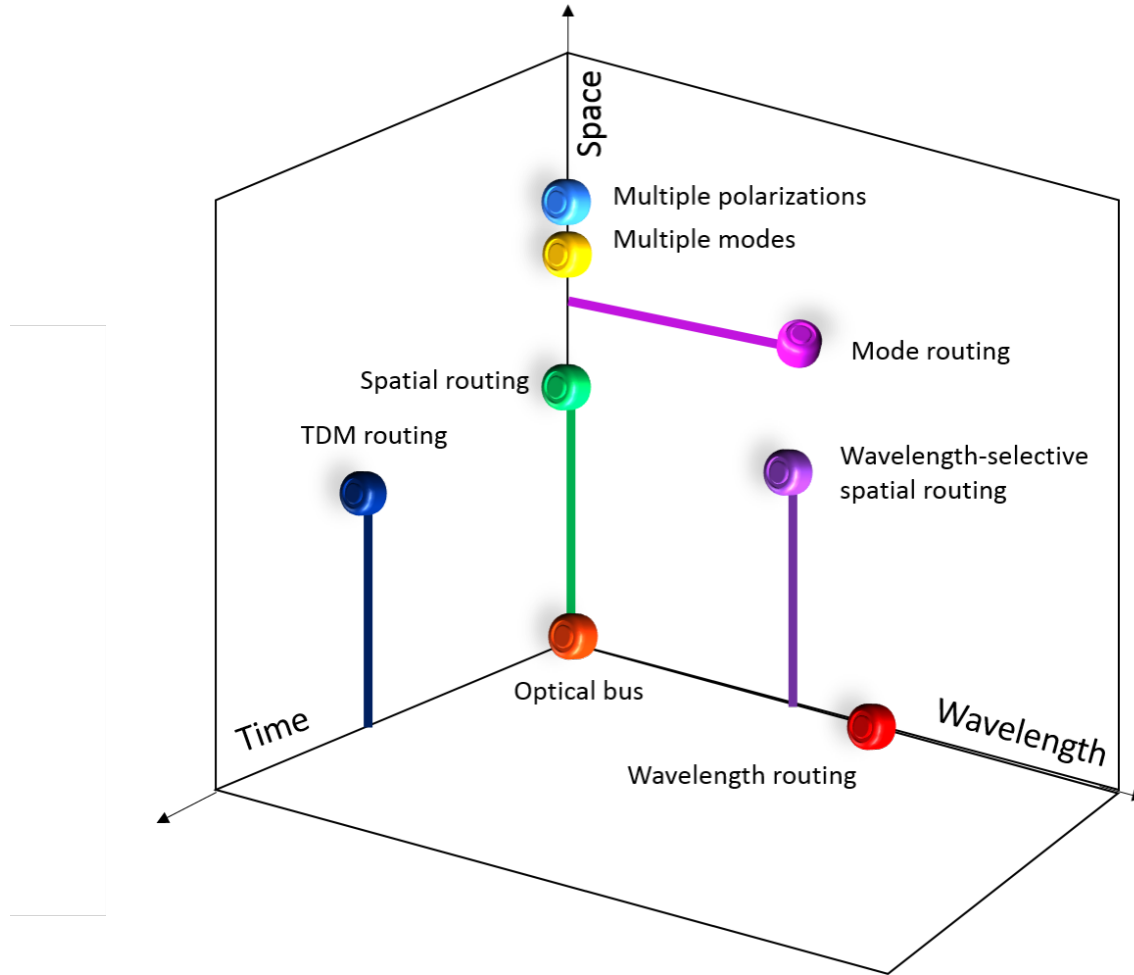


Figure 1.2: Illustration depicting the different dimensions data can propagate

will be greater levels of crosstalk, inducing intrachannel crosstalk. There will also be an increased power per bit metric for photoreceivers operating at higher data rates. Likewise, for higher order data modulation, there is decreased spacing between bits of data. In the case of the wider spectrum support, new link equipment must be engendered and adopted.

1.4 Control Plane

In order to better integrate Si photonics into different systems, it becomes imperative to have the capability to control the physical layer [Calhoun *et al.*, 2016]. The control plane

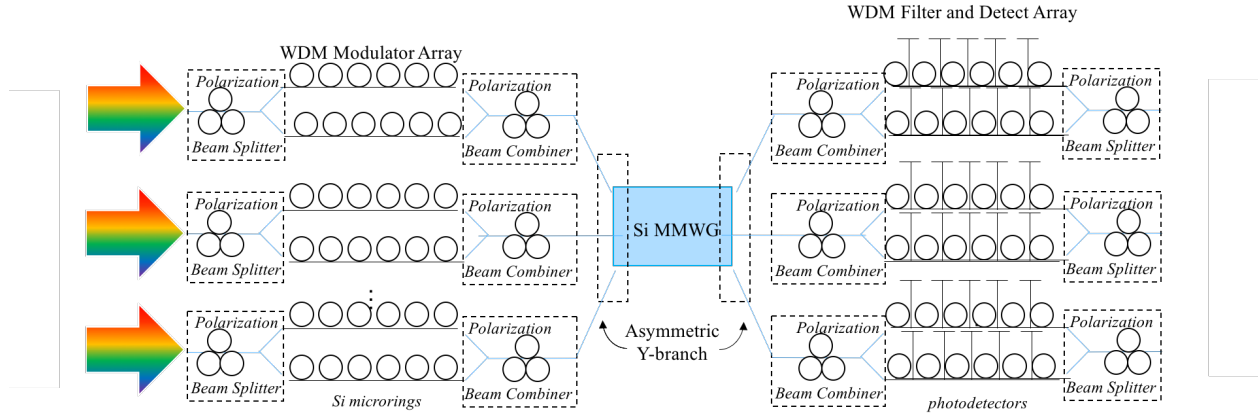


Figure 1.3: Illustration of full scheme with MDM, WDM, and PDM operation in a system effectively needs to operate at speeds faster than optical rates.

Depending on need, the control plane can either be low speed or high speed. An example of the former category is optical performance monitoring, which might have different needs for monitoring network performance, none of them on packet-level granularity level. For the latter, rapid offloading of packets in the optical network might heavily utilize a specialized control plane, further motivating the conversion of systems to optics [Perrin, 2010]. High-performance computing systems have increased bandwidth to hundreds of MHz cycles through multiplexing multiple high clock rate lanes [Eddington and Ray,].

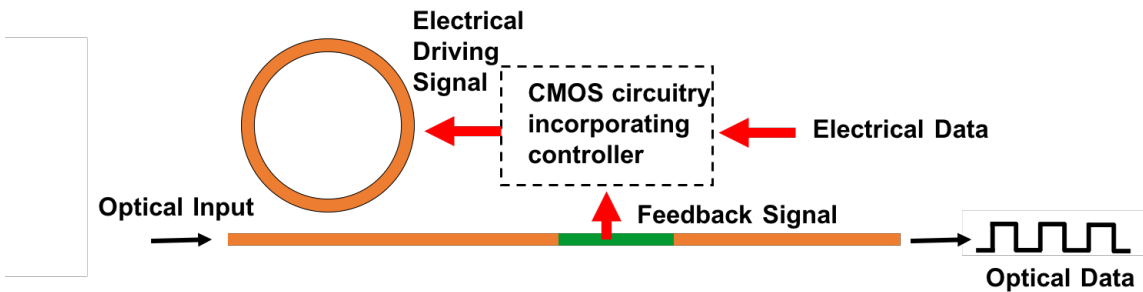


Figure 1.4: Integrating control plane in optical system

With the influx of sensing in the field, it becomes imperative to begin integrating moni-

toring within optics to provide feedback about device performance or overall system performance. In microring resonators, for instance, thermal fluctuations in the environment can induce the operational wavelength to drift, due to the high thermo-optic coefficient of Si, which can prove fatal to the system. As a result, feedback is a necessary tool to maintain wavelength locking [Padmaraju *et al.*, 2013]. On a larger system level, power fluctuations in a datacenter due to varying types of data transmission can necessitate automated power reallocation [Kilper *et al.*, 2011] with the use of a Si photonic switch fabric and dynamic control.

1.5 Focus of Work

The following dissertation proceeds accordingly: Chapter 2 examines the multimode waveguide structure, defines the theory behind its operation, and discusses the fabrication process. Chapter 3 delves into the experimental work behind performing mode-division multiplexing in conjunction with wavelength-division multiplexing and polarization-division multiplexing. In chapter 4, we extend the asymmetric, y-junction from two modes to three mode support. We also demonstrate increasing bandwidth support through the multimode device and improving performance through thermal tuning for optimizing device performance. We describe a device that can switch based on different modes and the features that can support a multimodal system. We consider as well the impact of thermal fluctuations to the signal through the MMWG for integration issues. In Chapter 5, we analyze the benefits of using a multimodal system. We examined the reduction of lasers in a system with multimode support, which improves energy efficiency in the system. In Chapter 6, we demonstrate the control system of a Si Ph switch through dynamic power reallocation. Deeper discussion of system algorithms is described. Using this switch device, we enable a flexible Dragonfly topology inside an HPC, marking the first demonstration of Si Ph in the HPC. In Chapter 7, we discuss the design of integrated parts that make up an entire system. Specifically, we discuss a photodetector that can push detection wavelengths to the infrared regime. In this chapter, we also include the first demonstration of a phase modulator that utilizes coherent perfect absorption. Finally, we will summarize the work presented in this dissertation and

discuss future avenues of work.

Part I

On-Chip Spatial Multiplexing

Chapter 2

Device Design of Multimode Waveguide

On-chip mode-division multiplexing (MDM) and de-multiplexing is desired for its capability of extending an available dimension of orthogonality in the optical waveguide. After presenting background material, the verified phenomenon of MDM through the Si waveguide is described by the mathematical construct of its physical properties. The design of the two-mode supporting multimode waveguide (MMWG) is extended to a three-mode supporting MMWG. The asymmetric, y-junction device, which will constitute the bulk of the spatial multiplexing section of the dissertation, is described and the microring resonator device, which is further utilized in a later chapter, is described as well. Finally, fabrication procedure for the devices are detailed in this chapter.

2.1 Background

Integrated photonics operate in the single mode domain due to the complexity inherent in coupling to higher order modes. Leakage will occur when coupling to higher order modes simultaneously, causing intermodal crosstalk and data degradation. Multimode supporting waveguides are designed to have a height that provides high modal confinement. By varying the width of multiplexing waveguides, a wide range of effective indices can be achieved, allowing for phase-matching of the mode induced in the incoming waveguides to that of the

multimodal waveguide.

2.1.1 Mode Multiplexing and Demultiplexing Designs

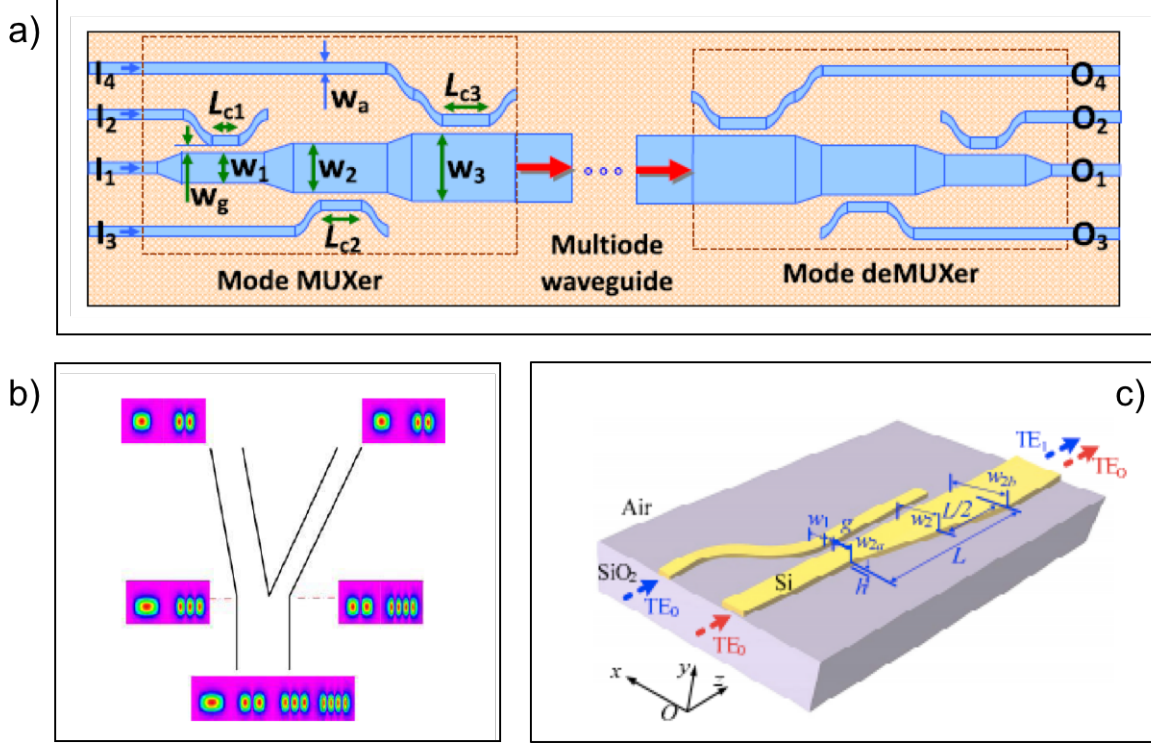


Figure 2.1: Different examples of mode multiplexer/demultiplexers; a) asymmetrical directional coupler [Dai, 2013], b) mode interleaver [Chen, 2014e], c) tapered directional coupler [Ding].

Various architectures of mode-division multiplexing have been proposed. In the realm of supporting multi-mode operation, a multiplexer/ demultiplexer unit is a necessary piece of the transmission link. Experimental demonstrations of MDM have been shown with different devices, including: an asymmetric directional coupler [Ding *et al.*, 2013] [Dai *et al.*, 2013], adiabatic coupler [Wang *et al.*, 2015], asymmetric y-junction [Driscoll *et al.*, 2013] [Chen *et al.*, 2016d], and microring resonator [Luo *et al.*, 2013]. These schemes all follow the principle of phase-matching in the coupling region to the MMWG. Tradeoffs incurred by these different methods include length of device, due to coupling length, device fabrication

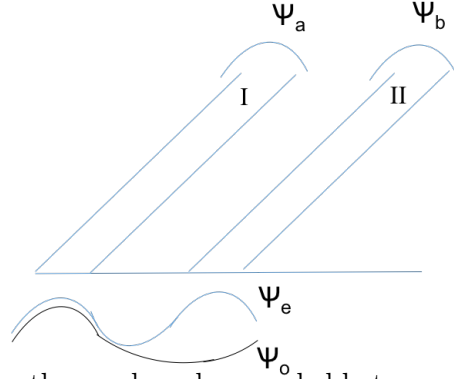


Figure 2.2: Illustration of orthogonal modes coupled between two coupled waveguides. The ψ represents the electric field. The electric field of the even and odd modes evolve into the electric field mode supported by the waveguide.

considerations, and size of bandwidth support, among other parameters.

2.2 Asymmetric Y-junctions for Mode Multiplexer/ Demultiplexer

2.2.1 Theory for Multimode Support

Y-junctions are often employed as power dividers or power combiners. Their functionality can be examined in terms of coupled mode theory (CMT). CMT describes how much of a mode energy shifts between waveguides. For the number of modes, and thus electric fields involved, a beat period appears as a result of the phase mismatch between the electric fields of the modes.

This beat can be determined by finding the propagation constants of the waveguide system from the coupled mode equation. Propagation constants of the symmetric mode ψ_e and antisymmetric mode ψ_o are β_e and β_o respectively.

For the unidirectional propagation, the wave can be written as

$$A(z) = Ae^{-z}e^{-jz} \quad (2.1)$$

and

$$B(z) = Be^{-z}e^{-jz} \quad (2.2)$$

with

$$2\Delta = \beta_b - \beta_a, \gamma = \sqrt{(\kappa^2 + \Delta^2)} \quad (2.3)$$

as the evanescent decay constant.

This will result in β_e and β_o equaling $\beta_m \pm \beta_c$. From here, the corresponding coupling length of $L=\pi/2\beta_c$ can be acquired [Nishihara *et al.*, 1989].

When the two incoming, and likewise outgoing, arms of the y-junction have different widths, they then induce a different phase vector than their neighboring arm. This brings us to the discussion of the asymmetric y-junction.

The coupling from the asymmetric y-junction to the multimode stem occurs adiabatically. The mode couples from the y-junction arm to the closest wavevector inside the multimode waveguide (MMWG). A parameter called the mode conversion factor (MCF) value determines whether the asymmetric y-junction serves as a mode sorter or a mode splitter [Riesen and Love, 2012],

$$MCF = \left| \frac{\beta_a - \beta_b}{\theta\gamma_{ab}} \right|, \quad (2.4)$$

where $\gamma_{ab} = 0.5\sqrt{((\beta_a + \beta_b)^2 - (2kn)^2)}$, and k is the free-space wave vector with n being the refractive index of the cladding. The $MCF < 0.43$ for a mode splitting device and $MCF > 0.43$ for a mode sorting device.

Each mode excited by the mux has a different wave vector; therefore, various relative phase is acquired as the modes propagate along the link. Optimal areas of operation ought to occur at places where the crosstalk is minimal.

There are two fundamental design criteria for the asymmetric y-junction. For mode-sorting, the arm supporting the fundamental mode with the smaller effective index excites

the first odd mode or even mode. The MCF should be minimized for a given value of θ and γ_{ab} . The second parameter is that the mismatch value between the fundamental mode and stem modes compared to the mismatch value between the fundamental mode and higher order mode should be smaller [Riesen and Love, 2012].

Here, we look at the transfer matrix of a two-mode multimode waveguide in terms of Dirac notation [Griffiths, 2004]. We will later extract characteristics of the 3MMWG.

$$D_{mux}|\psi_i\rangle = \begin{pmatrix} k_{11} & k_{12} \\ k_{21} & k_{22} \end{pmatrix} = |\psi_o\rangle = \begin{pmatrix} \psi_{TM,1} \\ \psi_{TM,2} \end{pmatrix}$$

Meanwhile, the propagation matrix is:

$$P = \begin{pmatrix} e^{j\beta_e L_{mm}} & 0 \\ 0 & e^{j\beta_o L_{mm}} \end{pmatrix}$$

By the property of time reversal symmetry, $D_{mux}^{-1} = D_{demux}$. We can multiply across to acquire the matrix for full mode-coupling.

$$\begin{pmatrix} k_{11} & k_{12} \\ k_{21} & k_{22} \end{pmatrix} \begin{pmatrix} e^{j\beta_e L_{mm}} & 0 \\ 0 & e^{j\beta_o L_{mm}} \end{pmatrix} \begin{pmatrix} k_{11} & k_{12} \\ k_{21} & k_{22} \end{pmatrix}^{-1}$$

When $\Delta\Phi = (\beta_i - \beta_j)L_{mm} = m2\pi$, where $m \in Z$, the system simplifies to:

$$\begin{pmatrix} \psi_{a,demux} \\ \psi_{b,demux} \end{pmatrix} = e^{j\beta_e L_{mm}} \begin{pmatrix} 1 & 0 \\ 0 & 1 \end{pmatrix} \begin{pmatrix} \psi_{a,mux} \\ \psi_{b,mux} \end{pmatrix}$$

In the Hilbert space, a sufficient condition for having a real inner product is that the complex functions have the same integer multiple phase. Power superposition is satisfied by the orthogonality of the fields [Bottacchi, 2014].

2.2.2 Theory Extended to Three Modes

The optimal regime for a 3×3 asymmetric Y-junction can be found by using the design methodology that approximates the device geometry minimizing a multiple output factor (MOF). The MOF is used for creating devices that can support > 2 mode operation.

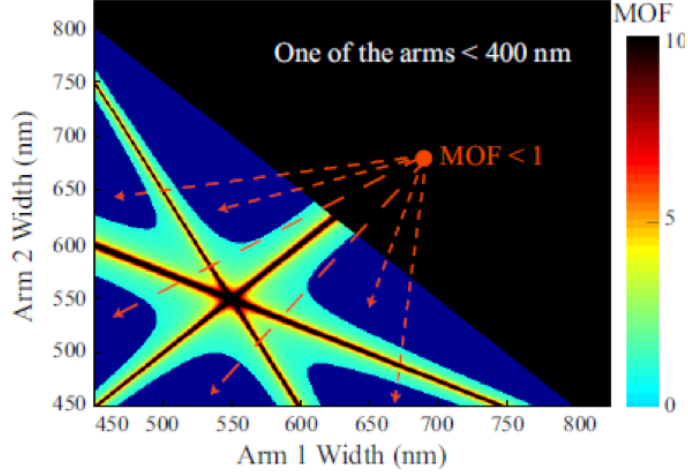


Figure 2.3: Simulated device

$$MOF = \sum_i^N \left| \frac{1}{MCF_{ij}} \right| = \theta \sum_i^N \left| \frac{(i-j)}{(\beta_a - \beta_b)\gamma_{ij}} \right| \quad (2.5)$$

and N is the number of arms, i and j denote individual arms, θ is the divergence angle between adjacent arms (in radians), $\beta_{i,j}$ is the propagation constant of the fundamental mode of an arm, and γ_{ij} is the evanescent decay constant of the fundamental mode between two arms.

The MOF of the 3x3 mux/demux device is illustrated in Fig. 2.3. It is the reciprocal sum of statistically combining the MCFs of all the arms. The region where $MOF < 1$ is where the 3x3 mode multiplexer design is effective.

To verify this design, the crosstalk in each arm is modeled as a function of wavelength using both the effective index method and 2-d eigenmode expansion method and found to be < 10 dB across the C-band, with a minimal value of -25 dB for each arm. With this design, 3-mode MDM could be performed at multiple wavelengths with power penalties < 1 dB.

The transfer matrix of the three-mode multimode waveguide can be extracted in terms of Dirac notation [Griffiths, 2004].

$$D_{mux}|\psi_i\rangle = \begin{pmatrix} k_{11} & k_{12} & k_{13} \\ k_{21} & k_{22} & k_{23} \\ k_{31} & k_{32} & k_{33} \end{pmatrix} = |\psi_o\rangle = \begin{pmatrix} \psi_{TM,1} \\ \psi_{TM,2} \\ \psi_{TM,3} \end{pmatrix}$$

Meanwhile, the propagation matrix is:

$$P = \begin{pmatrix} e^{j\beta_e L_{mm}} & 0 & 0 \\ 0 & e^{j\beta_o L_{mm}} & 0 \\ 0 & 0 & e^{j\beta_{o,2} L_{mm}} \end{pmatrix}$$

By the property of time reversal symmetry, $D_{mux}^{-1} = D_{demux}$. We can multiply across to acquire the matrix for full mode-coupling.

$$\begin{pmatrix} k_{11} & k_{12} & k_{13} \\ k_{21} & k_{22} & k_{23} \\ k_{31} & k_{32} & k_{33} \end{pmatrix} \begin{pmatrix} e^{j\beta_e L_{mm}} & 0 & 0 \\ 0 & e^{j\beta_o L_{mm}} & 0 \\ 0 & 0 & e^{j\beta_{o,2} L_{mm}} \end{pmatrix} \begin{pmatrix} k_{11} & k_{12} & k_{13} \\ k_{21} & k_{22} & k_{23} \\ k_{31} & k_{32} & k_{33} \end{pmatrix}^{-1}$$

When $\Delta\Phi = (\beta_i - \beta_j)L_{mm} = m2\pi$, the system simplifies to:

$$\begin{pmatrix} \psi_{a,demux} \\ \psi_{b,demux} \\ \psi_{c,demux} \end{pmatrix} = e^{j\beta_e L_{mm}} \begin{pmatrix} 1 & 0 & 0 \\ 0 & 1 & 0 \\ 0 & 0 & 1 \end{pmatrix} \begin{pmatrix} \psi_{a,mux} \\ \psi_{b,mux} \\ \psi_{c,mux} \end{pmatrix}$$

2.2.3 Device Fabrication

2.2.3.1 Two Mode Supporting Device

The asymmetric y-junction waveguide structures demonstrated in the multimodal experiments were manufactured at the Center for Functional Material facilities at Brookhaven National Laboratory. The process included e-beam lithography on HSQ-spun resist followed by reactive ion etching (RIE) of the Si layer and cladding laid on by plasma etched chemical vapor deposition (PECVD).

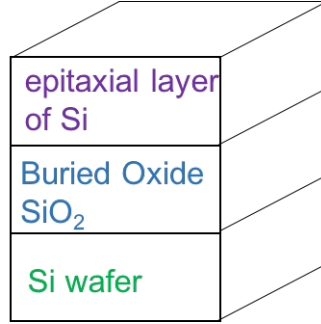


Figure 2.4: Makeup of the waveguide, constructed via standard fabrication procedure at Brookhaven National Laboratory (BNL)

A piece of chip was diced from 250 nm Si on top of 3 μm buried oxide (BOX). This piece was cleaned with acetone, methanyl, and isopropanol. Then, the chip was baked on a hot plate at 450°C for an hour. This step minimizes the amount of hydrophobic surface from developing when the resist is spun on. Next, a HDMS layer is baked on, and hydrogen silesquioxane (HSQ) is spun on the top surface.

The General Station Description (GSD) files were created in RSoft and validated through Beamprop simulations. This pattern is placed in the BEAMER software, which converts the layout to a file that the e-beam lithography system can interface. These patterns were exposed to 2 nA beam current, which results in a beam spot size of 5 nm. The HSQ crosslinks when it is exposed to the electron beam dosage.

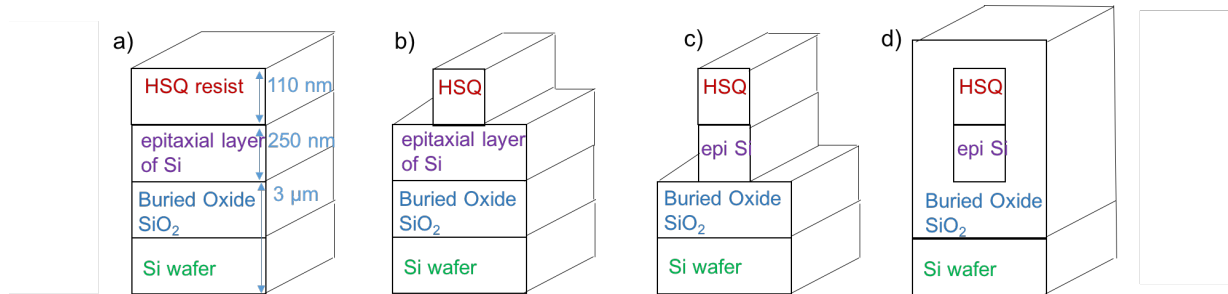


Figure 2.5: a) Device and insulator layers b) after e-beam lithography c) after reactive ion etching d) after plasma enhanced chemical vapor deposition

The next step is the development process. The chip is placed in a basic mixture of NaCl

(4%), NaOH (1%), and H₂O. Sonication was alternately done to the samples to prevent particles from staying on the chip surface, and followed by the same procedure with Di water.

RIE using various recipes, including HBr/Cl Si etch, is performed next. We carefully develop sharp side walls by not overetching. Finally, SiO₂ is deposited ontop of the waveguide to serve as cladding.

The heights of the incoming and outgoing arms as well as the MMWG are 250 nm tall. For a 2MMWG, the arms have widths of 450 nm and 550 nm. The MM waveguide has a width of 1 μ m. An angle of 1.3° then results in a MCF of 1.3. L_{mm} is designed to be 1.2 mm [Driscoll *et al.*, 2014].

As noted before, the operational wavelengths occur in areas where coherent crosstalk is at a minimum. When

$$\Delta\phi = 2_{mm} |n_{eff,e} - n_{eff,o}| = m2\pi \quad (2.6)$$

where m is an integer multiple, the free spectral range (FSR) becomes

$$\Delta\lambda_{fsr} = \left| \frac{\lambda^2}{L_{mm}(n_{g,e} - n_{g,o})} \right| \quad (2.7)$$

The relation between the effective index and group index is given by

$$n_g(\lambda) = n_{eff}(\lambda_o) - \lambda_o \left(\frac{dn_{eff}}{d\lambda} \right) - \lambda_o \Delta\lambda \left(\frac{d^2 n_{eff}}{d\lambda^2} \right). \quad (2.8)$$

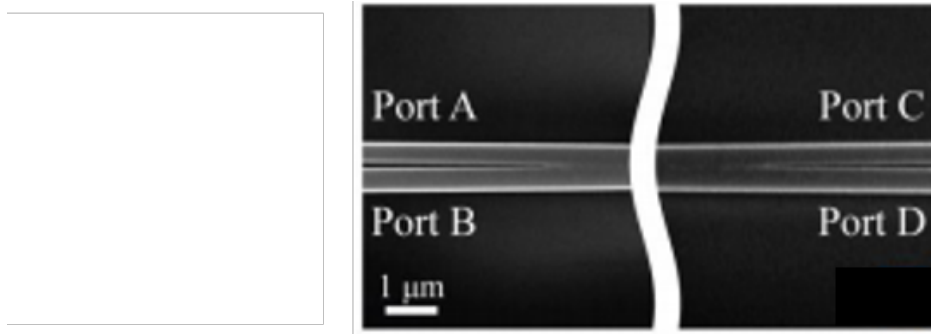


Figure 2.6: SEM image of the 2MMWG asymmetric y-junction from top-down

2.2.4 Three Mode Supporting Device

The asymmetric, y-junction device supporting three modes is created at Brookhaven National Lab, as described in the prior section. Besides the MOF, the procedure discussed in Chapter 4 can be followed to further optimize the device. There, in addition to phase-matching being performed on the device, the angles can be varied to extract more overlapping wavelength regimes.

2.3 Microring Resonator for Mode Multiplexer/Demultiplexer

2.3.1 Background: Optical Resonators

Resonators are components that confine and store energy at certain frequencies. In optics, when light is resonant in a medium, it is able to propagate back and forth within that medium while retaining the amount of energy for a duration of time. The effectiveness, meaning the amount of time this oscillation will stably occur, is termed as the Q value of the resonator.

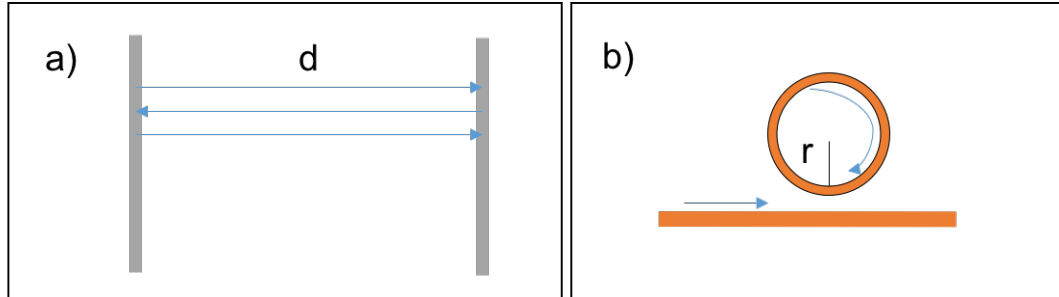


Figure 2.7: a) Two mirror planar resonator that have "perfect" reflection [Saleh, 1991], where d denotes the optical path length. b) Microring resonator whose injected optical signal is coupled to the waveguide. Its resonance is described by the distance the light travels, respective of radius r , as well as the loss of the medium.

In both of these cases, we can describe the resonance by its free spectral range (FSR). This denotes the periodic frequencies where light is propagating in the cavity structure.

$$FSR = \Delta f = \frac{c}{2nd\cos(\alpha)} \quad (2.9)$$

where α represents loss.

The resonant mechanism is regularly used in optical spectrum analyzers and tunable lasers, where mechanically tuning the distance between reflecting mirrors determines the light transmitted by the resonant cavity.

The FSR can be seen when spectral scans are taken, as depicted in Fig. 2.8.

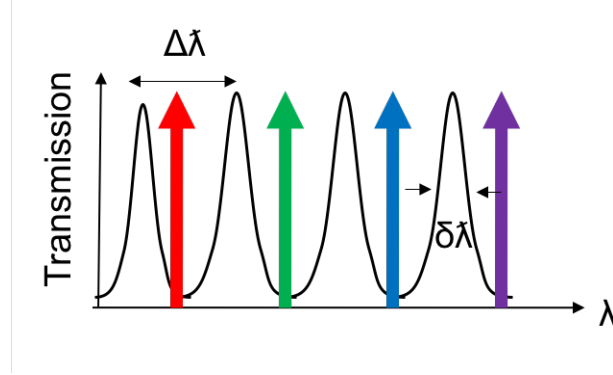


Figure 2.8: FSR can be seen in the spectral scan characterizing an optical device and full-width half maximum (FWHM) depicting bandwidth that device can support

The arrows in the figure indicate wavelengths that can pass by this device through WDM operation.

2.3.2 Theory for Multimode Support

Mode-multiplexing via microring resonators enables active coupling of light into the multimode regime. It also allows for additional wavelength tuning capability. Multiplexing of the modes can be done in two ways; either the microring waveguide width is varied, thereby varying the supported mode, and the waveguide width is held constant, or the microring waveguide width is kept constant, and the bus waveguide width is tapered across multiple coupling regimes. For both these possibilities, by varying the effective index (n_{eff}), a different order mode is induced. In [Luo *et al.*, 2013], the three microrings were identically single mode while the waveguide width varied in different sections of the coupling regime. Depending on intended tradeoffs, with the microrings' waveguide width varied and the waveguide held constant across all coupling regimes, modes are able to be added or dropped without disturbing neighboring modes. However, multimode waveguide bends require an additional

level of optimization [Gabrielli *et al.*, 2012] and fabrication detail.

The phase-matching principle is calculated according to the procedure described in the previous section and can be likewise considered through coupled mode theory.

2.3.3 Design of the MM Regime

Si/SiO₂ as the core-cladding yields a high index contrast. The coupling waveguide is 250 nm tall for high confinement. That way, greatly varying propagation constants are possible, with TE₀ to TE₄ having n_{eff} of 2 to 2.9. By matching the propagation constant, a mode can be evanescently coupled from a single mode WG to a MMWG where coupling strength depends on the width of the MMWG and the optimized coupling gap.

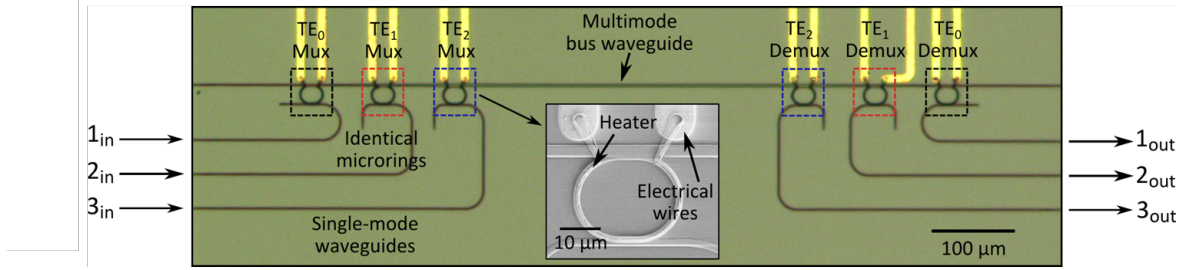


Figure 2.9: Image of the MDM microring structure

The regions where the mode couples from a microring with n_{eff} of 2.46 is tapered ranging from 450 nm to 1.41 μm . The coupling gap and the coupler length between the microrings and waveguides are optimized to minimize insertion loss for the mode and minimize intrachannel crosstalk, with a coupling length of 6- μm leading to lowest loss values.

2.3.4 MDM System

While the orthogonal domains on-chip can be leveraged, it must also be considered how to harness the bandwidth of these signals once off-chip. An analogous realm of research into spatially-multiplexing data in fibers has been developed over the past few years. Multicore fibers group multiple cores into a single fiber, thereby increasing bandwidth in a single fiber while keeping uncoupled modes [Richardson *et al.*, 2013]. Few mode fibers similarly increase bandwidth but the inherent non-linearities of coupled modal properties to recover

the signal [Ramachandran, 2005] must be taken into consideration. While multimode support in fibers can push fiber-optic bandwidth to great heights, it has to be complemented by developing multimode technologies inline to the fiber system. This includes, but is not limited to: amplifiers [Jia *et al.*, 2012], ROADMs [Nelson *et al.*, 2014] [Wang *et al.*, 2016], and photodetectors [Viana *et al.*, 2013], moving towards an end-to-end multimodal system.

2.4 Main Takeaways

In this chapter, background of mode-division multiplexing (MDM) devices and the theory behind their operation is described. Specifically, the asymmetric, y-junction structure is examined mathematically for its phase-matching functionality, in particular, in terms of coupled mode theory. Then, design of the MMWG is expressed in terms of optimizing the mode-sorting criterion. We further supplement this section with description of the device fabrication process. While this section focuses on devices supporting two mode multiplexing, three mode support is also introduced. Use of microring devices for MDM operation is described. Finally, implementing system-wide MDM is examined.

Chapter 3

Spatial Multiplexing for Ultra-high Bandwidth

By combining mode-division multiplexing with other forms of spatial multiplexing, a myriad of paths can be engendered for continuing to scale on-chip data bandwidth. Experimental setup and results across the 2-MMWG waveguide are described, specifically mode-division multiplexing in conjunction with wavelength-division multiplexing (WDM) and polarization-division multiplexing (PDM). The particular experiments described in this chapter are as follows: 2MDM, 2MDM-3WDM, and 2MDM-PDM. Challenges faced with each experimental design and measurement technique are elaborated.

3.1 Enabling Mode-division Multiplexing (MDM)

The overarching theme of this section is to illustrate the technical implementation of scaling data bandwidth on-chip by using domains not explored before. Details are presented of how mode-multiplexed data propagating on-chip was enabled by available optical components assembled in our laboratory [Chen *et al.*, 2013a] [Chen *et al.*, 2013b].

3.1.1 Experimental Setup

The continuous wavelength (CW) laser operating in the C-band is modulated with data using a LiNbO₃ modulator. The pulse pattern generator (PPG) puts out non-return-to-zero

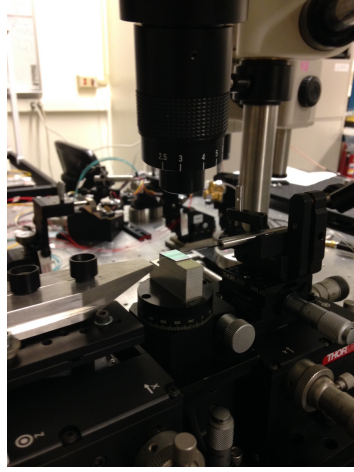


Figure 3.1: Coupling setup and integration in the foreground. On the right side of the MMWG, sitting on the center platform, is a $38\text{-}\mu\text{m}$ radius pitch PROFA that couples light into all arms of the MMWG simultaneously. The light is recovered through a lensed tapered fiber (LTF) towards the left side of the figure.

(NRZ) 2^7-1 pseudo-random bit stream (PRBS) data. The PPG and the recovery module are clocked with the same source. Then, the signal is passed through an erbium-doped fiber amplifier (EDFA) before being propagated through an inline power splitter that splits the signal into m channels, where m denotes the number of modes that the device can support. A spool of standard single mode fiber (SSMF) decorrelates 625-meters between 2 channels. To ensure that the bit sequence of the different channels are decorrelated, a relative delay is injected into the PRBS pattern. If our data rate is 10 Gb/s, then our delay is $0.625\text{ km} \times 17\text{ ps}/(\text{nm km}) \times 4\text{ nm} \times 10\text{ Gbps} = 0.425\text{ bits}$. The polarization controller (PC) is placed inline each of the pathways directed to the device in order to control the polarization of each arm separately.

A pitch reducing optical fiber array (PROFA) with $38\text{-}\mu\text{m}$ pitch is used to launch several channels simultaneously on-chip [Kopp *et al.*, 2015]. The signal exiting the waveguide is recovered with a tapered fiber. The signal is summarily amplified and filtered before the signal is detected using a PIN-TIA avalanche photodetector followed by a limiting amplifier (LA) to amplify the signal going into the bit error rate (BER) tester for BER measurements and/or the digital communication analyzer (DCA) to recover eye diagrams.

3.1.2 System Considerations

3.1.2.1 Coherence Length

In the optical system where light beams from the same source are split and then again recombined, the coherence length of the source must be taken into consideration. Otherwise, the two participating beams will become mutually incoherent [Hui and O’Sullivan, 2009]. The coherence length is represented mathematically by $L=c/n\Delta f_{lw}$, where Δf_{lw} is the line width of the laser source and n is the refractive index of the transmission medium. In this case, the SMF has a refractive index of 1.5 and $\Delta f_{lw}=200$ kHz. Coherence length L then equals 1 km. The idea of maintaining coherence in a fiber is analogous to minimizing errant power present in a signal when waves of different frequencies and fixed phase are combined, the result of which is white noise.

3.1.2.2 Power Penalty

Device performance takes a hit when there is intrachannel crosstalk. In the case of the MMWG, when there is improper optical confinement, coherent crosstalk occurs [Winzer *et al.*, 2005]. The power penalty (PP) that will theoretically be seen is related to

$$PP = -10\log(1 - 2\sqrt{\epsilon}), \quad (3.1)$$

where ϵ is P_x/P_t . P_x is the power exiting the cross port, and P_t is the power exiting the through port [Rawaswami *et al.*, 2004]. In order to recover the data and maintain the link, a higher power level must be injected into the system.

3.1.3 Data Results

Of any experimental result, the eye diagram indicates to the viewer the signal resilience. The transmitted data is swept over the same time slot. Any timing jitter can be visualized by the shrinking of the horizontal transition regions of the eye over an increasing number of sweeps.

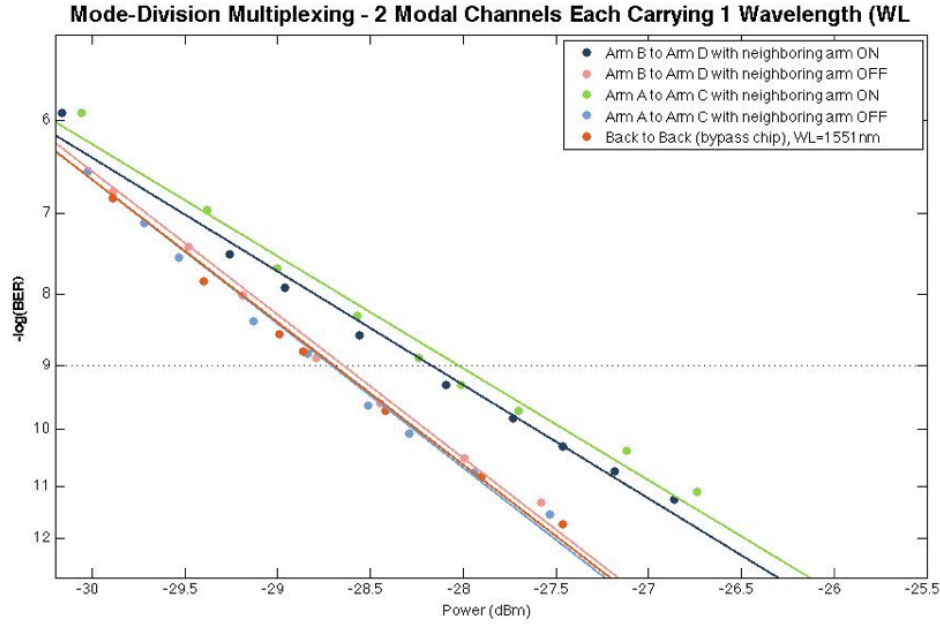


Figure 3.2: BER measurement and eye diagrams for MDM data through two-MMWG

Noise that is introduced by the system can be seen in the railings of the eye diagrams. A thicker top rail means that the 1's that are being set are accumulating distortion. The desired signal is an eye yielding equal intensity between the 0 and 1, which are the bottom and top railings respectively.

Most of the data are taken according to the IEEE-802 standards [Anslow, 2013]. The equipment is standardized so that any data retrieved is comparable to industry measurements.

The BER measurements and eye diagrams for MDM operation through the asymmetric

y-junction are shown in Fig. 3.2. The power penalty can be read from the BER diagram, as 0.6 dB at $\text{BER} = 10^{-9}$.

3.2 MDM-WDM

In order to specify the WDM capacity, to utilize MDM with existing WDM technology, wavelengths of data are incrementally added on top of each modal channel.

3.2.1 Experimental Setup

The CW laser operating in the C-band is modulated with data using a LiNbO_3 modulator. The PPG puts out NRZ $2^{31}-1$ PRBS data. The PPG and the recovery module are clocked with the same source. Then, the signal is passed through an EDFA before being passed through a 1.5 km spool of SSMF. The SSMF has dispersion of 17 ps/(nm km) at 1550 nm [Peerlings, 2003] so this spool serves to decorrelate the wavelength channels by 25.5 ps/nm.

The latter half of the setup from the launch on-chip to recovery of the signal with the photodetector mirrors the layout described in Sec. 3.1.1.

3.2.2 Data Results

When transmitting several wavelengths along the 2 modal channels (MDM-WDM), the amount of crosstalk leaking from 1 modal channel to the next at each wavelength was minimized by choosing to operate in the spectral regions with minimal crosstalk levels. Then, by balancing the power entering each arm at a particular wavelength such that the relative crosstalk of each channel was equal, equivalent performance could be realized.

By looking at Fig. 3.3, the level of crosstalk from adding each additional wavelength channel can be visualized. The experimental results of dual-wavelength MDM-WDM and triple wavelength MDM-WDM are displayed. From these curves, the power penalties for 1551 nm at $\text{BER}=10^{-9}$, when averaged between top and bottom arms, turn out to be 0.66 dB for 2 wavelengths and 0.7 dB for 3 wavelengths.

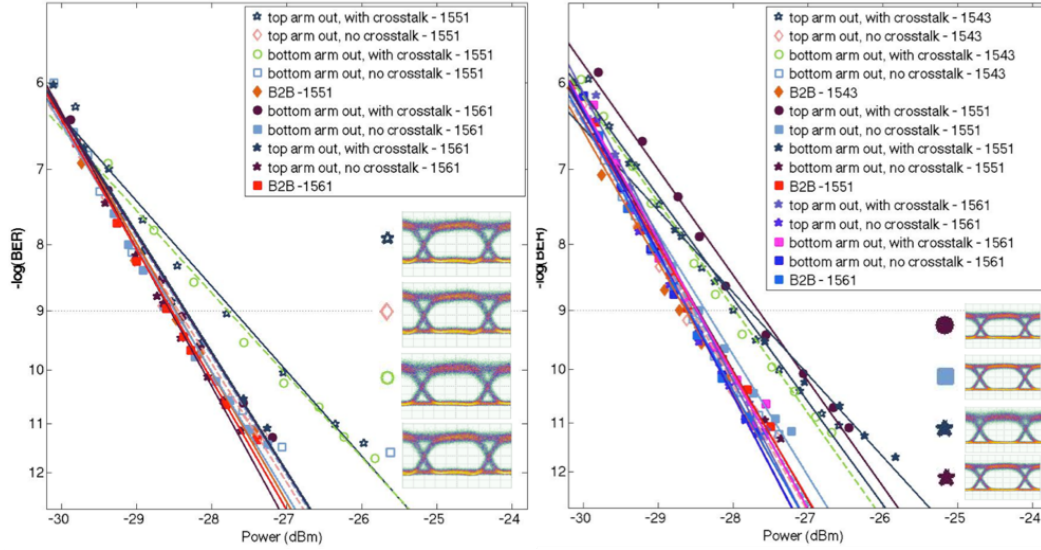


Figure 3.3: 2MDM-2WDM and 2MDM-3WDM BER measurement and eye diagrams

3.2.3 Discussion

There is negligible power penalty introduced from each additional wavelength placed on top of each MDM mode. This indicates that the technique is scalable to more wavelengths, and it is possible to substantially increase on-chip bandwidth density.

As mentioned earlier, the launch power of each arm is equalized. This is performed in an effort to have the relative crosstalk of each channel be equal, so equivalent performance could be attained. Since the crosstalk for a particular arm is dependent on the relative input power level at each arm, if the levels are relatively uniform, then we want to make sure to equalize the power level seen entering each input port of the MMWG device. It has also been shown through the microring-resonator based mode multiplexer/demultiplexer described in the prior chapter that scaling wavelengths on top of modes does not noticeably scale power penalty.

3.3 MDM-PDM

While MDM components can leverage either quasi-transverse-electric (QTE) or quasi-transverse-magnetic (QTM) spatial modes, simultaneous utilization of both modes is challenging. Indeed, most MDM methods are polarization sensitive, with deviations from ideal

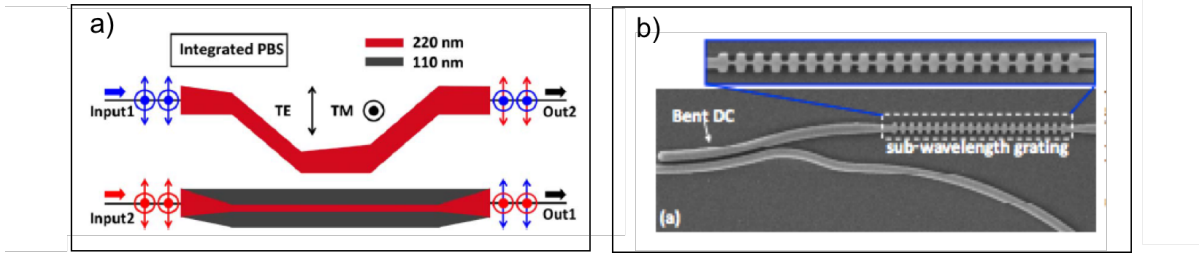


Figure 3.4: Examples of on-chip polarization-related devices like: a) image of PBS induced through adiabatic transition in an asymmetric junction from [Su, 2014] b) SEM picture of subwavelength-grating polarizer from [Dai, 2016]

polarization resulting in a significant amount of crosstalk [Nelson *et al.*, 2001]. However, integrating this pol-muxing capability with a multimode waveguide is possible and recent SiPh polarization-diversity circuits have served integrally as part of the interconnect fabric [Doerr *et al.*, 2010] [Fukuda *et al.*, 2008], enabling on-chip MDM-PDM [Mengyuan *et al.*, 2014]. These circuits have included SiPh polarization-diversity arrangements of splitters, rotators [Watts *et al.*, 2005] and polarization insensitive wavelength filters [Sheng *et al.*, 2016].

3.3.1 Experimental Setup

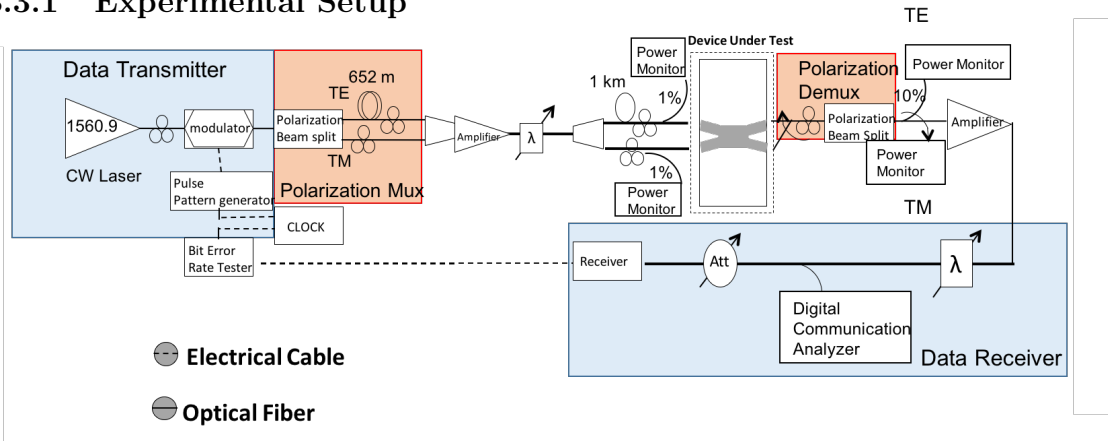


Figure 3.5: Experimental setup supporting polarization multiplexed data across MMWG. Two polarization modes are isolated using a PC and polarizer combination. Then, post chip traversal, the polarizations are similarly selected.

Wavelength scans for MDM-PDM operation are conducted by measuring power through

the chip of either polarizations selected using a PC/polarizer combination. Low crosstalk over orthogonal regimes must be shown for viable operation of the device at both polarizations and all modal channels to occur.

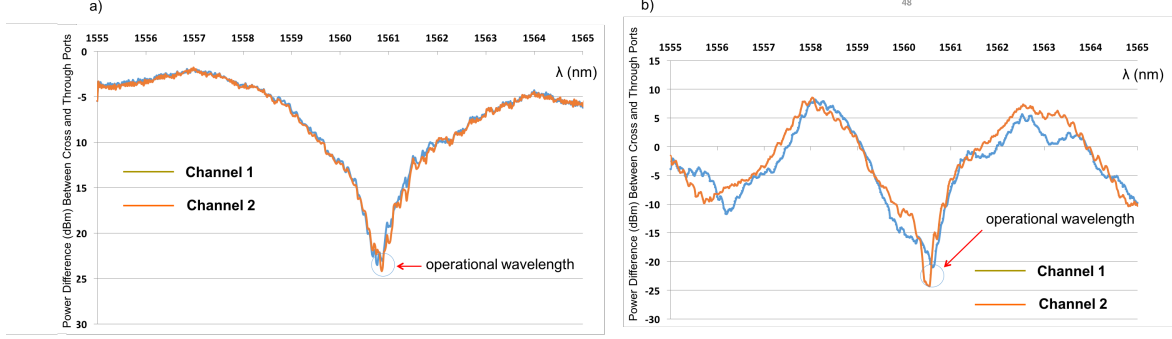


Figure 3.6: Measured crosstalk levels over wavelength obtained by subtracting the difference in power level between the power seen at the throughput with the power detected at the crossport for a given output port for a) one polarization and b) another polarization

The CW-light is generated at 1556.9 nm using a tunable laser, and the signal is modulated with the OOK-NRZ $2^{31}-1$ signal [Chen *et al.*, 2014a] [Chen *et al.*, 2014b]. It is split and orthogonally recombined to generate PDM data. For further verification, different data rates were launched on different polarizations.

The 625-meter SSMF is put on the TE path to decorrelate the signal from the TM path. The EDFA is placed in-line to boost power before launching the signal on-chip. A 1-kilometer fiber is placed in one of the modal paths to decorrelate the two tributaries.

Post-chip traversal, the light signal is inspected from one output port at a time using a LTF. The pol-muxed data is then separated into its TE and TM components using a PC followed by a polarizer.

The orthogonal degree of freedom gained through polarization allows for full maximization of spatial freedom. By launching pol-muxed channels across the two-mode MMWG, simultaneous MDM and PDM operation is demonstrated. 40 Gb/s aggregate bandwidth is attained by using 2 modes \times 2 polarization modes \times 10 Gb/s across the MDM-PDM link with power penalties of < 5 dB/channel.

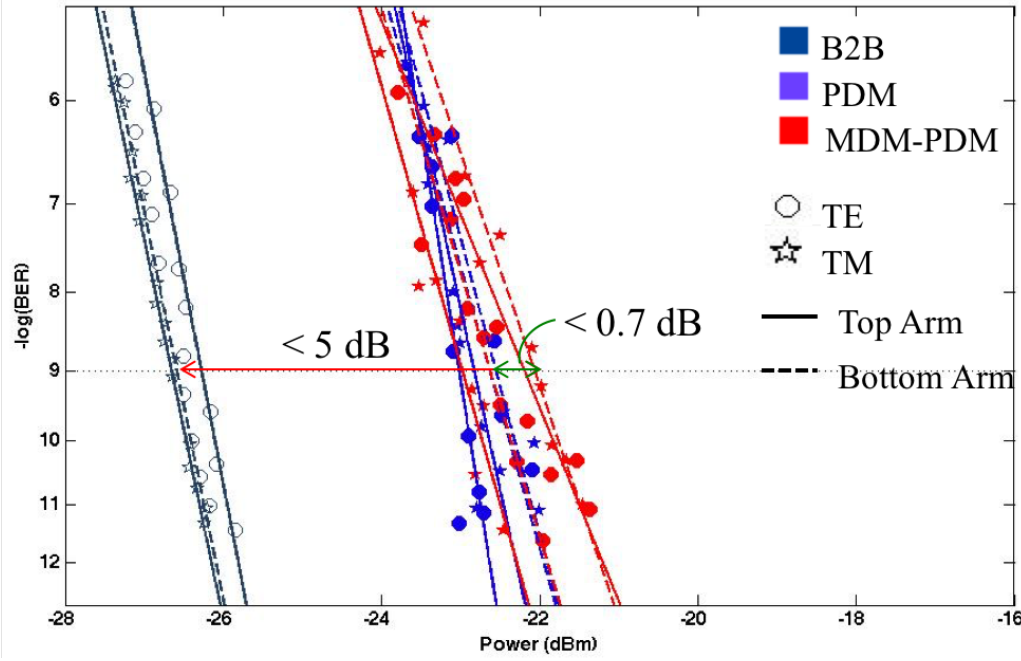


Figure 3.7: BER measurement and eye diagram of MDM and MDM-PDM across this set link

3.3.2 Data Results

To demonstrate a complete MDM-PDM link, several BER plots were recorded. The first set of BER curves consist of back-to-back (B2B) curves obtained using two polarization paths leading up to the chip.

The measurements of MDM on-chip only showed a 0.5 dB PP when 2 MDM channels carrying 10 Gb/s data per mode were transmitted.

In the following measurement, polarization channels were both activated and launched on-chip. The 2 x 2 x 10 Gb/s MDM-PDM shows support by both the QTE and QTM modes.

BER measurement for each possible combination was extracted. PP varied based on the selected wavelength. Maximum resulting penalty from MDM-PDM operation was 5 dB. A maximum of 4 dB was observed for the PDM link, 1 dB less than MDM-PDM operation, which matches well with previously measured MDM PP. The majority of PP was contributed from polarization crosstalk. This can be optimized by engineering the polarization-insensitive device on-chip.

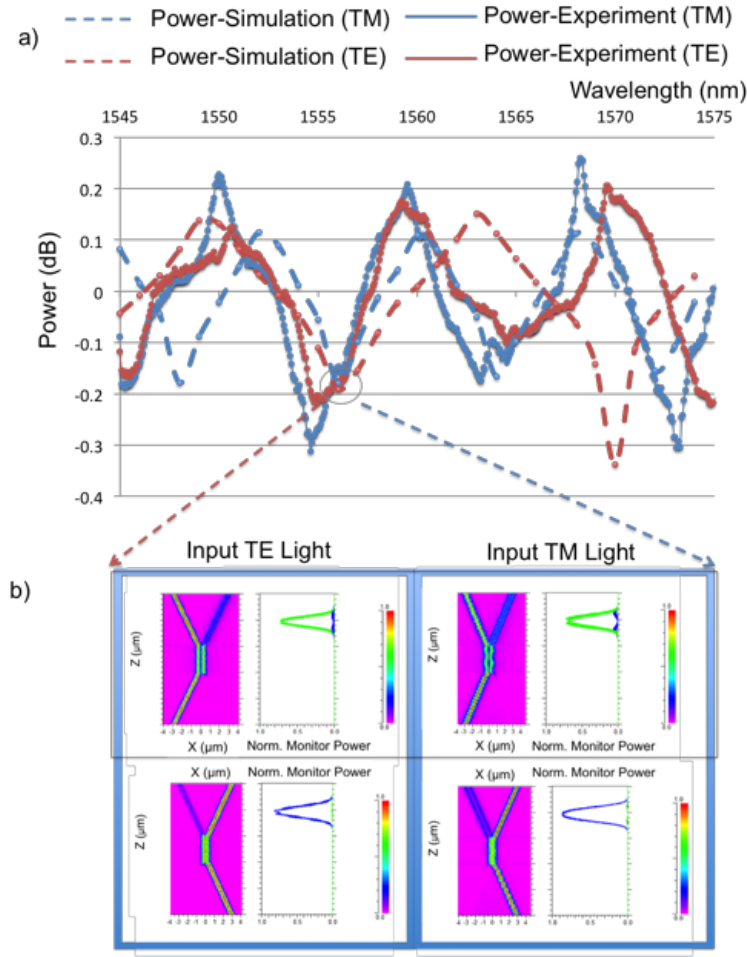


Figure 3.8: a) is wavelength scan through one arm of device. b) is result of RSoft simulations of on-chip TE/TM propagation, with corresponding modal power seen at throughport. Boxed region in black depicts simulation resulting in comparison with actual scan in (a).

3.3.3 Simulations

We model the MDM-PDM asymmetric Y-junction mux/demux using the eigen-mode expansion (EME) method via ModePROP simulations. Simulated results from utilizing this method serve as a guidepost for the experimental data, by illustrating the same general trend for both cases.

The experimental PER is verified using ModePROP through RSoft simulation calculations. Any deviation between the exact overlap of experimental and simulated wavelength scans is likely due to the device parameters varying from their designed values incurred as a

result of the fabrication process. One way of studying the variance of PP contribution due to polarization imperfection is through the polarization extinction ratio (PER), the linear sum of extinctions of TE and TM light after transmission through the device [Fukuda *et al.*, 2008]. As the ratio of the sum of individual minimum to maximum polarized power for both TE- and TM-polarized light, any variance is the result of cross-beating effect [Nishihara *et al.*, 1989].

3.4 Main Takeaways

In this section, experimental demonstration of high-speed data transmission through a MMWG is depicted. In particular, challenges of MM operation through the system are explained. For each of the multiplexing schemes, a detailed look into the experimental data results is provided. Various forms of spatial multiplexing on top of the multi-modes are performed across the asymmetric, y-junction device, through simultaneous MDM-WDM, followed by MDM-PDM operation. Simultaneous WDM data support is illustrated by incrementally adding wavelengths and measuring < 0.7 dB power penalty at error-free operation. Simultaneous PDM operation is possible by selecting specific wavelengths where crosstalk contribution from neighboring arms is minimal and, furthermore, operable. ModePROP simulations are performed to further explore the polarization theory behind this work. To the best knowledge of the author, this is the first demonstration of MDM-PDM performed on-chip.

The combination of these available realms of on-chip spatial multiplexing is one direction forward for continuing to scale bandwidth. By improving design parameters of multi-mode supporting device structures, systems can be created on-chip utilizing these orthogonal domains. Furthermore, schemes where isolation between channels are needed can look towards these physically orthogonal pathways as a viable solution of traversing data simultaneously and *securely* on-chip.

Chapter 4

Scaling MDM Capacity

In this chapter, we progress to perform data transmission across the three-MMWG device. The data is scaled in two ways: by increasing the number of modal arms from two arms to three, as well as scaling bandwidth on top of each induced propagating mode. The technical challenges, both in terms of device physics and experimental, are discussed in detail. From what we learn, we then examine how device performance can be improved through design considerations and dynamic phase variation. Further, we delineate the properties of a spatial switch that can serve as a fundamental element in future generations of network-on-chips. Other considerations for industrial adaptation of device technologies supporting MM operation are analyzed.

4.1 Scaling MDM channels

The question becomes: how can we viably scale the number of modes supportable by the device geometry? In terms of the multimode regime, the width of the waveguide determines the number of modes that can be supported. For the mode multiplexer/demultiplexer, the number of modes the asymmetric y-junction can support theoretically depends on device area limitations.

4.1.1 Three Modes

As we scale the number of modes from two modes to three, we learn several points. As the number of asymmetric y-junctions increases, the areas in which low crosstalk exist undergoes a reduction [Chen *et al.*, 2014c].

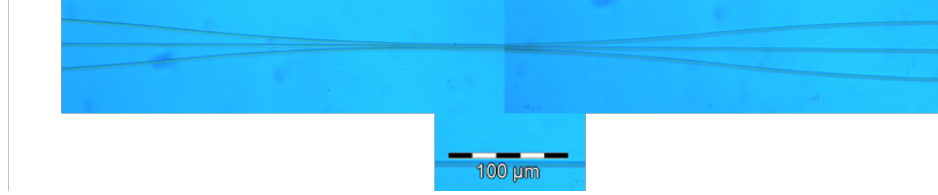


Figure 4.1: Top down image of 3-mode device

The design of the 3-mode device, and any device supporting 3 or more modes, is done through minimizing the multiple output factor (MOF), which was explained in Sec. 2.2.2. As the number of y-junction branches increases, [Riesen and Love, 2012] states that the length of the y-junction scales non-linearly. We have not necessarily found this to be the case. As the number of modes supported increases, the angles etched does need to be smaller. The design process will necessarily become more intricate. Most significantly, fabrication needs to be designed with relative alignment of operating wavelengths to simultaneously scale supported wavelengths. It can alternately be considered to add additional device adjustment for post-fabrication optimization of the operational wavelength regime.

Even with phase-matching determined as per Section 2.2.1, power equalization along each modal path might need to be performed to compensate for losses along each path in the system. Power matching is done according to proportional fairness allocation [Mo and Walrand, 2000]. $\sum p_i f(x_i)$ is maximized, where p_i represents a positive number and $f(x_i)$ represents a strictly concave function (ie., it can be optimized), with a basis of eigenvectors. In this case, we have a special case, which is one link and N connections, so the power is split equally irrespective of the function.

For the 3-mode device, data operation is performed across the device with the characterized crosstalk level of the device shown in Fig. 4.2. Following this characterization, we perform data measurements through the experimental setup depicted in Fig. 4.3.

These data results show a 2.5 dB power penalty for 2x10 Gb/s data operation. When

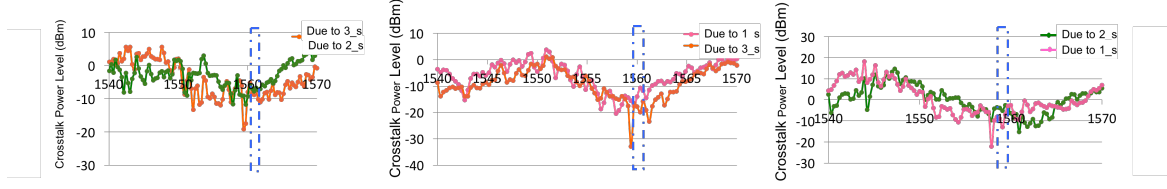


Figure 4.2: Crosstalk level of channels 1_s , 2_s , and 3_s going to 1_d , 2_d , and 3_d . Dashed lines indicate regions selected for best crosstalk levels across all three channels.

all three channels are activated, inclusive of the arm contributing a greater amount of crosstalk, we arrive at 3×10 Gb/s data operation and 7.5 dB greater power penalty. The crosstalk values measured suggest MDM muxing can be realized with power penalties < 1 -4 dB/channel. Imperfect mode-sorting in the MDM demux induced coherent crosstalk. This resulted in the ~ 5 –7 dB penalties shown.

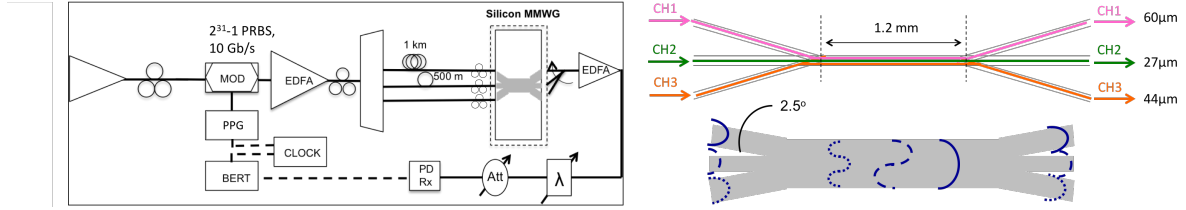


Figure 4.3: Experimental setup (left) and device dimensions (right) measured using an SEM

In order to improve performance, we optimize the device based on methods employed in the following sections through thermal tuning.

4.1.2 Alleviating Imperfection in Multimode Device

To optimize the asymmetric, y-junction angle for WDM operation, we both minimized crosstalk level and visualized the crosstalk regime for different angle combinations. At specific angle combinations of all the arms, low crosstalk levels will overlap more broadly. For broadband wavelength-division multiplexing to be performed, we examine the angle at which the N modes are designed.

The following device parameter optimizations are performed through RSoft simulations via ModePROP. The simulated and extracted n_{eff} are of different width waveguides. Then, we perform post-processing of the data in Matlab.

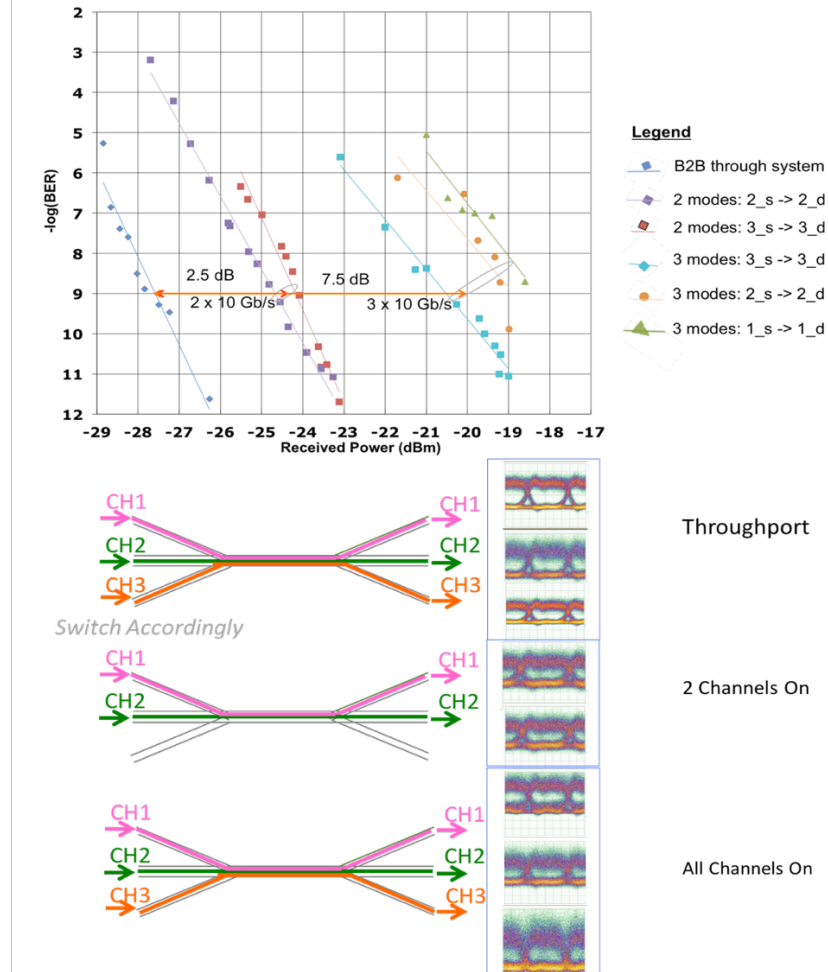


Figure 4.4: BER Measurement for 3-arm MMWG at 10 Gb/s operation and corresponding eye diagrams

ModePROP is used for a device with abrupt junction regions [Synopsys, 2013]. Instead of calculating solutions of Maxwell's Equations, the solver looks at the modes in each section of the structure. The expansion coefficients for each sector are determined by matching the fields of the interface and the boundary conditions.

We arrive at a particular width and angle combination. First, we sweep through n^2 possible sets of crosstalk levels, where n represents the number of angles examined. Each set has the wavelength sweep, and we choose to operate at specific wavelengths for later

Ang	Ang2
val1	val1
val2	
⋮	⋮
	val10

Figure 4.5: Table of variation of angles for the MMWG device

WDM operation.

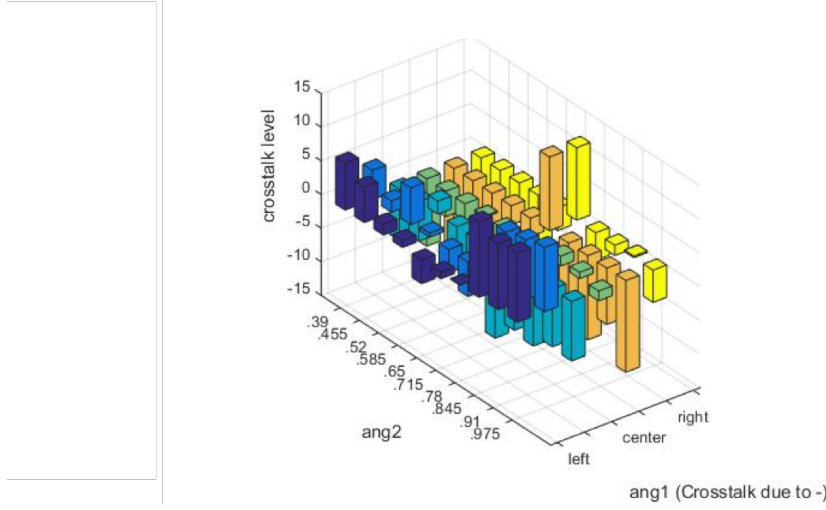


Figure 4.6: Visualization of crosstalk for particular angle variations of the 3MMWG

In Fig. 4.6, the crosstalk levels are illustrated by scanning through possible values for one angle and keeping constant the other angle. There are several issues with plotting the data in this way. It primarily comprises of the large amount of data to sort through. For this particular configuration at several wavelengths, viable operation is presented. Fig. 4.6 is simulated with the wavelength set at 1553.7 nm.

The length of the multimode regime was kept steady relative to the original two-multimode mux/demux. The simulated cross-beating at a wavelength resolution of 20 nm over 20 time steps are low across 1545-1565 nm regime. Note, the finer the resolution is, the greater the accuracy. As wavelength resolution is scaled, though, the simulation will take much longer if the modal resolution remains the same.

The n_{eff} values are 2.424, 2.447, and 2.4662 for the 3 modes. $\Delta\lambda$ can be directly

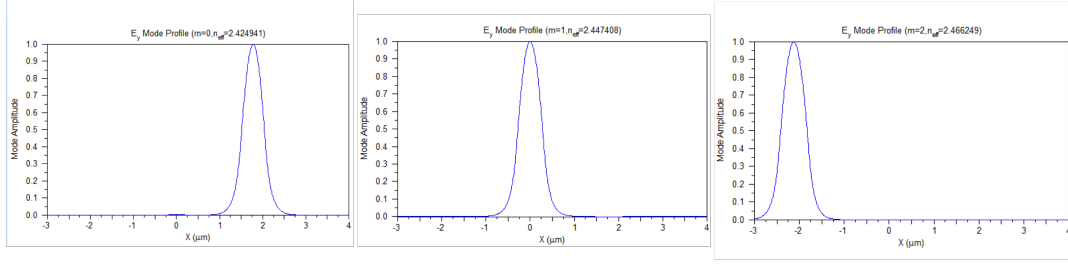


Figure 4.7: Three modes simulated across device of detailed dimensions

calculated from simulated n_{eff} values. The angle chosen after conducting this scanning process is 0.75° , relatively close to the angle of the other arm, which is 0.585° , when crosstalk values are low.

4.1.3 Accuracy of Fabrication

Device angles are designed to be on the order of $\sim 1^\circ$, while the writer beam has a tolerance equivalent to 2 nm resolution. The device SEM is shown in Fig. 4.8. This particular device was designed to have angles of 0.75° and 0.585° . Fig. 4.8a photo was post-processed, where the angle was edge detected using the Prewitt Filter (Fig. 4.8b). From here, this captured image was transformed with the Hough Transform (Fig. 4.8b). The lengths of the intersecting lines were extracted to calculate the angle of the device. These were calculated to be 0.545° and 0.357° , a 27 % and 38 % difference from design, respectively. Besides slight offset introduced from fabrication, various post-processing analysis methodology could be examined, which can be further fine-tuned.

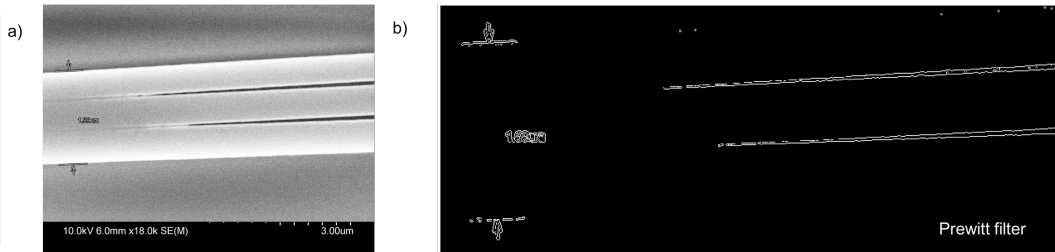


Figure 4.8: a) SEM of the resultant three-armed multimode multiplexer device and b) Prewitt filter for edge detection to computationally measure the angles via length approximations

Dynamic adjustment of the asymmetric, y-junction arms, as discussed in the next section, can also be considered during design.

4.1.4 Discussion of Need for Dynamic Adjustment

The ability to adjust spectral operation of one arm would likewise enable device operation to be improved post-fabrication [Chen *et al.*, 2016b]. As can be seen from the above sections, such capability could be important for overall system improvement.

We explore how accurately phase change can be performed. Phase change can be introduced in the form of a P-N junction to electro-optically introduce shift to the phase of the signal in the y-junction arm. This biasing mechanism can also be added in the multimode sector to shift every arm's wavelengths by a certain amount.

For the three-MMWG, a ± 2 dB difference between arms at a particular wavelength could occur so that the pair are within standard deviation of operation, yet the third arm has $> \pm 2$ dB induced. As this only occurs at several nm offset, the wavelength regime could be tuned to fix this discrepancy and match the performance across all arms.

Electro-optic tuning can be introduced through nonlinearities in the waveguide [Mrejen *et al.*, 2014], done by adding a PIN junction, which generates or depletes carriers between the two regions surrounding the waveguide, inducing a difference in refractive index of the material. Spectral tuning can also be done by thermo-optically introducing the shift in phase in the propagating signal [Chen *et al.*, 2012]. Simulations are performed using the latter method.

4.1.5 Introduce Variation in Arm vs. Multimode Regime

Variation is first introduced in the multimode waveguide region (Fig. 4.9a). With the thermo-optic coefficient of Si as $1.87 \times 10^{-4}/\text{K}$, change in temperature likewise induces change in refractive index at this rate.

If we were to mark a certain wavelength as a resonant wavelength, we can see the shift due to temperature change. Then, we introduce the tuning to the bus guide (Fig. 4.9a) or on one of the arms (Fig. 4.9b), resulting in the corresponding spectrum. We can note the difference in the slope of the spectral response due to the location of the heating region and

the source.

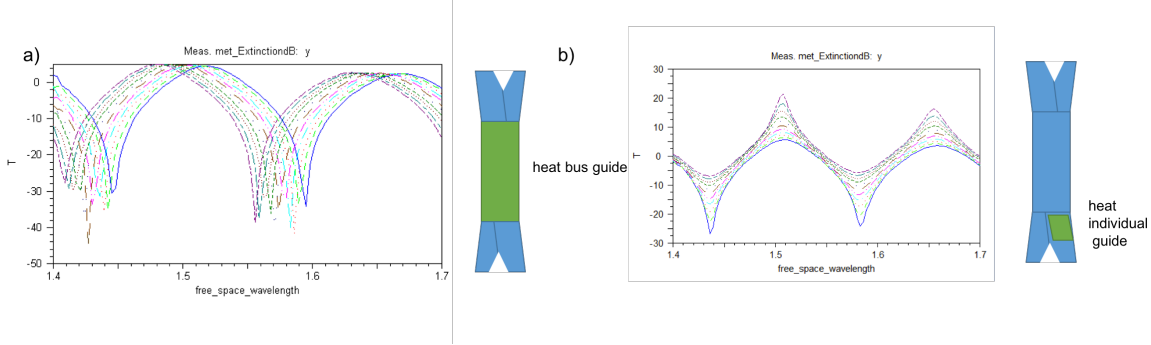


Figure 4.9: a) Spectrum when arm is thermally varied b) Spectrum when multimode body is thermally varied

4.1.6 Thermo-optic Control for Three Modes

The device simulated, as shown in Fig. 4.10, has a multimode length of $L=1.003$ mm with $w_1=550$ nm, $w_2=600$ nm, and $w_3=650$ nm. The angles θ_1 and θ_2 are 0.75° and 0.585° respectively. The geometry of the multiplexing arms induces a range of effective indices (n_{eff}) that then propagate as three different-ordered quasi-transverse magnetic (QTM) modes in the MMWG.

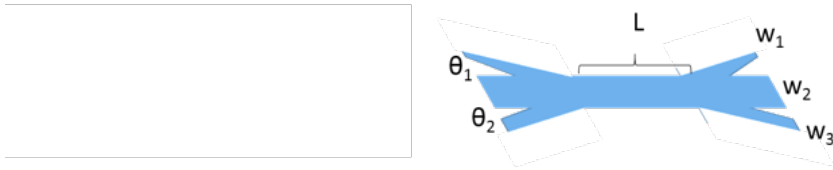


Figure 4.10: MMWG supporting three modes with dimensions $\theta_1=0.75^\circ$, $\theta_2=0.585^\circ$, $w_1=0.55$ μm , $w_2=0.6$ μm , and $w_3=0.65$ μm , and $L=1.003$ mm. w_3 arm is the Left Arm, w_2 arm is the Center Arm, and w_1 arm is the Right Arm.

The graph in Fig. 4.11 plots every possible combination of crosstalk on the throughport arms due to the neighboring arms. The crosstalk level is the difference in power seen at the throughport arm with respect to the crossport arm. The labels in the legend indicate the crosstalk contribution of one arm on the other labeled arm. The crosstalk value contributed by arm i can be expressed as:

$$CT(\lambda_o)_{arm,i} = 10\log_{10}(P(\lambda_o)_{throughport} - P(\lambda_o)_{crossport,i}) \quad (4.1)$$

where $P(\lambda_o)$ is the power in dBm at λ_o . This crosstalk value then translates to power penalty when we are performing system measurements [Rawaswami *et al.*, 2004].

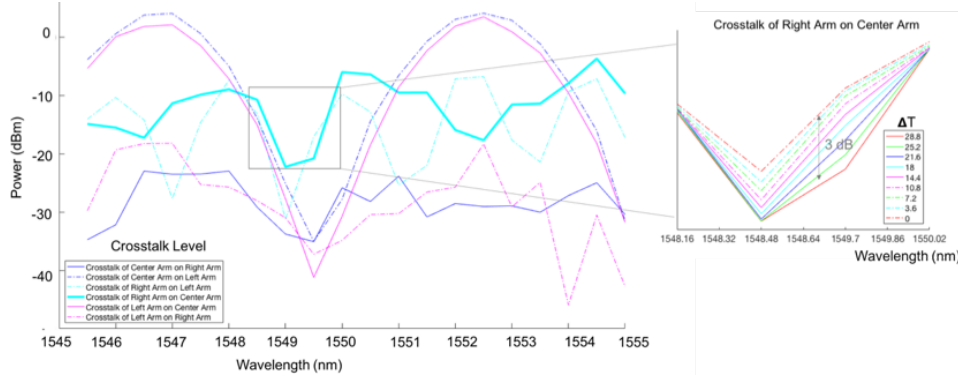


Figure 4.11: Crosstalk level at all arms of the device described here. The legend indicates the crosstalk contribution of the crossport arm on the throughport arm. The arm that is the main contributor to crosstalk has its crosstalk level drawn in bold. The spectral region investigated is boxed. By zooming in on that region, we see the resultant reduction in contribution to crosstalk by the right arm as it is thermo-optically induced.

From this particular graph, we can select $\lambda_o=1549.4$ nm as an operational wavelength. However, the largest contribution of crosstalk at this operational wavelength seems to originate from the source at the right arm. The closest dip due to interference of the right arm is offset from the selected λ_o by ~ 0.4 nm. A thermo-optic control is placed at this arm to shift the spectral regime shown in the zoomed-in region of Fig. 4.11. $\Delta\lambda$ is directly related to n_{eff} as follows with a similar derivation in [Uenuma and Motooka, 2009]:

$$p\lambda_o = \Delta n_{eff} * L \quad (4.2)$$

where p represents a positive integer and L is the length of the multimode waveguide. Then, waveguide dispersion is taken into account, resulting in the below equation and P replacing

p.

$$P = p - L * \partial_{eff}/\partial\lambda \quad (4.3)$$

Dips in the crosstalk regime as a result of temperature variation can be written in the form:

$$\frac{\partial\lambda}{\partial T} = (L * (\partial\Delta n_{eff}/\partial T))/P \quad (4.4)$$

At the selected right arm, we perform a temperature sweep over about 30°. The derived shift at the examined wavelength regime is about 0.043 nm/K. At 28.8°, we see a crosstalk value 3 dB lower than without thermo-optic tuning. It should be noted that the amount of thermal adjustment will vary across different modes. Additionally, finer resolution on the thermal study can provide more granularity in the spectral content.

The effect from the thermo-optic control is localized on one of the arms, as opposed to possible integration on the multimode region. Thermal isolation of the tuning region could also ensure other channels are not also affected by this active thermo-optic inducement [Masood *et al.*, 2012].

The parameter of interest for multimode operation is the difference in phase between all possible combinations of signals traversing across the different arms. Phase mismatch in our case can be represented by $\Delta\beta_{eff} = \beta_{arm} - \beta_{TO}$ that takes into account $\beta_{eff} \ll \beta_{arm} - \beta_{neighboringarms}$, where β_{arm} indicates the original mode propagation constant, and β_{TO} indicates the mode propagation constant with the additional tuning applied.

As multimode operation is realized through different designs, bandwidth continues to scale via spatial-multiplexing, and new tools can be developed for optimizing performance.

4.2 Scaling Capacity

One way of scaling aggregate data bandwidth is by standalone increasing bandwidth. The challenges that arise, then, is that the power needed to drive the transceiver circuitry is quantifiably higher. Furthermore, operation at a higher bandwidth will result in sensitivity misalignment.

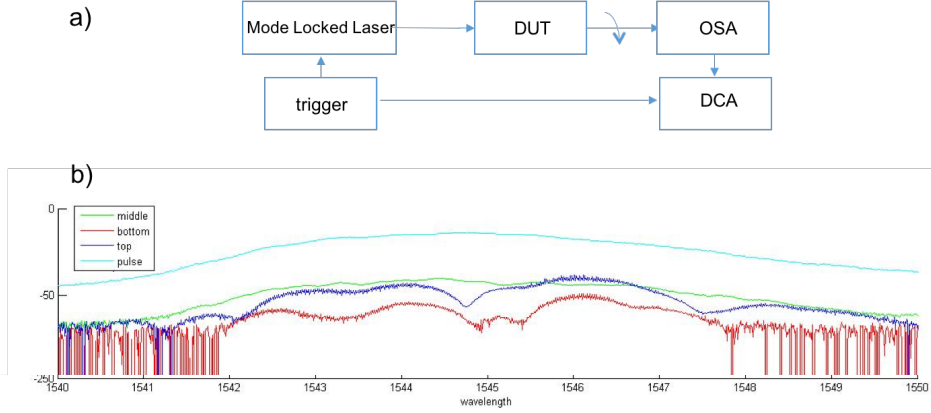


Figure 4.12: a) Experimental setup to take the b) frequency response of the 3MMWG device, in reference to the pulse scan itself

The main experiment at 40 Gb/s data across the 3MMWG is able to achieve 240 Gb/s aggregate data bandwidth by modulating each data channel on each optical pathway through the three-MMWG [Chen *et al.*, 2016a]. The wavelengths selected for this operation were 1547 nm and 1557 nm. Transmission spectrum through short pulses of 1ps duration traversing through the device can be taken in the time domain [Lee *et al.*, 2006]. The response for the Fig. 4.12a setup is shown in Fig. 4.12b, with the results of the pulse response through the system, as well as the transmission spectrum through the arms of the device. The receiver inside the Yokogawa OSA has specs [Yok, 2011], with the highest .05 nm resolution set for the scans.

For the experiment, the data is transmitted through the experimental setup of Fig. 4.14 in order to demonstrate high-speed data across the modal channels. While previous demonstrations showed 10 Gb/s data rate operation, here 40 Gb/s data is placed on top of each modal channel.

The front end and back end of the 40 Gb/s setup is described here. There are 2 CW

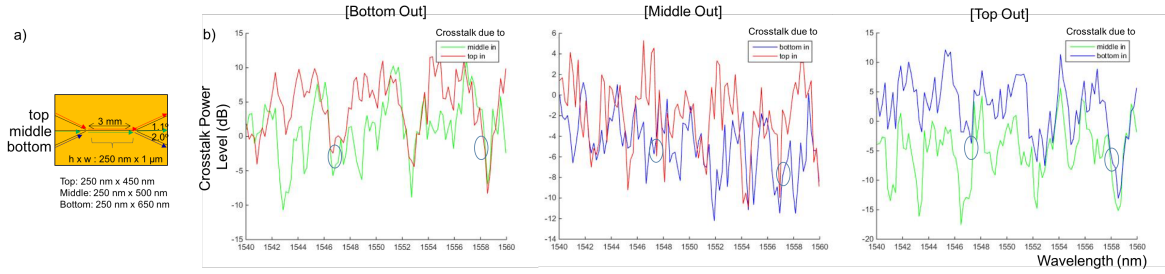


Figure 4.13: Wavelength scan for the 3MMWG device, with the wavelengths of operation circled in each diagram

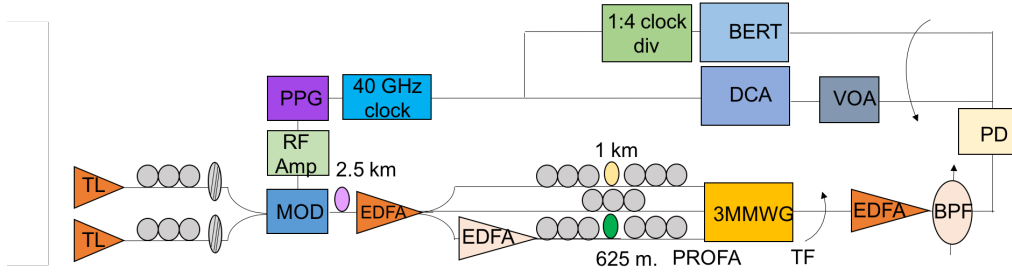


Figure 4.14: Experimental setup for 40 Gb/s data across three-MMWG

lasers multiplexed into a single fiber before the light paths are modulated with a Centellax pulse pattern generator putting a 40 Gb/s trigger into the clock divider that then injects the signal into the SHF 1-to-4 mux to recover the signal. A 40 Gb/s LiNbO₃ modulator is utilized. The 2 wavelengths are decorrelated by a spool of fiber before the signal is split into 3 pathways to launch into the 3 modal channels. Then, for each channel, we decorrelate the data that is on each pathway. Post-chip traversal, each wavelength and mode signal combination is recovered through a tapered fiber to be amplified, wavelength-filtered, and received with a PD for BER tests.

From the BER diagram in Fig. 4.15a, we see BER penalties of 6-10 dB, due to crosstalk introduced by the worst arm. The power penalty accrued varied from a combination of device and system variation. There were two system parameters of power to account for. First, due to the imperfect power coupling on-chip, a power difference at the input to the chip can be seen. Unequal performance is likewise seen along each pathway directed to each input of the device. Taking these two system parameters into account, we set the power level going on-chip to be acceptable for simultaneous MDM-WDM operation, as can be

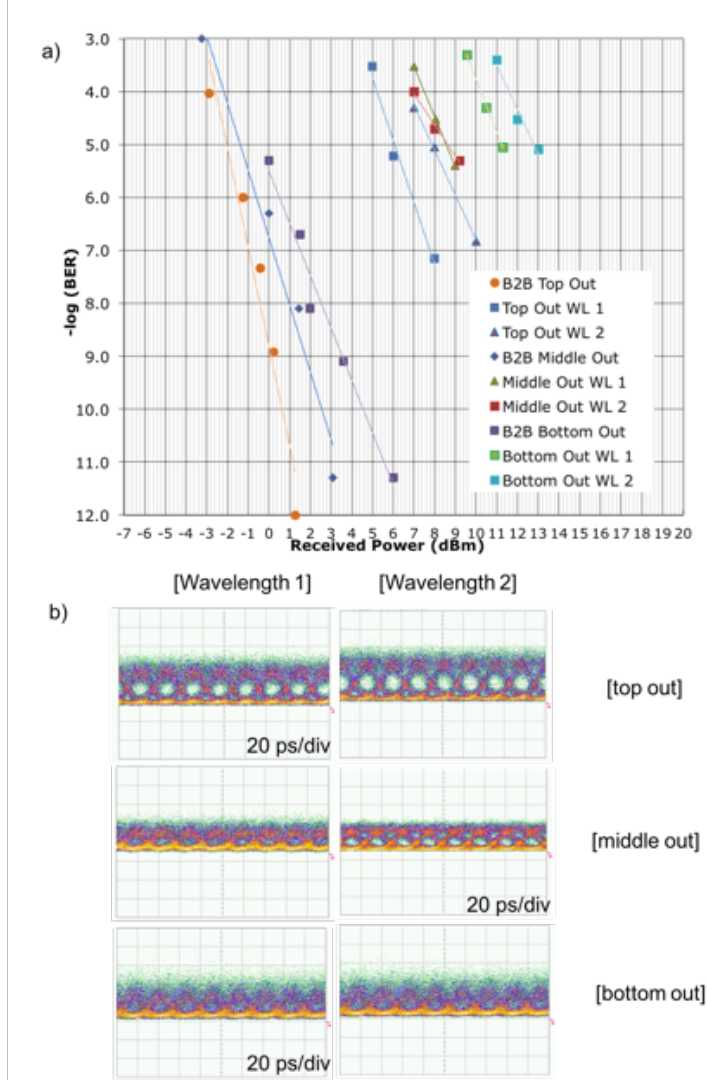


Figure 4.15: a) BER and b) eye diagrams of 3MDM-2WDM operation

seen from the wavelength scans. Operation was then at the edge of power requirements and upper bounded by receiver saturation.

Power penalty due to intra-channel crosstalk arises when there is imperfect mode confinement. In this case, for the chosen wavelengths, power penalty ranged from 7 dB at the 10^{-8} BER point to considerably lower bit error rate of 10^{-6} for the most impaired arm in the system, with the bottom arm seeing the highest level of intra-channel crosstalk. Low

crosstalk regimes matching all three modal arms had to be selected. Compared to the multimode waveguide support of two modes, there were fewer regimes with equivalently low crosstalk level. Coupled with the higher data rate, a considerably higher power penalty is accrued. To improve system performance, considerations for increasing fabrication tolerance can be investigated. The previous sections discussed how to effectively minimize this device imperfection. Furthermore, it should also be taken into account that at higher data rates, as noise becomes a problem, forward error correction (FEC) can be employed to bring down the bit error rate. Additionally, dispersion in fiber becomes inherent at higher data rates, incurring fiber impairments in the system.

4.3 Multimode Data Distribution via a Switch Fabric

In order to enable next-generation network-on-chips (NOCs) capable of supporting greater than terabits-per-second data rates for intra-chip and inter-chip communication, we can consider leveraging orthogonal optical domains. This will allow us to move towards reducing power consumption across the switch. Lower order switch elements like the 1x2 switch [Gu *et al.*, 2009] serve as the building block of NOCs [Gu *et al.*, 2009]. From such an element, architectures like Corona— which is a 3d many-core architecture that uses optics for inter-core and off-stack communication— have been built [Vantrease *et al.*, 2008].

Recent simulational work has found that photonic network-on-chips (NOCs) routing multiple modes simultaneously can decrease power consumption by as much as 75% average router power than the typical Corona architecture [Dang *et al.*, 2015]. Power utilization, the effectiveness of power usage in a data center, is inversely related to the number of modes.

With this defined motivation, routing of multiple modes simultaneously is demonstrated on the scale of the 1x2 switch. The exhibited device, which was fabricated through e-beam lithography and RIE, routes four data channels with < -16.8 dB crosstalk [Stern *et al.*, 2015a].

This is the first demonstration of switching multiple modes [Stern *et al.*, 2015b], with the switch routing four channels at TE_0 and TE_1 . The light is coupled into the routing waveguide, and much like the theory behind the design process described in Sec. 2.3.2, the

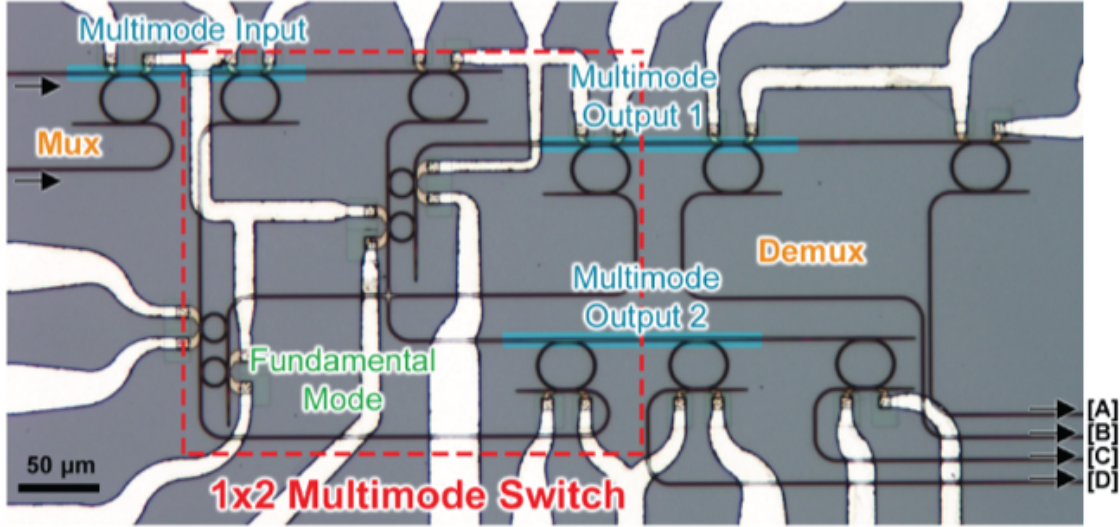


Figure 4.16: Top down view of multimode switch layout with inputs and outputs labelled

fundamental mode is phase-matched to waveguides of widths that specifically induce higher order modes.

The rings have a smaller radius of $8.6 \mu\text{m}$ (for a FSR of 10 nm), and these rings are tuned to resonance so that all the wavelength channels can be converted to modes.

BER measurements were collected for all possible channel permutations. Modal channels are decorrelated as elaborated in Sec. 3.1.1. Wavelength channels are decorrelated as explained in Sec. 3.1.2.1. The highest crosstalk configuration is examined. This occurs when each modal channel is "dropped" at the same output port. At $\text{BER} < 10^{-9}$, PP of 1.4 dB routing is shown when 10 Gb/s data is input separately. The switch exhibits an additional power penalty of < 2.4 dB when the four channels are routed collectively.

Some challenges that were experienced while taking these measurements could be attributed to the design of a cascade of microring resonators along the single waveguide path. Fluctuations in the power of one ring then affects its cascaded neighbors. Another issue is that the bandwidth of the last ring in a series of rings will be more filtered than the earlier rings.

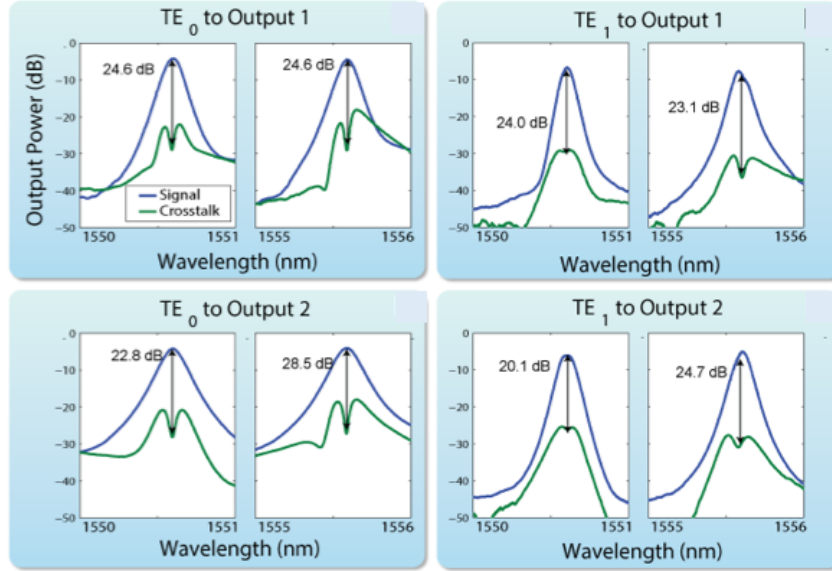


Figure 4.17: Crosstalk measurements for the different channels. Spectral profiles at both outputs for each of the four input channels, compared with profiles from interfering channels. Signal and crosstalk were measured individually with a CW tunable laser for configurations with the highest intermodal crosstalk, showing that it is below <16.8 dB in all cases.

An alternative for this mode switching design can be with an eye towards having a 3d stack. The main challenges lie in the steps additional to the CMOS-process that need to be introduced to integrate multi-layer photonics [Sherwood-Dros and Lipson, 2011]. Doing multimode operation in stack would couple the elimination of crosses (potential sources for loss factor) with the reduced power consumption of lasers per wavelength. These are future-looking capabilities that should be kept in mind.

4.4 Coupling and Packaging Considerations

For the experiments in this chapter, and those described in the prior chapter, a PROFA that had a $38 \mu\text{m}$ pitch and $0.08 \mu\text{m}$ average error was utilized. Typical mode field diameter (MFD) is $10.4 \mu\text{m}$, and the waveguide was designed to couple to this exact pitch.

Visible variation in the level of flatness along the edge of the chip was minimized by sanding. This aided to likewise minimize reflections inducible by additional edge roughness,

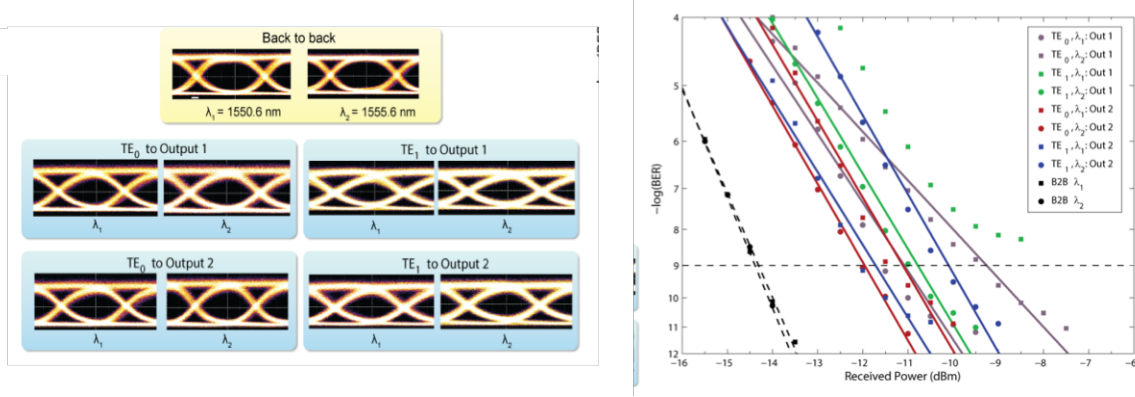


Figure 4.18: Eye diagrams and BER measurements for multimode switch

made even more acute by the need to simultaneously couple multiple modes on-chip.

The PROFA sits on a goniometer that provides the angular adjustment needed to align the coupler to the chip waveguide input. Coupling is a problem with a two-fold solution. The insertion loss for a multichannel device might vary. As such, the PROFA can be coupled to the device with this inherent imperfect equalization in mind. Attenuation can also be introduced across the pathways such that the channel where greater power is needed is provided relative to its neighbor.

Accurate coupling is a research area in and of itself. If the fiber is misaligned with the device port, over or under coupling could be induced, as is examined in [Bozinovic *et al.*, 2013].

For any object's commercial viability, the process by which device packaging is accomplished must be standardized. Since the device we examine has few I/O considerations, the additional level of complexity might be the attachment of the PROFA to the coupling regime, and similar designs have been shown in [Kopp *et al.*, 2015].

4.4.1 Thermal Variations

In packaging, thermal variation can become an issue, due to the presence of the laser source. As a partial study of thermal effect on the two arms of the multimode waveguide, the device was put on top of a thermoelectric controller (TEC). Similar type measurements have been

done in [Yasuoka *et al.*, 2015], where temperature change is induced by this implementation of Peltier effect.

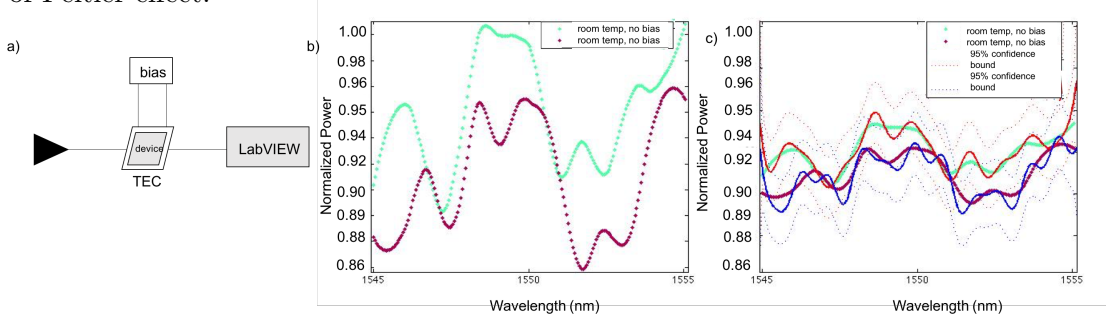


Figure 4.19: a) Experimental setup with thermal electric controller (TEC), b) wavelength scan at same temperature (0V bias to the TEC), and c) fit of sum of sine functions with both graphs matching fit parameters $< 6\%$

By applying bias to the platform, temperature change is introduced across the TEC surface, and, by extension, the semiconductor. The device is placed on thermoconductive tape towards the center of the TEC.

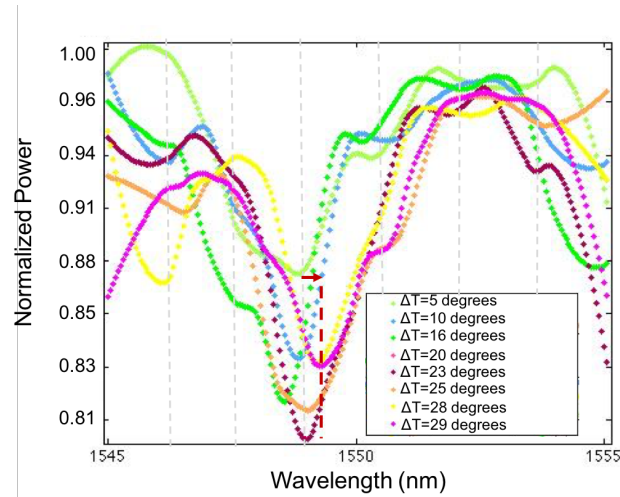


Figure 4.20: Normalized wavelength scan at varying bias, fit to smoothing spline parameter at < 0.55 with specific TEC bias of 0.1 V and 0.9 V, with a general red-shifting trend, and the red arrow overlay on the graph indicating the measured shift over 30 degree change

As a first test, several scans were taken over a span of a couple of minutes without biasing the TEC to gauge the inherent drift in the system. Fig. 4.19b shows several normalized

spectral scans, with the plots smoothed. The fit in Fig. 4.19c is to a sum of sine functions, which follow the curves, and the red and blue dotted lines indicate the 95 % confidence bound. Whilst the two measured curves vary vertically, lateral variation is less visible than the case when the temperature is varied in the region of the chip with the "hot surface" contacting the Si platform (Fig. 4.19a).

A sequence of incremental voltages were applied to see how much temperature change is induced. When 0.1 V bias (Fig. 4.20) has been applied, according to [Marlow Industries,], there's a 5°C temperature change from no bias having been applied. With an approximately 1 V bias applied, there is about 29°C in temperature variation. The exhibited shift if we were to look at the dip, is on the order of approximately 0.4 nm/30 degrees, with the shift mainly occurring with > 30 degree change. Further measurements can be conducted for more exact figures and sophisticated temperature source emulations can be conceivable.

In the interest of reducing wavelength drift due to thermal variation, on-chip considerations might need to be made, as there is the potential need for reduction in the thermal effect on operation as well as thermal stabilization schema.

4.5 Main Takeaways

The capacity supported through a MMWG is expanded by scaling the modal arms, as well as increasing data rate across each of these arms. Upon expanding device channel support from two to three arms, a slight mismatch in the third arm can increase crosstalk contributions considerably, especially when increasing data rate, so a methodical way of designing the asymmetric, y-junction by considering fabrication variations is considered. Correspondingly, several additional solutions to increasing wavelength regions of tolerance are explored. Specifically, device optimization targeting wavelength regions of operation and phase variation across the device is examined. We compare fabrication results with the designed device parameter favorably. Further, we simulate thermo-optic operation for phase-shifting the modes to operate in the desired wavelengths of operation.

In order to accommodate for system-level utilization of MM, considerations for a MM switching mechanism is experimentally demonstrated. 10 Gb/s data is propagated through

a 1x2 microring-based switch. Beyond component elements, the mechanism for coupling to a MM-supporting device is considered in terms of packaging viability. The issue of thermal effect on MMWGs is examined with possible future studies into increasing thermal tolerance depending on the source of thermal instability.

In order to continue to improve MM operation, we have turned to examining device optimization. Such considerations are important for continuing to improve device performance, which when scaled to a larger system-level network, can impact overall system performance.

Chapter 5

Power Saving Analysis

Electrical power consumption dominates the power overhead within datacenters [Heck et al., 2011]. By using spatial multiplexing, the number of lasers employed can be reduced by the number of modes and/or polarizations introduced on-chip. Since energy efficiency of an optical system is largely dictated by the power dissipation due to the laser source [Ophir et al., 2013], research adaptable for future technologies must push towards reducing the power per bit metric. In this chapter, we will analyze laser power saving in an on-chip, multimode-supporting system.

5.1 Power Analysis in Optical System

A significant motivation for MDM can be expressed in the following chart, which illustrates the costly power consumption of lasers relative to other components in the optical system.

Several assumptions were made in compiling this chart. In an optical link with OOK data being sent, and data rate set at 10 Gb/s due to the maturation of electronics in that range, we estimate 10 fJ/bit for 1 Vpp modulator levels. The microring resonator of $Q \sim 10,000$ has 3.5 dB insertion loss and 6.45 dB extinction ratio whereas for passive componentry, different estimates would have arisen [Ophir et al., 2013].

For electronic circuitry, a trans-impedance amplifier (TIA) exhibits 0.4 pJ/bit, with the limiting amplifier (LA) componentry exhibiting several pJ/bit. Coupling mismatch accounts for 1.5 dB insertion loss.

Finally, the laser source, with output power of 0.70 mW, accounts for 5.6 pJ/bit at 1% efficiency. Therefore, the majority of power consumption comes from the laser.

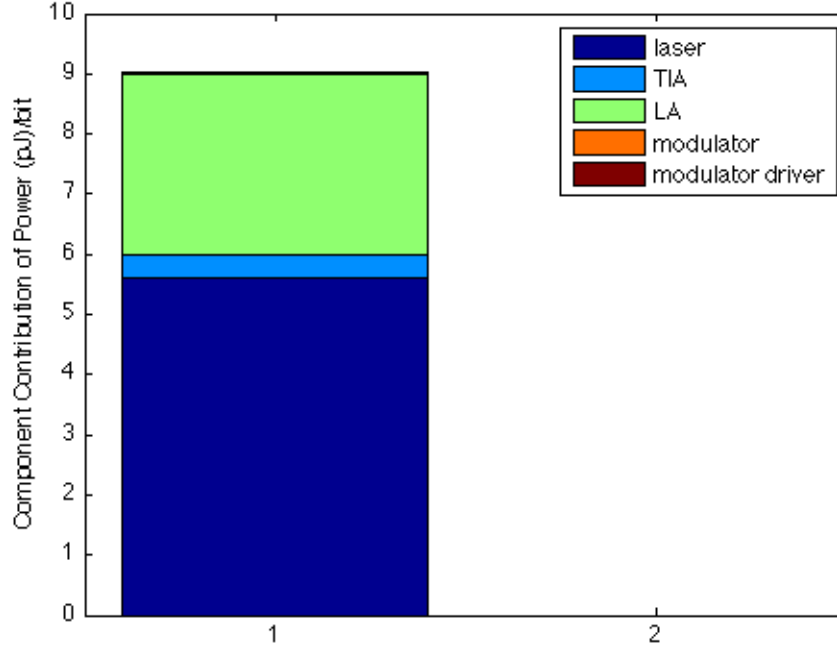


Figure 5.1: Power Consumption Due to Each Component Geared Towards Passive MDM Setup

5.2 Laser Power Analysis for MDM/PDM Channel Addition

We explore attaining a set bandwidth proposed by current Ethernet standards [McDonough, 2007], through MDM operation. Furthermore, the effect of adding on the use of modes to replace wavelength channels is examined [Chen *et al.*, 2015a].

There are several different kind of lasers we can look at for performing laser power analysis. The primary metric for these lasers is the threshold voltage, which indicates the point at which acceptable injection current level is reached for the system, primarily attaining detector sensitivity levels.

First, we look at the micro-disk laser (MDL). This laser is bonded to a III-V die. Details of laser dimensionality are given in [Roelkens *et al.*, 2010], with its characteristic provided

in Fig. 5.2. For calculation purposes, we will decide on a reasonable injection current to operate at just about the drive voltage so that the laser is operating in the linear regime.

This is in comparison with the hybrid ring resonator (RR) laser [Keyvainia *et al.*, 2013].

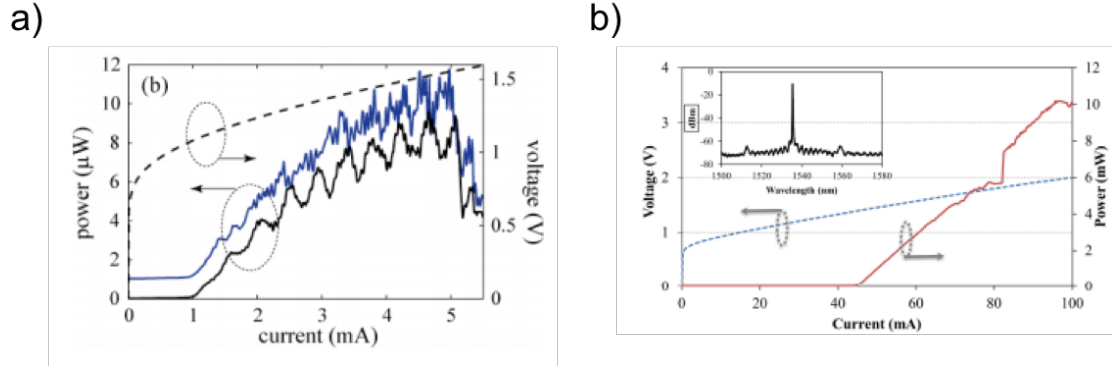


Figure 5.2: a) MDL from [Roelkens, 2010], noting the dark line and b) hybrid ring resonator from [Keyvainia, 2013] showing laser I-V characteristics to determine electrical power consumption

For both cases, our calculations are done with the following equations. The $I_{threshold}$ and $V_{threshold}$ represent the values at which we set the laser to operate at with WDM. The $I_{operating}$ and $V_{operating}$ are the values at which we set the laser to operate with each successive orthogonal dimension used:

$$P_{electrical} = I_{threshold}V_{threshold} + I_{operating}V_{operating} \quad (5.1)$$

$$P_{savings} = mwP_{electrical} - mI_{threshold}V_{threshold}, \quad (5.2)$$

$m \in \text{modes}$, $w \in \text{WLs}$

$$\%P_{savings} = savings / mwP_{electrical} \quad (5.3)$$

For the MDL laser, if we set the operating point to 3 mA, the lasing source would be emitting 6 W of optical power. For 32 lasers, this would be 96 mW of power consumed. Then, with 2-MDM, we operate at slightly higher optical power, driven to 4 mA. This consumes 76.8 mW, and with PDM added on, driven to 5 mA, the laser consumes 60 mW. This is a 36 mW reduction from the case with corresponding bandwidth attained through WDM.

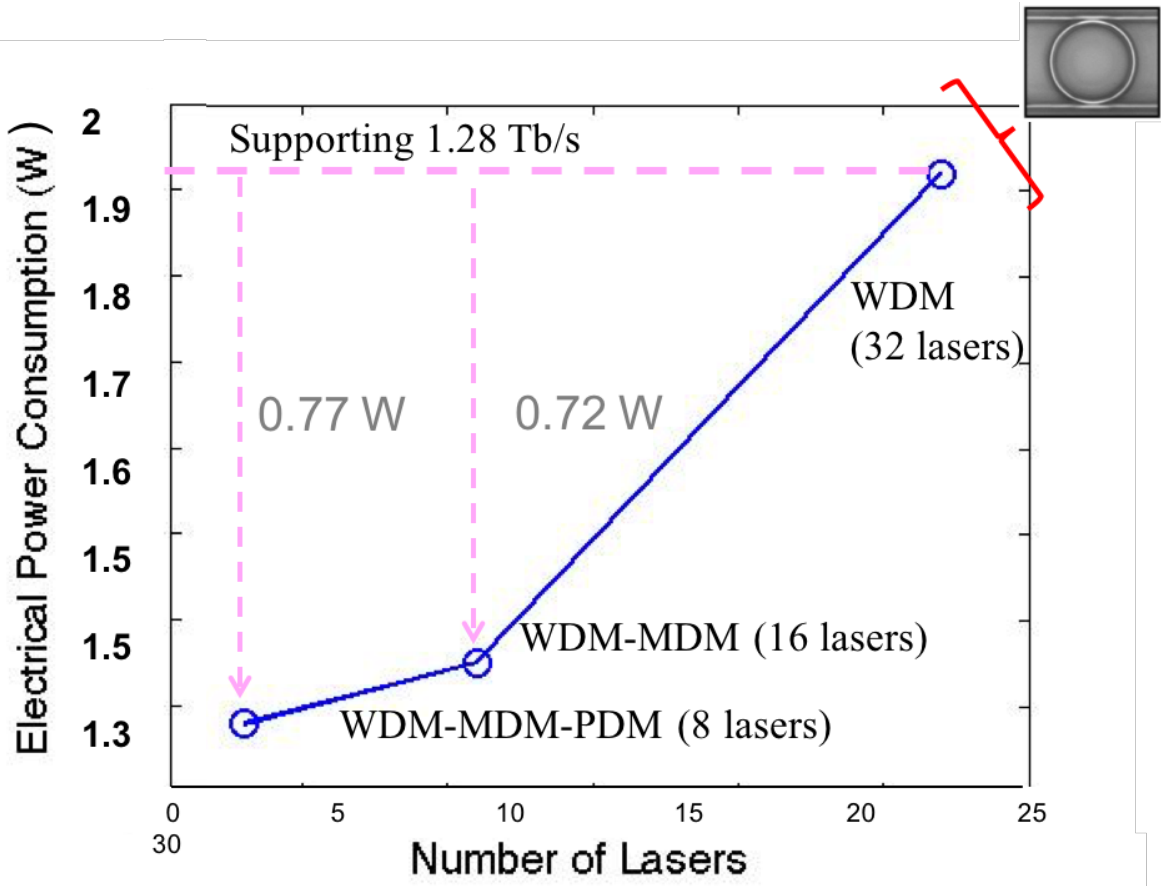


Figure 5.3: Power consumption of lasers for different multiplexing schemes

For the hybrid ring resonator, if we assume an operating point of 3 mW of optical power, which is within the linear regime (60 mA), for the 32 laser case, 1920 mW is needed to power such a WDM channel. When we employ 2-MDM, we can cut the number of lasers in half and still attain the same bandwidth capacity. This means that with 16 lasers emitting, and driving to 75 mA, we'd be consuming 1200 mW of power. With PDM added

on, and driving to 80 mA, the laser would consume 1152 mW. This is a 768 mW reduction in electrical power when 2MDM-PDM is employed in the system instead of WDM.

On-chip spatial multiplexing then engenders a potential area for reducing power in a system. The number of lasers used is reduced as a result of employing multiple modes through MDM or pol-muxing. Electrical power is reduced by the threshold power of each laser saved, thereby yielding a significant energy saving, while scaling bandwidth. We look comprehensively at power savings relative to each laser. Fig. 5.3 graphs the hybrid RR laser scheme.

In an optical system where the majority of power is consumed by the laser, employing multimode operation can allow for a reduction of lasers. This can minimize significant footprint in energy consumption as highlighted in this section. It should be noted that there is a power penalty hit taken from additional wavelengths or modes in a waveguide. However, through further improvement to device fabrication, this figure will only diminish, and it is not an exponential increase in penalty as orthogonal channels scale, much like it is for lasers' power requirements. A 40% reduction in power for the 2MDM-PDM case using a RR laser and a 37.5% reduction in power for the 2MDM-PDM case using a MDL laser are derived. By combining different orthogonal domains together to traverse data, power reduction can be attained.

5.3 Main Takeaways

At the root of adoption of a technology is the capability for its introduction to reduce costs to the existing system. In this chapter, we illustrate the presence of high power consumption in an optical system due to the laser source. While MDM can scale the number of orthogonal modes supported on-chip, it can also be used to maintain bandwidth at much reduced power by saving on the corresponding laser drive power for WDM operation. We illustrate this cost-saving benefit by analyzing laser specs for a sample metric, thereby providing compelling motivation for adopting MM structures in optical network-on-chips, while future direction in this power analysis could examine the benefits of using MDM versus other forms of multiplexing in the face of desired types of cost reduction. The systematic analysis shown

here presents on-chip MDM as both a viable and attractive technology.

Part II

Si Photonic Subsystems

Chapter 6

Optical Network Architecture

In this next part, we examine photonic devices for the purpose of integrating into the modern data center. Modern data centers utilize optical fibers for long haul (of lengths $<$ backplane traces, [hdp, 2009]). Anything on a much shorter length is still being quantifiably demonstrated on a deployable scale [Kachris et al., 2013]. Furthermore, use of optics on an intra-datacenter scale promises to be an energy-efficient path forward, reducing electrical-optical-electrical conversions through a closer integration of photonics with electronics. Optical switches compose an important building block in this realm of datacenter network operation.

We envision and realize the use of a Si Photonic mach-zehnder interferometer-based switch fabric from a dynamic programmable level for data multicasting and dynamic power reallocation as well as exhibit across it an application-level switching topology.

6.1 The Optical Switch

At the core of a datacenter is the switch fabric. Development of active optical cables, electrical components, and optical devices occur in parallel. Considerations made in designing and utilizing optical devices in this fast-changing environment must take into account a multi-faceted amount of parameters.

On a purely physical level, different photonic switches have been demonstrated. These include microelectromechanical switching (MEMS) [Han et al., 2014], arrayed waveguide grating (AWG) switching [Asakura et al., 2015], mach-zehnder interferometers [Yang et al.,

2010], and ring resonators, electro-optically switching [Soref and Bennett, 1987].

Control of these different types of devices will all require active monitoring. Determination of how these devices ought to integrate control plane signals is an area that needs to be examined. Aside from static control, future-looking photonic devices will need to be managed in a dynamic environment, both in terms of power fluctuations in a data center [Tang *et al.*, 2009], to minimize downtime of a path, and lowering power consumption of the devices themselves, to compete in terms of technological adoption costs.

6.1.1 2x2 MZI Switch

The switch element that we focus on in [Chen *et al.*, 2015a] is a MZI. It operates as a device that couples in light and splits it into two paths. One path has a phase modulator, to alter its path length relative to the other path. This dynamic arm has a PIN junction that will induce carrier generation when one side is biased. The movement of charge carriers from one side to the other generates an electric field, which in turn changes the refractive index of the material. This action causes the path length to shift on the one arm relative to the other arm's path length, resulting in a different amount of power seen at either output ports of the MZI. When light meets at the output combiner, the power is either constructively or destructively summed, which outputs as either a 1 or 0, respectively, or some subset if the interference is incomplete.

In order to characterize the 2x2 element [Chen *et al.*, 2014d], a dither signal is applied on top of the input electrical bias and the corresponding output is looked at in the optical channel. The low frequency dither signal doubles in frequency at the inflection points of the switch. Places where the signal amplitude maximizes serve as the quadrature point of the switch. Likewise, the phase differs for the different slope locations. Prior instances of using dithering include for laser cavity initialization or dynamically stabilizing MZIs [Wang and Kowalczyk, 2010].

The 4x4 switch is composed of these 2x2 elements. Such a precise characterization of the 2x2 element allows us to extend the procedure to the higher-order 4x4 stage, where we no longer have the luxury of seeing the output of each switch output. Rather, the signal traverses through three stages total before we glimpse the signal. (Future iterations of the

device could do well to place a photodetector at each stage in the multistage cascade of MZI elements. The downside to this is the hit on power resulting in a reduced overall power). Power must be enough in desired switch arms for the dithering characterization to be performed.

6.1.2 2x2 Switch Layout and Results

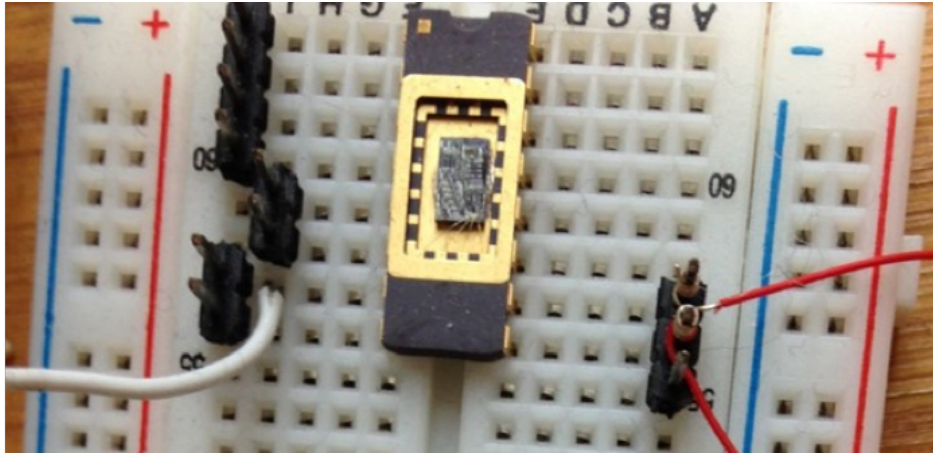


Figure 6.1: 2x2 MZI carrier bonded to the socket

In order to lower added resistance from electrical probes and contact pads [Zhu *et al.*, 2013], the device was packaged using wirebonding at Columbia Nanoscience Institute. In Fig. 6.1, the device has been epoxied to the top of a Au chip carrier, with the electrical pins wirebonded to the contacts on top of the device.

We then apply the electrical voltage to the PIN of one arm. In order to locate the precise phase response at specific bias values, a dithering signal is applied on top of the phase modulator. Fig. 6.2 shows the optical power output one arm of the device upon applying the dither signal.

6.1.2.1 Multicasting with the 2x2

The multicasting functionality for variable power distribution to either arms of the 2x2 MZ-based switch is shown in the Fig. 6.3. The power to either arms are adjusted by varying the bias placed on the PIN junction of the MZ. Then, these are mapped onto the FPGA

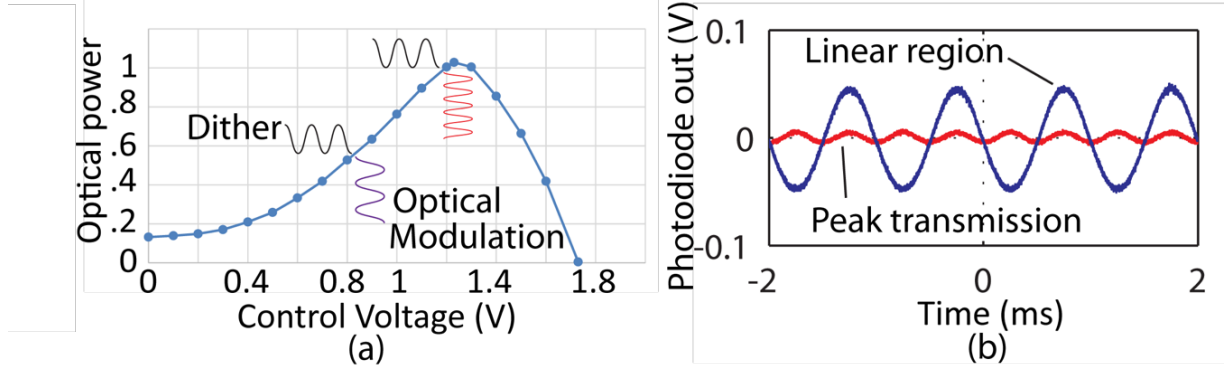


Figure 6.2: Using dither to find precise switch states. a) Near the inflection point at the transmission peak the optical modulation doubles in frequency due to the phase reversal. b) PD output connected to output 1 as MZ is dithered by a 100 mV_{pp} , 1 kHz signal. Detected modulation doubled to 2 kHz at precisely the peak transmission.

logic to control the switch with ease in configurability. Specifically, the peak inflection point of the switch is determined, and the percentage p of that value would be equivalent to a $10 \cdot \log_{10}(p \cdot 0.1)$ offset from this maximal power value.

These scans are the result of launching light from a broadband source (BBS) through a polarization controller (PC) onto the chip. The MZ can tolerate the power rationing with relatively uniform operation due to the broadband nature of the device.

6.2 4x4 Switch Element

6.2.1 Initialization

Initialization is required to determine the operating voltage for all switch positions because each stage of the device starts from an unknown position between cross and bar states. This random initial state results from variations in fabrication processes and environmental fluctuations in temperature [Kopp *et al.*, 2011].

We pass a single laser through input 1 of Fig. 6.5b and observe the power level at the four output ports. If we can set each stage to a guaranteed cross or bar state, the states through the switch become defined.

First, the final MZI stages of MZ5 and 6 in our topology are set to the cross or bar

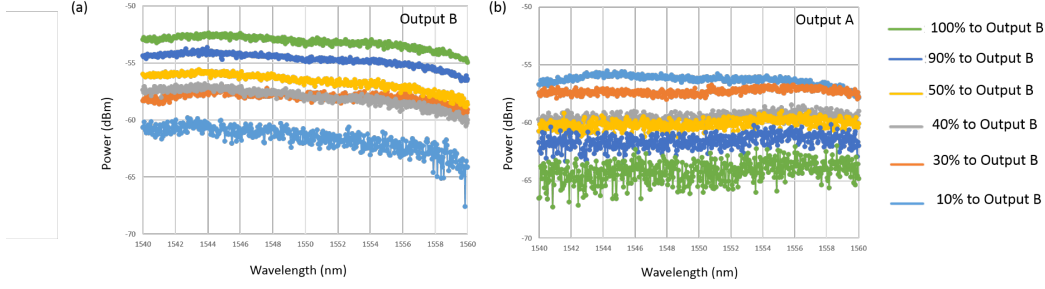


Figure 6.3: Incremental switching shown with basic 2x2 unit where light is injected at Input 1 and power seen at either outputs A and B are varied by biasing the junction. The resulting spectrum sweep is shown in (a) of Output B and (b) of Output A. The percentage labels are with respect to the peak power of Output B.

state. Next, we move backward to set MZ3 and 4 in the same manner. Finally, MZI is tuned to concentrate power into just one output port. Tuning correctness is verified by injecting light into another input port and seeing if power is switched accordingly.

The 100 mV_{pp} dither is applied to the PIN driving signal. The output optical signal is then modulated by the MZI structure. The optical modulation changes phase when the dither signal goes beyond inflection, doubling frequency. Again, at the inflection point, the cross or bar states occur.

6.2.2 Discussion of Non-Blocking Topology

For support of many transmission routes simultaneously, the traversed paths may need to be rearranged to become non-blocking [Daly, 2004] [Yang and Masson, 1991]. As a rearrangeably non-blocking Beneš topology, this switch can address several paths simultaneously [Pat, 1998]. The non-blocking characteristic for multicasting depends on how often paths cross at a MZI element [Yang and Masson, 1991] [Yang, 1998]. Additionally, a greater number of middle-stage MZIs can provide greater freedom in the paths that the multicasting route is set to traverse. While the total device area will be larger, a greater number of multicast routes will be possible under this configuration.

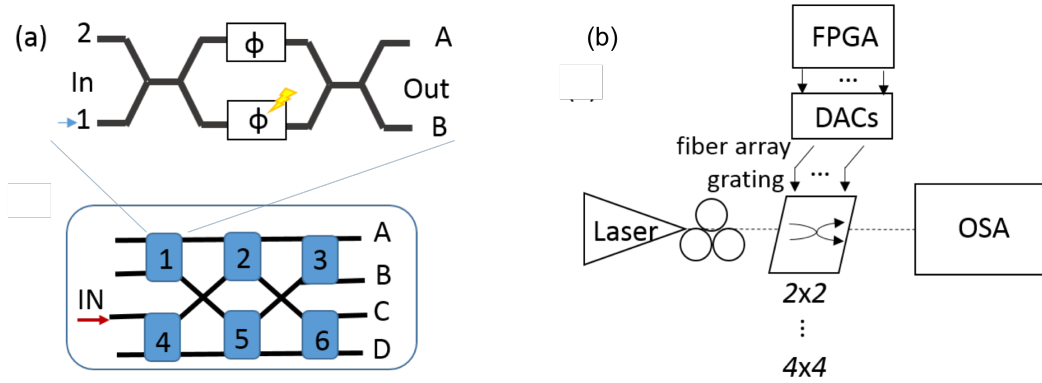


Figure 6.4: Switch layout and experimental setup. (a) 2x2 topology, single MZI with 4x4 topology having six MZIs configured into three stages, (b) setup for optical spectrum characterization of variable power allocation to output ports

6.3 Intelligent Power Algorithm for Power Reallocation

With the MZI-based switch thus characterized [Chen *et al.*, 2015b], we utilize it as part of a dynamically programmable platform.

Data centers are now consistently composed of a range of hundreds to two thousand nodes. In order to route the data in these networks, optical switching from the packet level or time domain multiplexing has been examined. Another method would be to utilize flow switching and overlay the OCS on top of the EPS [Zhu *et al.*, 2015].

Considerations need to be made when using the optical setup. Optical power level throughout the network is one parameter that needs to be maintained. Depending on the kind of data being sent, as well as the pathway taken before reaching each node, power levels will vary among paths.

Improving the dynamicity of the system can help to minimize downtime, which can be very costly. Studies have shown that as demand scales, downtime cost can escalate to \$7,900 per minute [Verge, 2013]. By employing an intelligent power algorithm, we can account for the dynamic needs of a system.

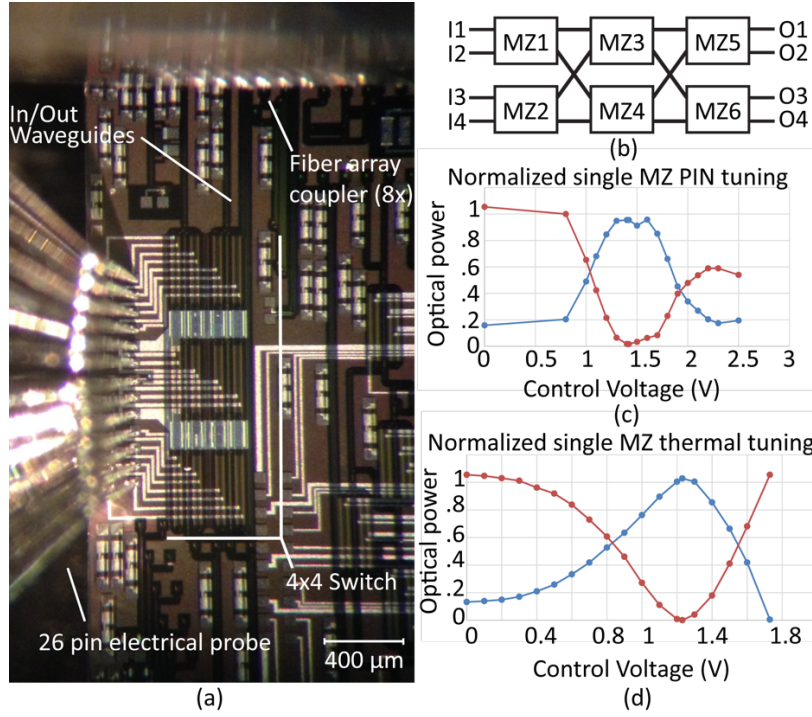


Figure 6.5: a) Microscope image of device. Center shows six 2×2 MZI switch stages with left and right arms. b) Benes switch topology: input/output and stage labeling convention for device. MZ6 is upper right MZI switch and MZ1 is lower left in a). c - d) Red and blue curves show normalized power detected at the two output ports of single switch stage as control voltage is adjusted. Switch normally starts in cross state with no voltage applied. PIN tuning in c) shows increased carrier induced losses increase at higher tuning voltages. Multicast operating points are near crossing point of curves.

6.3.1 Control Plane for Demonstration of Power Equalization

Dynamic control of data signals through the Si photonic switch matrix is demonstrated using the Xilinx Virtex-5 programming interface. Two resource allocation schemes are presented, where power is varied along each of the supported pathways in the switch fabric. The schemes are defined as *ordinary*, where the power at each MZI in the switch fabric is set to 50:50 for either output ports, and *dynamic*, where the power at the final destination of the switch fabric is equalized among clients. These two possibilities are looked at to examine a static power scheme versus a dynamic one, finding advantages and disadvantages for each.

A control algorithm is described to dynamically reallocate optical transmission power as loss changes along a given path. Integrating real-time power monitoring and checks for power reallocation through the control platform algorithm is shown and discussed here as well, with power reallocation explicitly demonstrated.

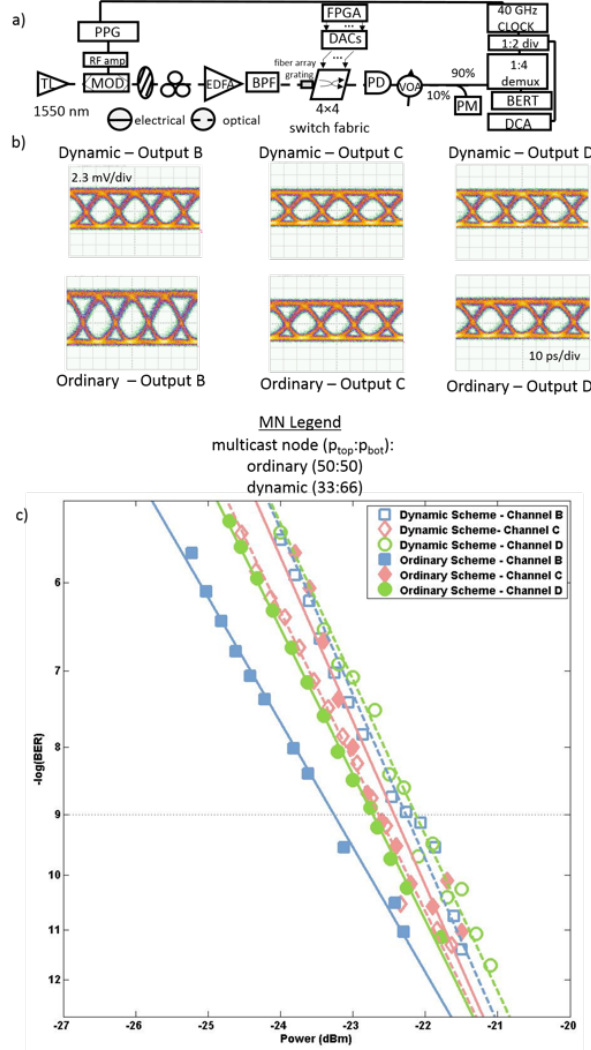


Figure 6.6: a) Experimental setup; b) Eye diagrams, and c) corresponding BER measurements of 40 Gb/s error-free dynamic multicasting across the 4x4 optical switch fabric

Previous data center control algorithms did not account for optical path or power budget variation [Li *et al.*, 2014] [Stabile *et al.*, 2016]. This particular scheme rebalances power among various pathways during multicast data transmission. Multicast signals exhibit

the one-to-many traffic pattern prevalent in search engine algorithms and video-streaming applications [Das, 2012], among other applications.

6.3.2 Experimental Setup

First, data is modulated at 40 Gb/s onto a 1550 nm CW laser source using a LiNbO₃ modulator. A pulse pattern generator (PPG) puts out a $2^{15}-1$ pseudo-random bit sequence (PRBS), which is amplified, and then serves as modulator input. The light path is amplified with an erbium-doped fiber amplifier (EDFA) and then passed through a filter tuned to the operational wavelength in order to remove the amplified spontaneous emission (ASE) noise. This signal is launched on-chip through a fiber array/grating coupler. A Xilinx Virtex-5 FPGA is used to program the switch fabric to the values previously determined through the initialization process. The values are passed through digital to analog converters (DACs). Different multicast operations can be obtained with the control system in place.

We show that we are able to transmit data through the switch *via* multicasting as described [Chen *et al.*, 2016c]. Primarily, a node is arbitrarily chosen to multicast from. The multicast node (M.N.) has its voltage bias varied on the MZI arm. The experimental diagram and resulting BER tests are shown in Fig. 6.6.

Both ordinary and dynamic switching are examined using this switch fabric. Variable power allocation is accomplished by programming the fabric to perform 1-to-3 multicast at a particular biased node. This multicast node (M.N.) is defined as a MZI element whose bias is varied so that the power exiting its output ports determine the power from the final two device outputs. The output power ratio is acquired by adjusting the M.N. from 50:50 to 33:66. While the M.N. is chosen in this demonstration without emphasis on the specific stage being used, use of the first or last stage for the M.N. could result in a greater number of possible routes [Masson and B. W. Jordan, 1972].

Signals are then recovered by using a PIN-TIA photodetector (PD), which is connected to a 1:4 demultiplexer and selector followed by the 1:2 divider for bit error rate (BER) tests (Fig. 6.6c). Eye diagrams are acquired with the digital communication analyzer (DCA) (Fig. 6.6b). For BER measurements, 10% of the received power is tapped out to the power meter (PM) to be monitored, while 90% of the received power is going to the bit error rate

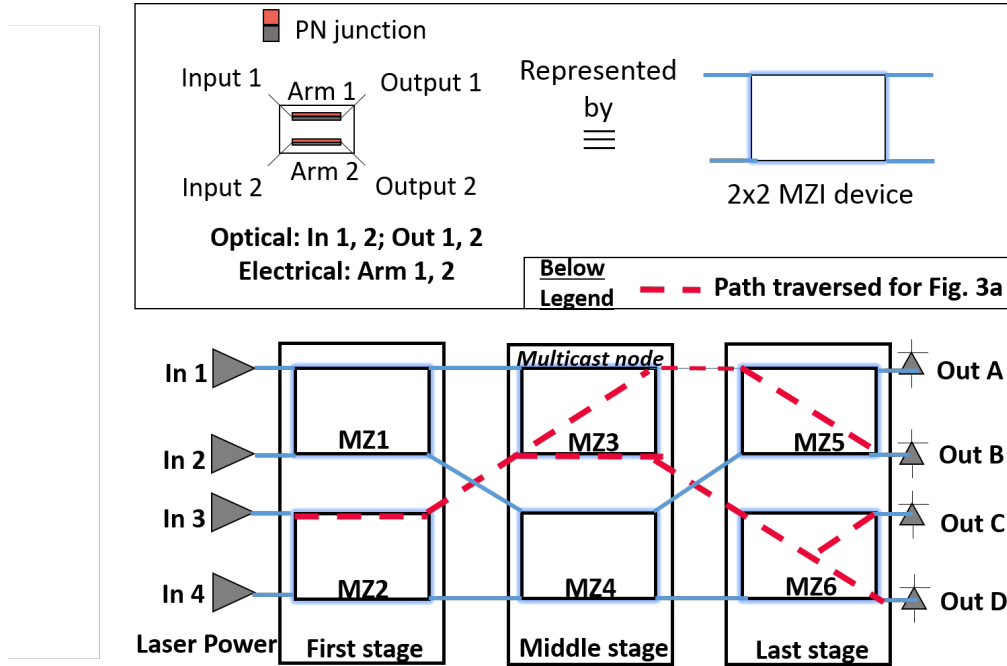


Figure 6.7: Cartoon of MZI switch element embedded in 4x4 topology where multicasting (pink, dotted line) is performed

tester (BERT).

Then, device characteristics of its switch rate are measured to be on the order of ~ 10 ns. The measurement was done by inputting a pulse stream with a digital timing generator (DTG) clocked at 10 Gb/s and looking at the output on a digital communication analyzer (DCA) of the same trigger. The noise is likely the result of crosstalk at the crossings of the switch fabric.

6.3.3 Algorithmic Implementation

The associated control algorithm is shown to provide the capability for dynamically reallocating optical power along a given path. The flowchart for the algorithm is shown in Fig. 6.9. It is implemented using C programming operating the data acquisition (DAQ) kit. Detailed description of the algorithm is included here.

From the initialization portion of the algorithm, bias voltage values on the M.N. are

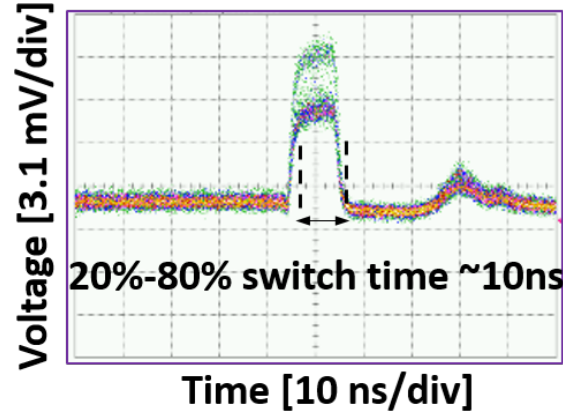


Figure 6.8: Switch latency

mapped to power values corresponding to the current configured switch fabric and saved in tables to refer to later. Power values of the two channels exiting the switch fabric and relative power level are constantly being monitored. When there has been a shift in power, relative power is used to update power values stored in the table.

The pseudo-code and implementation of tools provide a sense of experimental considerations.

The National Instruments (NI) DAQ is used for reading and writing voltage values on-chip. Task handles are used to continue cycling through data acquisition without running out of onboard memory. Standard deviation between same sets of voltage values and subsequent power reading acquisitions over time is on the order of 0.0001. The algorithm is presented in two main portions and implemented over a range of voltage values that result in relative power variation. Voltage values in the v_{sweep} array range from that needed to attain the high switch state to the low switch state, where the slope of the output optical power to voltage bias is noticeable. The switch device bias values ranged from 0.9 V to 1.5 V. The following is pseudo-code of the demonstrated algorithm.

Algorithm Part 1 System Power Initialization

Input: p_i and $p_{j \neq i}$ current power values of path i and j respectively

Persistent Values:

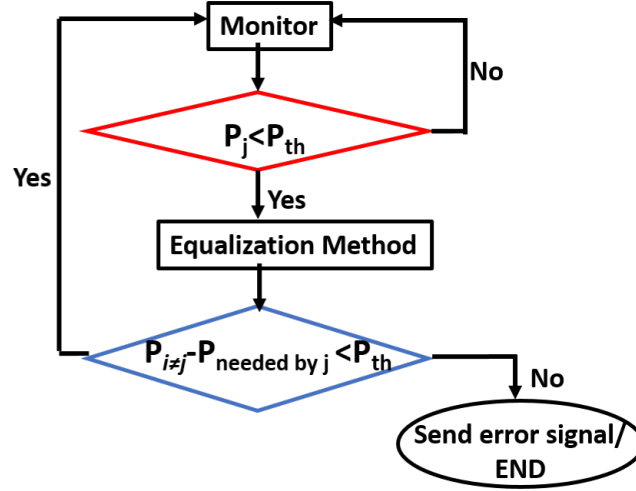


Figure 6.9: Flowchart implementing algorithm via control plane per the equalization method described in this section

- $S_{path}(p,v)$ a table of state for power, voltage pairs when initialized by the user. Equal sign designates setting a variable to a value.
- v_{sweep} : array of bias voltage values, the range of which are applied on node shared by path i and j

while *initialization state* **do**

for all operational v bias range, designated v_{sweep} **do**

$S_i(p = p_i, v = v_{sweep})$

$S_j(p = p_j, v = v_{sweep})$

end for

end while

Algorithm Part 2 System Power Equalization Check

Input: p_i and $p_{j \neq i}$ current power values of path i and j respectively

Output: v current bias value of node shared by path i and j

Persistent Values:

- $S_{path}(p,v)$ a table of state for power, voltage pairs as initialized by the user. Equal sign designates setting a variable to a value.
- Look up table (LUT) utility for accessing $S_{path}(p,v)$ for the power given the bias voltage value ($LUT(S_{path}(p, v = v_{bias}))$) or the voltage given the power value ($LUT(S_{path}(p = p_{value}, v))$). Accuracy of the latter lookup is determined by the selected acceptable deviation from desired power value.
- v_{sweep} : array of bias voltage values, the range of which are applied on node shared by path i and j . v_{bias} is value of v currently applied on the M.N.
- Threshold power level for photoreceiver, p_{th}
- To consider one specific case, we take p_j as the path that loses power

while *equalization state* **do**

if $p_j \neq LUT(S_j(p, v = v_{bias}))$ **then**

$p_{change} = LUT(S_j(p, v = v_{bias})) - p_j$

for *all operational v bias range, designated v_{sweep}* **do**

$p_{tmp} = LUT(S_j(p, v = v_{sweep}))$

$S_j(p = p_{tmp} + p_{change}, v = v_{sweep})$

end for

else continue

end if

if $p_i \neq LUT(S_i(p, v = v_{bias}))$ **then**

$p_{change} = LUT(S_i(p, v = v_{bias})) - p_i$

for *all operational v bias range, designated*

v_{sweep} **do**

$p_{tmp} = LUT(S_i(p, v = v_{sweep}))$

$S_i(p = p_{tmp} + p_{change}, v = v_{sweep})$

end for

else continue

```

end if

if  $p_j < p_{th}$  then
     $\Delta p = p_{th} - p_j$ 
    LUT(  $S_j(p \leq p_j + \Delta p + p_{dev}^* \ \& \ p \geq p_j + \Delta p, v)$  )
    returns  $v_{biasnew}$ 
    LUT(  $S_i(p, v = v_{biasnew})$  ) returns  $p_{new}$ 
    if  $p_{new} > p_{th}$  then
        set  $v = v_{biasnew}$ 
    else transmit error signal to deal with power loss in
    path
    end if
else continue
end if
end while

```

Note that $p_{dev} \ll \Delta p$. Upon first reading of the algorithm, you can assume $p_{dev} \rightarrow 0$. p_{dev} serves as a kind of buffer for the algorithm— an appropriately chosen p_{dev} for your specific system should not be too small in value to be constraining, nor too large in value to be inaccurate. Specifically, the p_{dev} value will depend on the granularity of your sweep steps as well as the tolerance of the system.

6.3.4 Demonstration of Dynamic Reconfiguration

The power monitor recognizes when the power level of one path falls below the threshold value, typically a nominal value referring to the receiver sensitivity level. This is when the equalization method is triggered, with the goal of having both paths attain the required performance metric.

The equalization method is applied to check the conditions for varying bias on the M.N. If the path with lower loss can tolerate reallocating the amount of power the path with higher loss needs to reach threshold, then the check passes. The new bias, set on the M.N.,

is determined from the table. Otherwise, the control system will be alerted to handle this power loss as necessary.

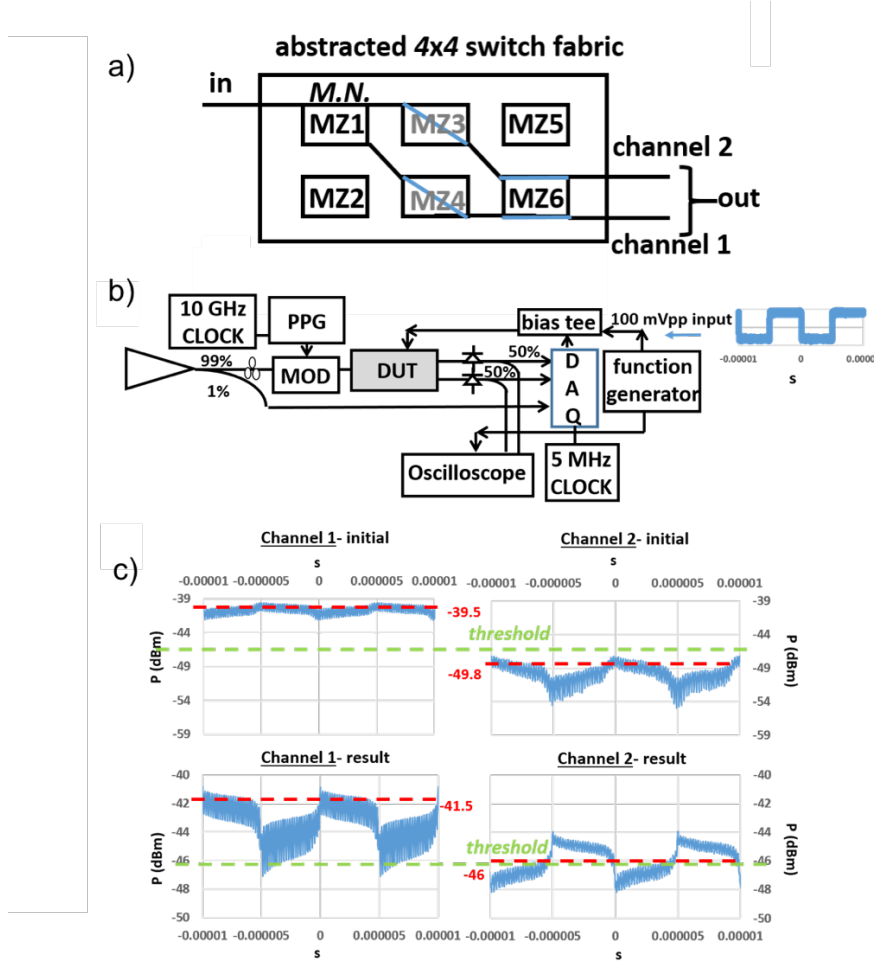


Figure 6.10: Experimental setup for dynamic demo; b) Channel 2 state initially falls below threshold. It recovers when Channel 1 provides it power in real time.

The switch configuration is set so that MZ3 and MZ4 are in the cross position. MZ6 is in the through state. Power becomes attenuated on Channel 2, triggering the equalization method, while Channel 1 stays above threshold level. The common M.N., MZ1, is biased in the switch fabric by the DAQ output. The top two graphs of Fig. 6.10c show the initial states, and the bottom 2 graphs show the final states of the channel.

Our implementation occurs on the timescale of the electronic componentry supporting

this dynamic operation. The cycle within the DAQ is clocked at a rate of 5 MHz. For the monitoring scheme, techniques with high resolution have been demonstrated at up to 40 GHz [Kim *et al.*, 2008b]. In a working data center, as we will further touch on in the next section, operation speed will instead be limited by network latency. Network latency can depend on data center size, the number of routers a signal traverses, with each router adding additional delay, and the algorithm deciding the network route [Stabile and Williams, 2014].

6.3.5 Simulation Results and Discussion

Computational simulations were performed to evaluate dynamic power reallocation in a system like the one illustrated in Fig. 6.11a. We examine two Gaussian white noise channels that each exhibit 40 dB of loss after the signal has traversed through the system. These channels share a common M.N., which is set in the switch fabric. The M.N. is initially set so that 50% of total power is allocated to Channel 1 and 50% of total power is allocated to Channel 2. Given this M.N. configuration, Channel 1 and Channel 2 will have 20 dBm power entering its respective channels when the total laser source power is set to 40 dBm. For our simulations, the laser source power indicated is the amount initially allotted to the individual channels.

The laser source power and photodetector sensitivity are set to specific values for the simulation to observe how different laser source powers and photodetector sensitivities can affect margin of power for probabilistic operation of the algorithm. Three different laser source powers (24 dBm, 22 dBm, and 20 dBm) are simulated over a range of photodetector sensitivities from -26 dBm to -17 dBm. For each simulation, the laser source power and photodetector sensitivity are the same for both simulated optical channels. For one simulation run, Channel 1 power at the receiver is initially received with no induced loss, indicating that with a 20 dBm laser source, and in a 40 dB-loss system, Channel 1 receiver will see a constant -20 dBm power level. Fig. 6.11a illustrates how Channel 2 power at the receiver end varies based on the added loss to its pathway. We observed in the simulation that added loss can vary up to 9 dB from the specified laser source power.

Since the loss is added to Channel 2 in the simulation through random generation and is upper bound by 9 dB, there are two possible outcomes of the dynamic power reallocation

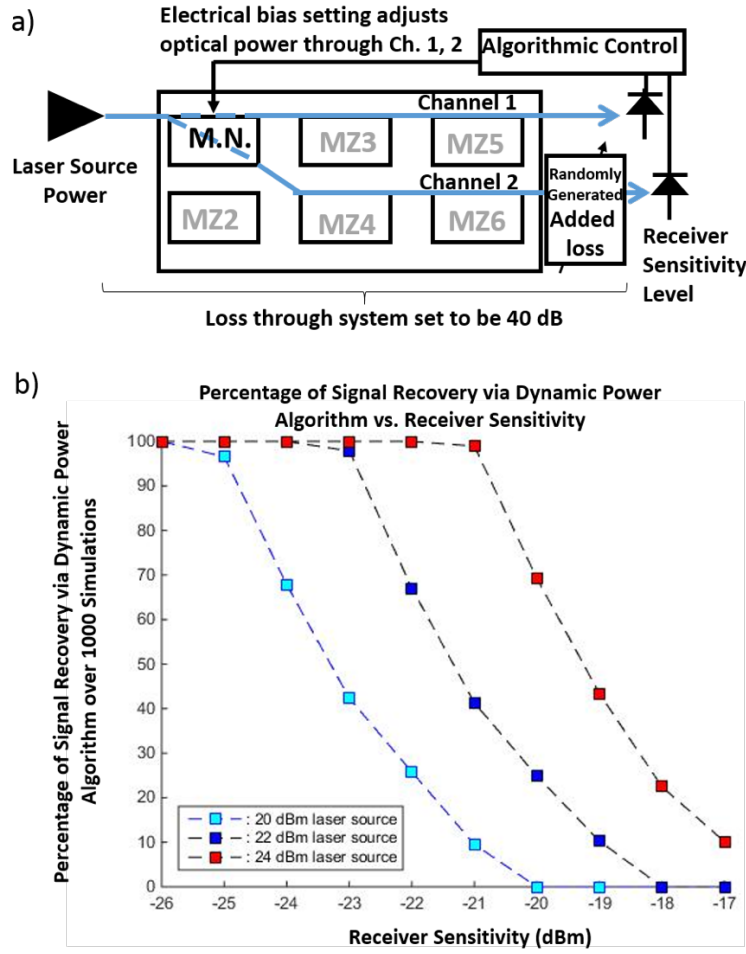


Figure 6.11: (a) Simulated setup with integrated switch fabric. (b) Simulation result of percentage of times signal is recovered vs. receiver sensitivity when dynamic power algorithm is employed. Each point in the graph is garnered from over 1000 simulations.

algorithm. As many simulations are run, we see what tends to occur when the parameter of power fluctuation is a random variable. We do not discuss the condition where Channel 2 power does not fall below threshold level. Loss added to Channel 2 causes Channel 2 power level to fall below the receiver threshold level. The decision tree depicted in Fig. 6.9 describes the following series of statements. This loss of power will trigger the dynamic power algorithm to check whether Channel 1 can provide the necessary amount of additional power for Channel 2 and still attain the receiver threshold level. If yes, Channel 1 will perform power reallocation, resulting in the recovery of Channel 2. If Channel 1 is not able

to provide the power differential for Channel 2 power at the receiver to reach the receiver threshold level, without itself falling below threshold, then this condition will result in an outage.

This simulation is performed 1000 times for each point on the graph, with the percentage of times signal recovery occurs calculated over the total number of simulations run, provided that the dynamic power algorithm is used. Specifically, the value being graphed is the number of recoveries over the sum of recoveries and outages. The simulation result is shown in Fig. 6.11b, where each point in a graph can be traced to the y-axis for its probabilistic value of signal recovery and to the x-axis for the corresponding receiver sensitivity. Three plots are graphed, one for each simulated laser source power.

The margin of successful power reallocation given that the dynamic power algorithm is run depends on laser source power and receiver sensitivity. The intersection point of each graph with the x-axis, which we will call the intersect point, is the difference between the laser source power and the set loss of the system, 40 dB. From our simulation results, we can see that the Channel 2 signal is recovered progressively along the direction of decreasing receiver sensitivity value until it reaches its maximum percentage of recoveries, within 5 dB of its intersect point. Likewise, the higher the laser source power, the larger this intersect point value as seen on the x-axis will be. This percentage of recovery is related to the power consumption that can be reduced with our dynamic power reallocation scheme in place.

6.4 High-Performance Computing through Silicon Photonics

6.4.1 Background

For the HPC testbed, we show the advantages of using a silicon photonic device, specifically the one described in the above sections, for switching [Wen *et al.*, 2016a]. Previous demonstrations of switching have primarily utilized MEMS-based switching.

The Dragonfly network is employed [Wen *et al.*, 2016b], a topology where the traffic is divided into two levels [Kim *et al.*, 2008a]. One level, the lower level, connects local networks, termed groups. The other level, called the upper level, connects groups through an all-to-all topology. This kind of topology is favored over multi-dimensional torus or fat

tree because it is able to provide full connectivity over the entire network [Dally and Towles, 2004]. This full connectivity is performed through adaptive routing that allows the traffic to go where the traffic is less distributed [Ebrahimi, 2013]. However, even with these dynamics in mind, traffic sometimes finds itself with increasing amount of latency to the destination and higher congestion.

With the optical switch placed strategically to link groups in both an intra- and inter-group manner (Fig. 6.12), the Dragonfly topology is able to be dynamically reconfigured. This demonstration on the switch platform described in the above section exhibits a 2x throughput improvement when flexible Dragonfly, named Flexfly, is employed relative to Dragonfly topology.

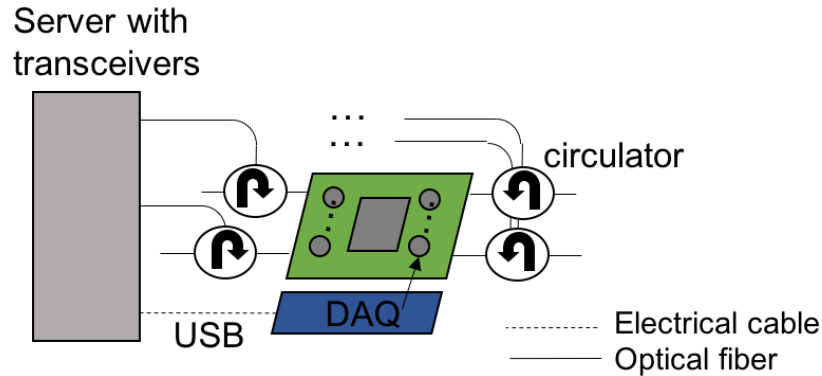


Figure 6.12: Cartoon of the switch interconnected with the server racks. The optical paths are bidirectional, with the addition of circulators.

6.4.2 Demonstration

Network traffic is redirected through the Si photonic device with the switch being biased to either a bar state or a cross state. Dynamic extinction ratios are maximally 15 dB and minimally 7 dB in the bar state while in the cross state it ranges from 19 to 24 dB. A higher speed DAQ than the one previously employed generates the voltages applied to the device. A C program controls the DAQ and is directly callable by the controller server.

From the 2x2 switch level up, the pathways are connected to 4 groups. Fig. 6.13 shows the HPC connection.

The controller server sends reconfiguration commands to the DAQ for switching between the bar and cross states and to the routers for updating the flow table rules. Flow table rules indicate to the signal passing through the router which path hop to take next for the signal to reach its destination. These also include statements that the router follows in order to forward, drop, or rewrite groups of packets for the purposes of switch testing and development [Salisbury,].

The timing for the switch is shown in Fig. 6.14. 820 ns switch time is achievable with a Msample/s analog output. The link reconfiguration time includes the transceiver's lock time (100 milliseconds for commercial small form-factor pluggable (SFP+)).

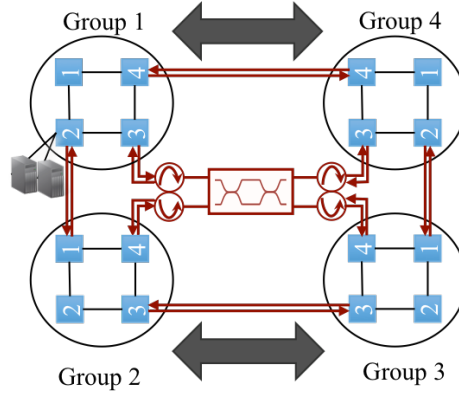


Figure 6.13: Experimental setup of Flexfly topology

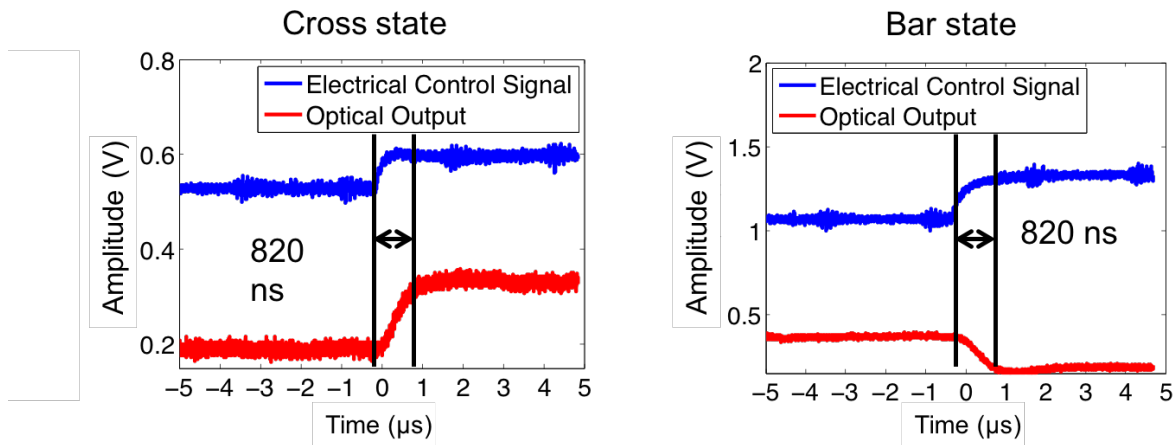


Figure 6.14: Switch latency indicating setup time

In computing, benchmarks are standardized tests run to see how long a system takes to set up. The Hpcbench Message Passing Interface (MPI) benchmark [Borrill *et al.*, 2007], one such standard, was run across the configuration shown in the below figure. The round trip delay between 8 pairs of servers located in two groups was measured. For the traffic pattern, each server in the first group (G1) communicated with a corresponding server in the fourth group (G4). In the cross state, which corresponds to the original Dragonfly topology, there is one global link between the two groups. Setting the switch in the bar state grants an additional link to this G1-G4 group pair.

In traffic flows between routers 3 and 4 of G1 and G4 and flows between routers 3 and 4 of the second group (G2) and the third group (G3), throughput showed a 2x increase for Flexfly over Dragonfly. In the physical implementation, this improvement means that throughput increased by two times for the bar state over the cross state configuration. The extra hops that data flows take in the Dragonfly configuration increases the round-trip time, potentially affecting flow control and lowering bandwidth. Meanwhile, Flexfly routes all flows over minimal hops leading to fairer bandwidth access for all groups.

Dynamically reconfiguring the system is depicted in Fig. 6.15. The servers are set up with flow rules that reroute the path for a Flexfly topology.

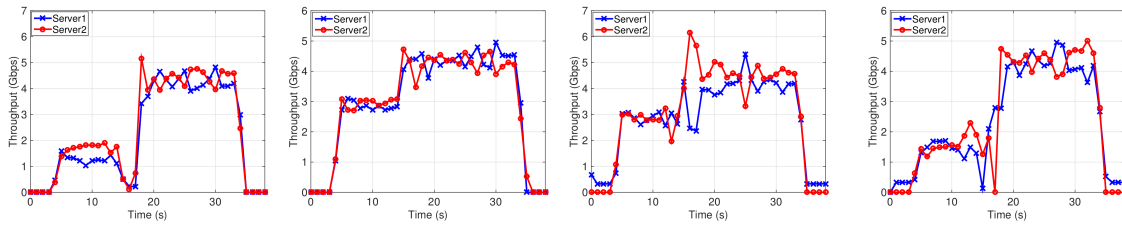


Figure 6.15: Dynamically reconfiguring the system done at second 15 of the exhibited graphs, with one extra global link provided between the two groups

Throughput is higher in the Flexfly-adapted configuration (bar state) as two global links are awarded to each of the above group pairs, marking the first time real performance improvements have been shown with a small-radix optical switch, specifically for reconfigurations needed by a single application.

6.5 Main Takeaways

In a high-performance computing environment, a large amount of effort has gone into designing systems with the capability to dynamically move data [Lin *et al.*, 2016]. In this work, we show not only a wholly novel way of dynamically reallocating power, with data multicast on top, but also the utility of Si Ph switch chips in an HPC environment. A dynamically programmable interface is designed to set the switch fabric and control the switch element biasing scheme to distribute power as desired to its final outputs. The unique power algorithm is shown to dynamically recover an optical channel across an error-free 4x4 switch fabric propagating 40 Gb/s data. Furthermore, application-level data is shown to be effectively switched, and throughput doubled, across the same Si Ph platform, when compared to a static Dragonfly topology across groups of servers.

Chapter 7

Optical Components for Future Applications

The design and application of integrated components are described in this chapter. A path towards sustaining data growth is to accommodate for new spectral regions at wavelengths around $2\ \mu\text{m}$ [Ackert et al., 2015]. Since Si and III-V materials only absorb up to $1.1\ \mu\text{m}$ wavelength [Nabet, 2015], photodetection beyond this wavelength regime has primarily been done with the use of InGaAs and Ge PD materials. Recently, it has been found that by introducing sub-bandgap defects, detection at longer-wavelengths is possible via the Si medium. Experimental demonstration of photodetection at $1.9\ \mu\text{m}$ is shown in this chapter with Si^+ -doped Si photodetectors at 1 Gb/s data operation featuring responsivities of $0.03\ \text{AW}^{-1}$ at 5 V bias.

Beyond direct detection, balanced detection will enhance sensitivities of recovered signals. Differential detection enhancing stability, enabled through a unique perfect coherence mechanism, is explored here. Specifically, a coherent perfect absorption Si modulator is demonstrated, showing an extinction ratio of 24 dB. Coherent perfect absorption is demonstrated in a Si chip for the first time.

7.1 Moving into the Long Wavelength Regime

In extending the wavelength regime, we can look at Fig. 7.1 to see available materials and processing steps to enable photodetection at longer wavelengths [Souhan *et al.*, 2013].

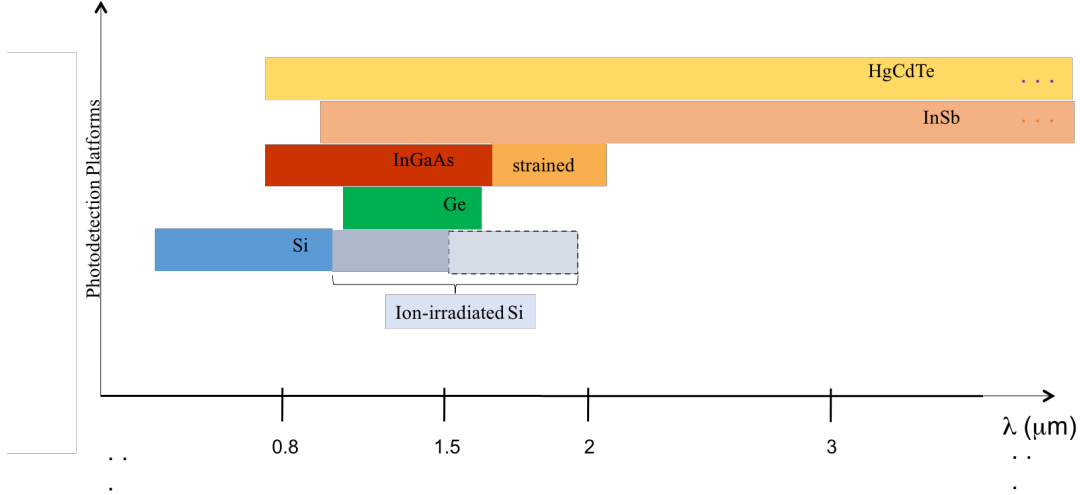


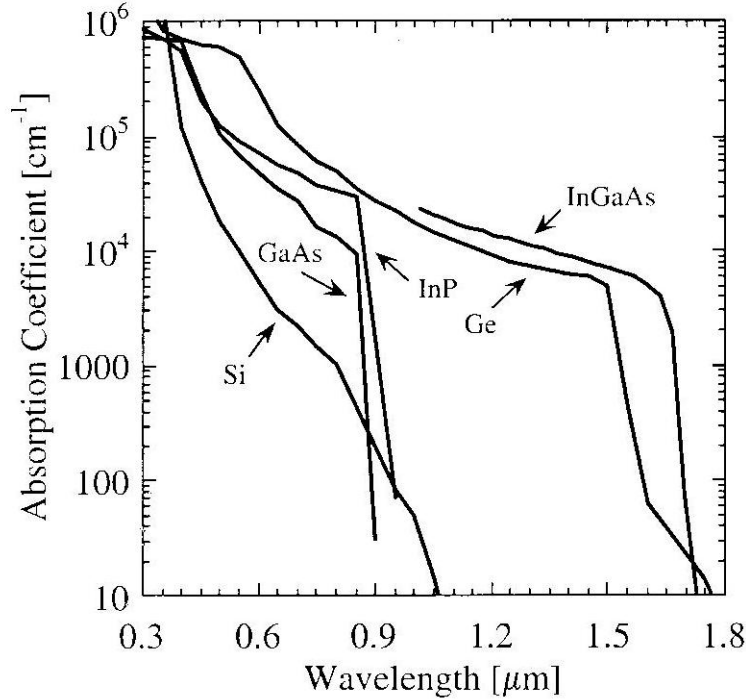
Figure 7.1: Collection of mid-IR materials technology, where Si is referenced from [Geis, 2009][Grote, 2013]

7.1.1 Applications of Long-Wavelength Detection

Light Detection and Ranging (Lidar) applications are commonly used in military surveillance and satellite monitoring of landmarks or weather from the sky [Young and Vaughan, 2009]. This is because long wavelength is better able to penetrate through obscuring structures or forms. Long wavelength detectors are needed for remote sensing through sub-optimal atmosphere conditions. Besides these functionalities, photodiodes sensing at longer wavelengths can push the operational spectrum to include mid-IR for the possibility of larger aggregate bandwidth support.

Long-wavelength detection provides the distinct advantage of larger bandwidth support for WDM. However, current state of the art does not support beyond the U-band (1625 nm -1675 nm). Thulium doped fiber amplifiers (TDFA) operating in this wavelength regime do exist and are being further developed [Li *et al.*, 2013]. Fibers that can support these

wavelengths are also being introduced into the market. Therefore, it is not unlikely that commercial equipment will trend towards supporting this bandwidth regime.



Handbook of Optical Constants of Solids, edited by Edward D. Palik, (1985), Academic Press NY.

Figure 7.2: Absorption Coefficient of Common Materials over Wavelength Range [Palik, 1985]

7.1.2 Background

Si⁺ ion implanted waveguide photodetectors are investigated in the following section. These photodetectors were fabricated at MIT Lincoln Labs by Geis and Spector. At 1.55 μm, Si photodetectors were found to have comparable IQE (0.8 A/W at 5 V) and absorption coefficients (20 dB/cm) as compared to Ge detectors [Grote *et al.*, 2013b], utilizing the Si interstitial cluster defect for operation. The process of ion implantation goes beyond substitutional doping, which is largely used in semiconductor processing. Instead, different defects occur here as a direct result of the annealing temperature and implanted ions.

Following Fan and Ramdas' seminal work on deuteron-irradiated Si [Fan and Ramdas,

1959], where they detected to $1.8 \mu\text{m}$, we utilize the Si-divacancy defect caused by dislocation of lattice atoms. Post processing temperatures reach 350°C maximally. The work presented here is the resulting detector that pushes the detection regime to $1.9 \mu\text{m}$.

7.1.3 Photodetector Design and Experimental Setup

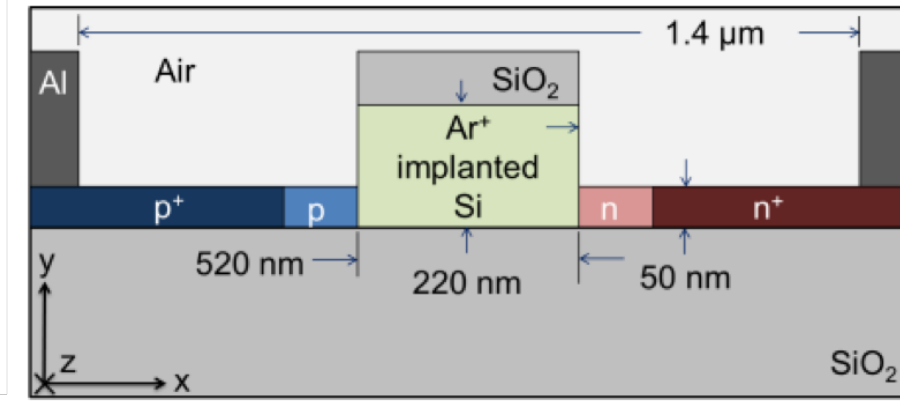


Figure 7.3: The center of the structure is intrinsic, and there are p and n doped regions on either side, forming a lateral p-i-n diode. Damage from the ion implantation makes the intrinsic region sensitive to light, which when present in the waveguide causes carrier generation.

The PD devices designed are 2 mm in length, 220 nm tall, and 520 nm wide, as shown in Fig. 7.3. The rib waveguide structure is ion implanted with $10^{13} \text{ cm}^{-2} \text{ Si}^+$ ions. Sub-bandgap defect states formed via Si^+ ion implantation are exploited. The structure is then annealed to 350°C .

The 2-mm device was measured to have a 3 dB bandwidth at 1 GHz, limiting our data rate, while the 3 dB bandwidth for the 3-mm device was 0.995 GHz. Higher data rates can be achieved by increasing the frequency response through better contact pad design and the use of shorter devices. For receivers often used in telecommunication systems, the sensitivity metric indicates its suitability for the telecommunications system. The receiver sensitivity is the minimum optical energy required to attain a specific bit error rate of 10^{-9} , which is estimated to be 12.4 dBm for the two device lengths of 2 mm and 3 mm examined.

For this particular measurement, 25 V reverse bias was necessary to push the current gain high enough to drive the limiting amplifier. It is possible that the photoreceiver was then operating in the avalanche regime.

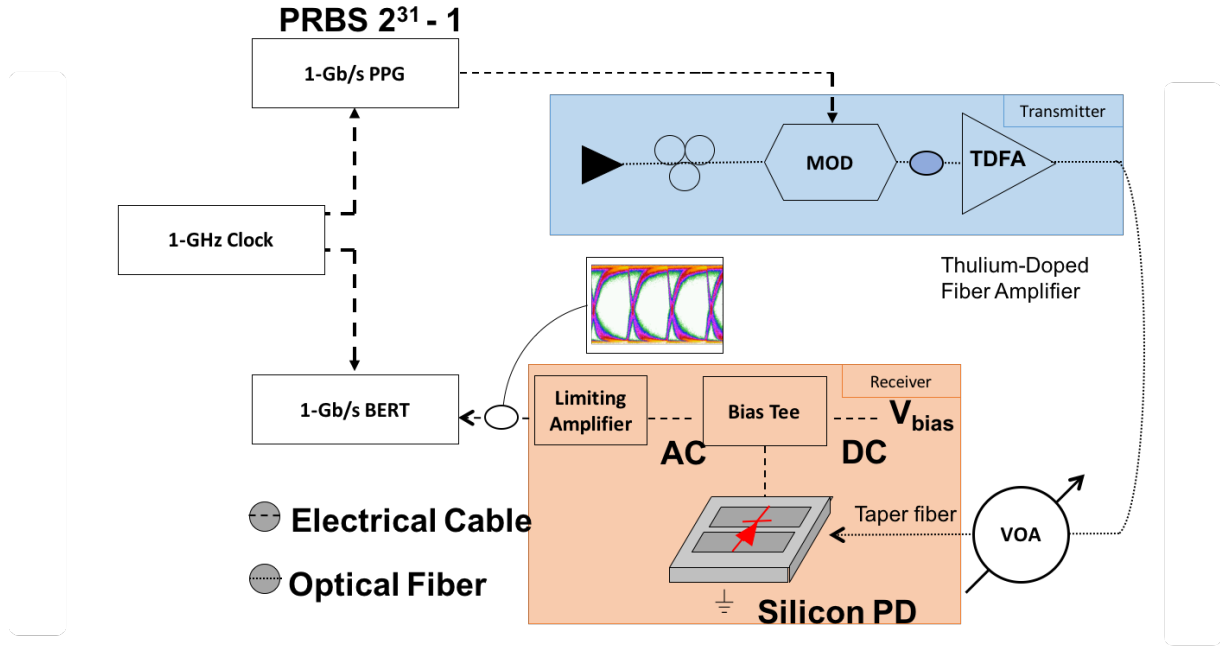


Figure 7.4: PD device embedded in the high-speed system

The experimental setup is shown in Fig. 7.4. After measuring the bandwidth, the pulse pattern generator (PPG) and bit error rate tester (BERT) were clocked at a suitable rate. Using those equipment, we modulate $2^{31}-1$ non-return-to-zero (NRZ) pseudo-random bits sequence (PRBS) onto the light path through the LiNbO_3 modulator. The laser is tuned, and the signal is amplified before it is launched on-chip. On the electrical componentry side, we bias the PN junction to increase the photocurrent. The resulting signal is captured with the limiting amplifier to go to the BERT to take further measurements. These resulting BER measurements are shown in Fig. 7.5a.

7.1.4 Experimental Results

The probability that a single photon landing on the detection region will induce a carrier that contributes to photocurrent is the quantum efficiency (QE) measurement. When a

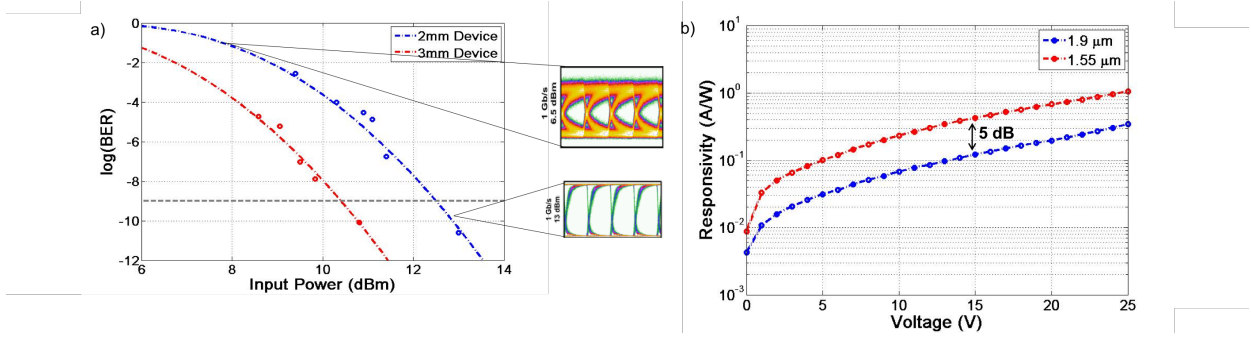


Figure 7.5: a) BER measurement for 2 mm (with the corresponding eye diagram) and 3 mm PDs operating at 25 V bias and 1 Gb/s and 0.975 Gb/s respectively; b) Device Responsivity for 2 mm PD at 1.55 μm and 1.9 μm wavelength, with dark current two orders of magnitude lower in current

device is bombarded by many photons, QE indicates the flux of electron-hole pairs to the flux of photons. Beyond telling us how many carriers are generated, QE also illuminates the effectiveness of the conversion rate of photons to carriers.

We measure these devices to have QEs of 0.2 AW^{-1} at 5 V, exhibiting the absorption characteristic, as stated, due to interstitial clusters or divacancies effects. Fig. 7.5b plots the responsivity, which is the electric current with respect to the optical power being placed on it. It is equal to $\text{QE} \cdot e/h$, with units of A/W, where e is the photocarrier pair and h is Planck's constant. It can also be written as a function of incident wavelength and material.

At 1.9 μm , the measured responsivity is 0.03 AW^{-1} at 5V bias, approximately 5 dB less than the responsivity at 1.55 μm . Performance can be improved to less than 2.5 dB difference by optimizing waveguide dimensions specifically for long wavelength operation.

It should be noted that the tapered fiber and coupler of light on-chip were designed for 1.55 μm . Due to this mismatch, an added 3 dB of loss could be present.

7.1.5 Improving Long Wavelength Photodetection and Extending Long Wavelength Detection Range

Some difficulties related to Si supporting long wavelengths include the difference in modal confinement factor for longer wavelength compared to C-band support. The power confinement factor is the power in the slab divided by the total power. This value is dependent

on the slab width as well as the wavelength of operation. Silicon waveguides have a smaller modal confinement factor for longer-wavelength than shorter wavelength light, leading to reduced absorption in implanted silicon.

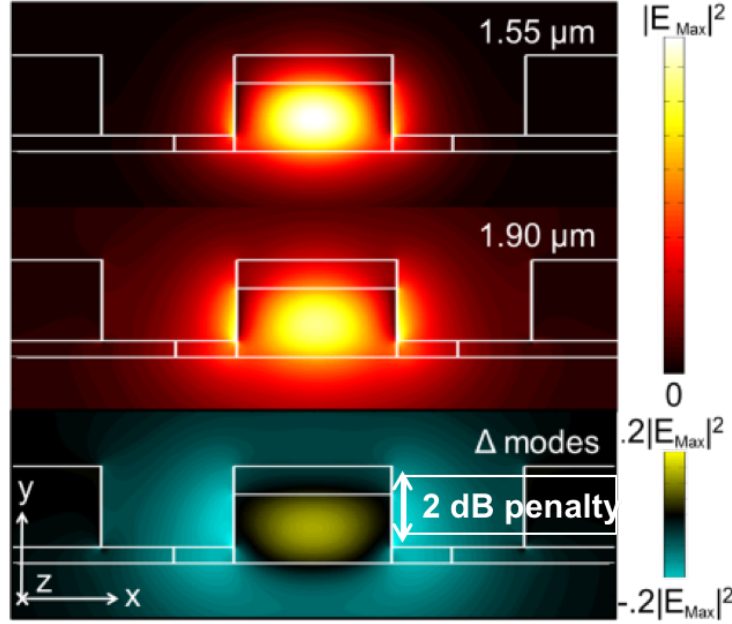


Figure 7.6: Modal confinement of different wavelength light through Si ribbed waveguides

In order to visualize the modal confinement of longer wavelengths in Si rib waveguides, simulations were performed using the Finite Element Method (FEM). It can be seen that the difference in modal confinement for $1.55 \mu\text{m}$ vs. $1.9 \mu\text{m}$ results in about a 2 dB power penalty.

In a follow-up to this work [Souhan *et al.*, 2016], the photodiode was annealed with the Ar^+ implantation energy chosen to put both the peak of the defect density and Ar ions in the waveguide for $2.2 \mu\text{m}$ operation. Since the vacancies are very mobile at anneal temperatures from 150°C to 350°C , a fairly even post-anneal distribution of defect and Ar ions throughout the channel section of the waveguide formed after heating. Responsivity improved to 21 mA/W from the Si^+ -implanted photodiode [Souhan *et al.*, 2014]. The demand for operation in this regime will become more apparent as chemical and biological sensing applications, some using two photon absorption processes, are realized.

7.2 Coherent Reception: Performance Improvement

Coherent perfect absorption (CPA) is a recently discovered phenomenon whereby a combination of superposition and critical coupling allows for phase controllable modulation of absorption in a resonant cavity [Chong *et al.*, 2010]. Utilizing this effect, the on-resonance absorption can be tuned between 0% and 100% of the input power by modulating the phase difference between two inputs to the resonator. Since CPA is based on critical-coupling [Haus, 1984] [Yariv, 2002], perfect absorption can be achieved for any material absorption coefficient by appropriately designing the input coupling coefficients.

CPA has been proposed for a number of on-chip applications, including a method of all-optical switching [Mock, 2012] that reduces the need for non-linear effects to modulate the round trip phase [Gardes *et al.*, 2005] or absorption [Wen *et al.*, 2012], as well as a novel architecture for differential phase shift keying (DPSK) demodulation.

Phase controllable amplitude modulation through a material's coupling is shown for the first time in silicon [Rothenberg *et al.*, 2016]. This mechanism uncouples the relationship of efficiency of the absorption effect from the Q -factor of the resonator.

7.2.1 Main Terms

Optical coherence is the study of statistically in-phase light. The wave function is dependent on time and position in a periodic fashion. Coupling of waves to a waveguide can be depicted as [Saleh and Teich, 1991]:

$$\begin{pmatrix} b_1 \\ b_2 \end{pmatrix} = \begin{pmatrix} t & k \\ k^* & -t^* \end{pmatrix} \begin{pmatrix} a_1 \\ a_2 \end{pmatrix}$$

$$|t|^2 + |k|^2 = 1$$

For a ring resonator, this can be represented as $a_2 = b_2 \alpha e^{i\theta}$, where α =loss (or gain) and θ = phase shift per circulation. The transmission factor in the input waveguide is then written as:

$$\frac{b_1}{a_1} = \frac{\alpha^2 + |t|^2 - 2\alpha|t|\cos\theta}{1 + \alpha^2|t|^2 - 2\alpha|t|\cos\theta} \quad (7.1)$$

If $|a_1|^2$ incident power is taken to be one, then we are left with:

$$|b_1|^2 = \frac{(\alpha - |t|)^2}{(1 - \alpha|t|)^2} \quad (7.2)$$

at resonance $\theta = m2\pi$ where $m \in \mathbb{Z}^+$. When $|b_1|^2 = 0$, then $\alpha = t$ and critical coupling has been achieved.

This α is what we seek to control then, with respect to t . For a MZI, if the two arms have a differential phase, $\Delta\phi = V^*\pi/V_\pi$ where V_π is the voltage shift causing $\Delta\phi = \pi$,

$$\frac{P_{out}}{P_{in}} = \frac{(\alpha - \cos(\pi * V/2V_\pi))^2}{(1 - (\pi * V/2V_\pi)^2)} \quad (7.3)$$

Critical coupling is often achieved by controlling $\Delta\phi$ but it can also be done by controlling the internal loss parameter α .

Examples of adjusting coupling via the term has been explored as early as in [Yariv, 2002], but it has not yet been shown in a silicon photonic device.

7.2.2 Device Theory

In CPA, a resonator couples steady-state power from an external source at a rate denoted by γ_c . Intrinsic loss in the device, represented by γ_i , can be due to absorption or scattering loss. When $\gamma_c = \gamma_i$, critical coupling occurs. This means that 0% of input power is lost relative to the normal case when 100% of input power is lost [Chong *et al.*, 2010].

For CPA to occur, the resonator needs to have two input ports. Interference occurs much like the principle of the MZI. The power can be represented in equation similarly. The equation of $P_{output1,2}$ is derived to be

$$P_{output\ 1,2} = \frac{P_{tot}}{2} \left(\frac{\gamma_c^2 + \frac{\gamma_i^2}{4} - \gamma_c\gamma_i \cos(\Delta\phi) + \Delta\omega^2 \pm 2\gamma_c\Delta\omega \sin(\Delta\phi)}{\Delta\omega^2 + \frac{1}{4}\gamma_{tot}^2} \right) \quad (7.4)$$

where γ_{tot} denotes the total loss rate of the cavity, $\Delta\omega = \omega - \omega_0$, ω is angular frequency, and ω_0 is the resonant angular frequency [Grote *et al.*, 2013a].

When $\Delta\phi = 0$, a notch filter exists. When $\Delta\phi = \pi$, an all-pass filter occurs. On resonance ($\Delta\omega = 0$), the transmitted power out of each arm simplifies to [Chong *et al.*, 2010]:

$$P_{\text{output } 1,2} = \frac{P_{\text{tot}}}{2} \sin^2 \left(\frac{\Delta\phi}{2} \right). \quad (7.5)$$

7.2.3 CPA Modulator Device Description

The ring resonator, fabricated at Singapore Institute of Microelectronics, is composed of a 220 nm Si layer with a 2 μm buried SiO₂ layer (Fig. 7.7). The waveguide is a rib/ridge structure, and there are 2 curved regions of the resonator racetrack where Si⁺ has been implanted. The intrinsic loss is determined by the material absorption of 100 to 250 dB/cm through the creation of divacancy lattice defects [Pinnow *et al.*, 1973].

The coupling coefficient κ is controlled by γ_c , which is a function of edge-to-edge waveguide distance d [Chin and Ho, 1998]. A coupling gap of 320 nm is chosen to match the loss rate of Si⁺-implanted Si.

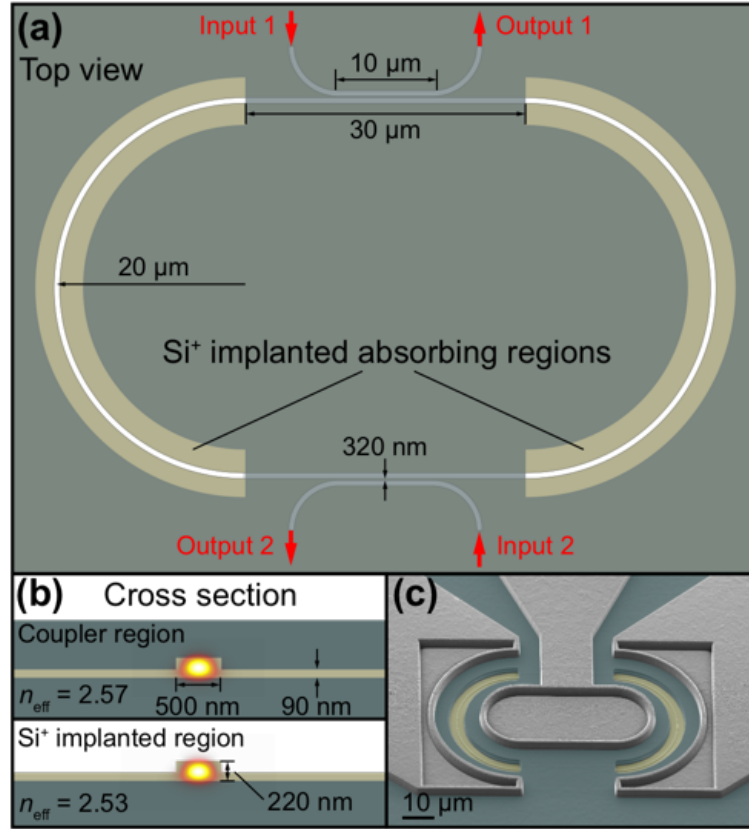


Figure 7.7: a) Device schematic; b) Waveguide cross section with oxide clad coupler region and air clad Si⁺-implanted region; c) Top-down SEM image

7.2.4 On-Chip CPA Demonstration

CPA operation is shown by having an off-chip phase modulator to adjust the phase of the tunable delay line [Rothenberg *et al.*, 2015]. Initially, calibration is performed to equalize the path lengths of the arms leading into the phase modulator and the other arm. This is done by adjusting the variable delay line (VDL) length in the other arm. Then, the following two experiments are performed.

First, the tunable laser source (TLS) syncs with the optical spectrum analyzer (OSA) (Fig. 7.8a). The sweep is set to 250 ms/sweep. This allows for little temperature dependent phase noise to arise in the measurement. The output to the device is put into the OSA. Relative phase is set to 0 through biasing the phase modulator, and the resulting spectrum is taken.

Due to the polarization sensitivity of the device, after the signal is launched on-chip, and the polarization is adjusted with a polarization controller to maximize the resonant dips, we no longer adjust the polarization prior to the chip. The power is also equalized leading into the chip.

Modulation depth of the device was captured, and this value is matched with the extinction ratio taken from the first measurement (Fig. 7.8b). This extinction result is discussed theoretically in a later section. The output of the CPA modulator is injected into a PD that is read into a DAQ interface. Sampling is controlled via a LabVIEW program. The function generator that is placed on the phase modulator is set to a 1 kHz, 9.8 V_{pp} ramp function.

The resulting diagram of (Fig. 7.9a) is measured, and the grayed area of the graph represents eleven consecutive wavelength sweeps. The wiggling characteristic seen is due to the Fabry-Perot etalon generated by the input and output coupling facets.

Meanwhile, Fig. 7.9b illustrates the phase dependent transmission through the racetrack resonator. The dots indicate the collected data, and the line is the best fit according to least-squares.

The extinction ratio (E.R.) is derived from $P_{output1,2}$. It can be represented completely by the loss ratio. The difference between $\Delta\phi=0$ and 4π is the extinction ratio, which comes to about 24.5 dB. This figure denotes perfect absorption.

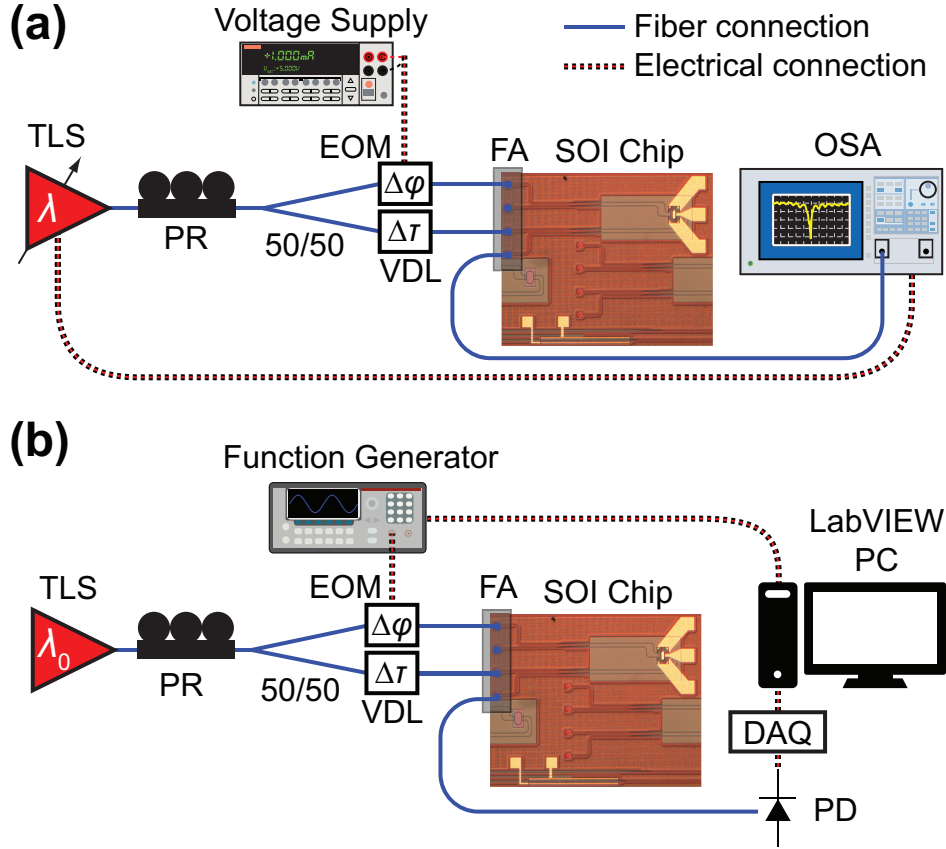


Figure 7.8: a) Experimental setup for spectral response; b) Experimental setup for phase measurement

7.2.5 Discussion on Sampling

The sampling rate is set in the LabVIEW program. The Peripheral Component Interconnect Express (PCIExpress) allows us to sample on demand, triggered at 1 kHz. This sample rate is matched with the choice of the ramp speed. Since we set the ramp to occur at 1 kHz, this sets the samples at 1000 samples/second or 1 sample/1 ms equivalently. The ramp allows us to sweep through steadily increasing voltage values till we reach V_π . The timing on the DAQ determines how quickly data flows from the device to the hardware. How quickly the data goes from the PC buffer into software processing is determined by the memory capacity of the computer [daq,].

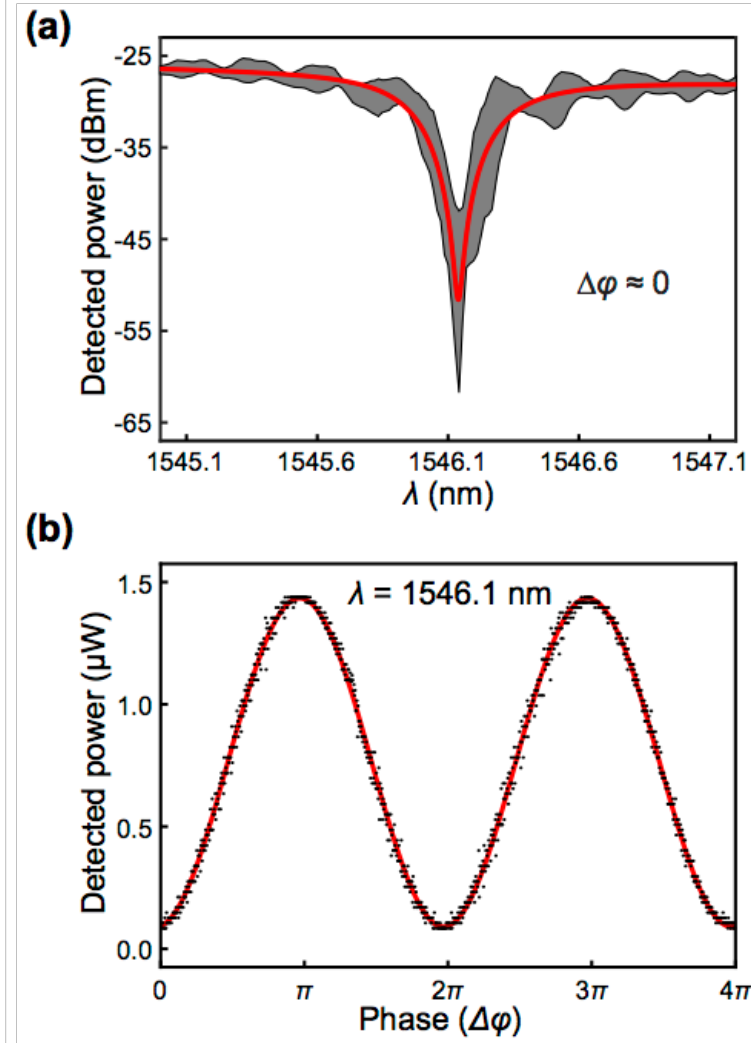


Figure 7.9: a) Power transmission vs. wavelength with $\Delta\phi=0$; b) Power transmission vs. phase shift at the resonant wavelength

7.2.6 Device Measurements

From the device measurements, the curves are least squares fit to $P_{\text{output}1,2}$ with the Fabry-Perot effect normalized out. As a result, the parameters are found to be $\gamma_i/(2\pi) = 29.4 \pm 0.5$ GHz, $\gamma_c/(2\pi) = 16.6 \pm 0.3$ GHz, and $\lambda_0 = 1546.12$ nm. For acquiring the transmission versus wavelength of $\Delta\phi = \pi$, the fit parameters are also used.

Accordingly, the Q -factor of the resonator at $\Delta\phi = 0$ was found to be $> 3,000$, where

$Q = \frac{\omega_0}{\gamma_{\text{tot}}}$. An absorption coefficient of $\alpha = 150$ dB/cm for the absorbing state ($\Delta\phi = 0$) was found using a modal group velocity of $v_g = c/3.8$, as determined by FEM modeling. The measured value of α matches previously measured modal absorption coefficient values for unannealed ion-implanted silicon waveguides [Souhan *et al.*, 2014]. A range of Q -factors can be designed for just by adjusting the ratio of R/L_{tot} to set γ_i , and modifying the coupler region such that $\gamma_c = \gamma_i/2$.

The extinction ratio of the device is calculated by finding the difference between on-resonance power with $\Delta\phi = 0$ and $\Delta\phi = \pi$ using the above fit parameters. An expression for the extinction ratio in terms of loss rates can be derived from the $P_{\text{output}1,2}$ equation:

$$\text{ER} = \frac{P_{\text{output } 1,2}^{\text{OFF}}}{P_{\text{output } 1,2}^{\text{ON}}} = 1 - \frac{8\gamma_i\gamma_c}{\gamma_{\text{tot}}^2} \quad (7.6)$$

which results in an extinction ratio of 24.5 using the fitted values of γ_c and γ_i .

Improvements that can be made to the device include fine tuning the coupling coefficient to the point where the loss rates get closer to critical coupling. From the fitted data, $\gamma_i = 1.8\gamma_c$, which indicates that the ring resonator is slightly over-coupled, resulting in a lower extinction ratio. While the device's coupling rate can be controlled by varying the gap distance between the input waveguides and the resonator, the internal loss rate is set by Si^+ -implantation, which is subject to fabrication process variation. Achieving perfect extinction requires the two input modes to be identical. This means that input power, mode profile, and polarization of the two inputs should be matched perfectly. Due to off-chip phase modulation, it became necessary to separate the two inputs off-chip. With these two separate light paths, all three of the parameters mentioned could be varied independently. On-chip phase modulation, which is being pursued, will be helpful to reducing signal phase noise, with phase modulation done through free-carrier effect [Reed *et al.*, 2010] or thermo-optic effect.

7.2.7 Benefits of System

The benefits of balanced detection are two-fold. First, a balanced detection scheme will reduce relative intensity noise (RIN). These are the random fluctuations in laser intensity.

$$i_{RIN}^2 = RIN * I_D^2 \quad (7.7)$$

where I_D^2 is dark noise of the photodiode and Δf is the circuit's limiting bandwidth [Joshi *et al.*, 2005]. This leads to improvement in the signal-to-noise-ratio (SNR).

Second, balanced detection will improve the third order spurious free dynamic range (SFDR3) measurement. This is defined to be the difference between the output noise level (N_{out}) and output power point ($P_{outSFDR3}$).

Data sent as differential phase shift keying (DPSK) enhances the signal by using balanced detection (Fig. 7.10). DPSK is a means of converting the phase into the 1 or the 0 bit. Below is a diagram depicting the functionality of DPSK reception.

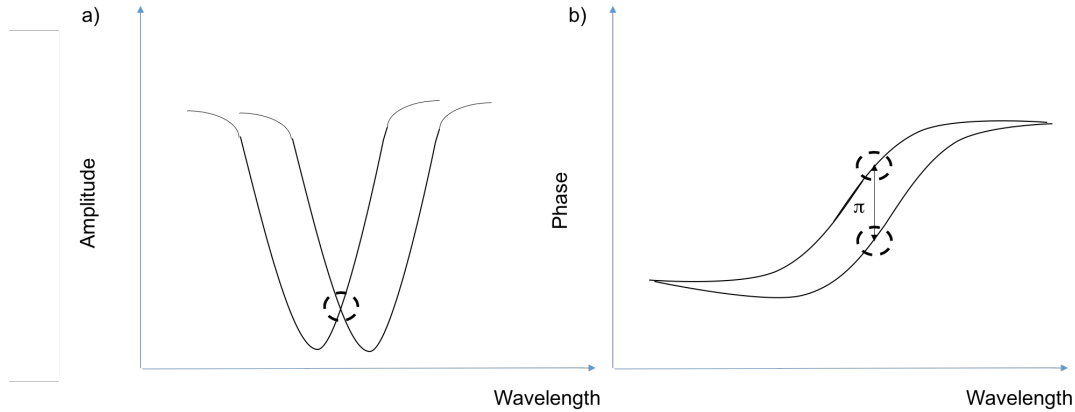


Figure 7.10: DPSK block diagram with a) showing the same amplitude of two signals b) but the difference in phase, which is what DPSK leverages

DPSK demodulation is usually done via a delay-line interferometer (DLI) [Christen *et al.*, 2009] or a microring modulator [Xu *et al.*, 2011]. The DLI is constructed for a specific bit rate; for 40 Gb/s, one path delays the signal by 25 ps. Then, the signals are recovered at balanced photodetectors simultaneously. If the signals recovered at the 2 PDs are out of phase, then an edge is detected (by a change in recovered amplitude).

DPSK data transmission has been proposed for WDM passive optical network (PON).

With lower insertion loss comes lower powers compared to OOK [Garg and Janyani, 2015].

Lastly, since CPA is based on critical coupling, perfect absorption can be achieved for any material absorption coefficient by appropriately designing the input coupling coefficients, meaning that the efficiency of this effect is independent of resonator Q-factor, with the idea similarly explored in [Saeedi *et al.*, 2015].

7.3 Main Takeaways

Novel device exploration for the purpose of expanding detection regime in the case of the Si photodetector is described in this section. Si ribbed waveguides can be processed in the same way to garner longer wavelength operation at 2.2 μm wavelength. Increasing demodulation stability in the case of the CPA modulator is also described in this section. By employing an automated process for data collection, instabilities in the fibers were minimized, with future implementations embedding an on-chip phase modulator for greater signal stability. These waveguide structures explore the possibility of enhancing spectral domain and stability through on-chip device integration.

Part III

Conclusions

Chapter 8

Conclusions

8.1 Overview

The work in this dissertation comprises a set of experiments designed to maximize bandwidth on-chip via mode-division multiplexing. Using available orthogonal domains by design of the multimode waveguide structure and mode multiplexing/demultiplexing region opens new avenues of attaining higher aggregate data channels. Whether through polarization-division multiplexing and mode-division multiplexing – a wholly novel combination demonstrated in this work – or through wavelength-division multiplexing and mode-division multiplexing, aggregate bandwidth is sufficiently scaled by leveraging different available physical domains for increasing bandwidth. In the device design, asymmetric y-junction mux/demux geometry dictates characteristics of its response. Primarily, with the parameters of waveguide width and angle inducing particular group velocity vectors, crosstalk contribution of one input arm on its neighboring arms can be minimized by spectrally matching low crosstalk regimes. We employ a visualization scheme of examining sufficient angles for a multimode waveguide supporting > 2 modes, in order to scale mode support using a demonstrated methodology.

In order to have broadband support for the asymmetric y-junction, we seek to have maximal regions of overlap. Slight offset in angle will shift the periodicity of low crosstalk regimes in the wavelength domain. A phase shifter can be employed to just one arm to correct for slight wavelength mismatch post-fabrication.

The experimental demonstrations presented in this dissertation motivate the capability of scaling aggregate data through multimode operation. Increasing standard data rate through the multimode waveguide and scaling the number of supported multiplexing arms are also implemented for increasing on-chip bandwidth. An entire multimode system is envisioned with the capability of routing and coupling on- and off- chip.

With our heightened understanding behind device design, we turn to analyzing the core motivators for introducing multimodal operation. In optical systems employing wavelength-division multiplexing, analysis is performed to show the clear advantage of replacing WDM channels with MDM/PDM in order to minimize electrical power consumption.

For current work in silicon photonics, the need to introduce a control plane is imperative for control of active photonic devices, especially to operate as functional units in any system, be it datacenter, optical networks, or supercomputers. In each of these cases, transferring data through optical interconnects is attractive for its high bandwidth capacity, lower power consumption, and small footprint compared to electrical interconnects. The multistage switch fabric is demonstrated in this dissertation as a programmable interface that operates at a rate of equivalent order of magnitude (10s of nanosecond) as the optical switch, with a way forward for faster control planes. A novel method to dynamically allocate power in a multi-path system while multicasting data is presented and demonstrated. The possibility of integrating the Si device with existing subsystems in need of faster response time for today's relatively larger workflows in data centers is realized.

The demand for more bandwidth pushes scaling to support currently unused bandwidth regimes, like longer wavelength. Beyond novel work in detection, more stable signal recovery is desired, and phase modulation via coherent perfect absorption on-chip is explored. As explored in this dissertation, photonic technologies can serve as drivers to push current bandwidth bottleneck to ever higher data bandwidth support on-chip.

8.2 Future Work

The current investigations present a number of extensions for future work. First, in the design of the multimode waveguide, we can continue to think along the lines of optimizing

device structure for stable, broadband operation. Some studies that have recently been conducted include [Riesen and Love, 2013], which examine tuning device parameters for optimizing specific characteristics, as well as other optimization procedures [Fu *et al.*, 2016]. Recent work in adiabatic coupling has also focused in the nonlinear domain [Mrejen *et al.*, 2014], which could be further examined for novel implementations of tight-spaced multimode guides. Moreover, a fine study on how thermal effects vary the operation in the mode mux/demux region can be extended and/or performed at this level of granularity.

We can continue to examine the power saving analysis motivating MDM operation. As performance from among a variety of MM-supporting devices tends to stabilize, on-chip system designs can take into account possible areas of improvement that can arise from using different MM structures.

Then, from a systems perspective, coupling between the multicore fiber and the multimode waveguide can be practically examined. Multi-tiered multimode waveguides are also possibilities for system implementation for keeping lateral density to a minimum. These potential areas of extension from the work presented in this dissertation will leverage scaled bandwidth with improved MM operation and allows for greater conceptualization of modal support in waveguide structure design.

Among the topics covered in this dissertation include the integration of a control plane with a photonic switch fabric. This work has room for continued development, as the control plane that is demonstrated should have the capability to take into account many parameters. As device integration with electronic platform matures, many of these complexities will likewise be modularized, out of necessity in operation. However, as a research question, we can continue to consider how to account for various physical feedback parameters in the presence of overlapping dependencies.

The final part of this dissertation examines ion implanting photodetectors to extend the wavelength absorption regime. By optimizing design of these devices for improving responsivity and rate, applications like biological and chemical sensing can more effectively be realized with long-wavelength operation. Then, with the CPA modulator, placement of the phase shifting component on-chip will allow for enhanced stability in data operation for future modes of data recovery.

These areas further the work presented in this dissertation and hold particularly exciting possibilities for exploration.

8.3 Summary

The main contribution of this dissertation maps out various routes for scaling bandwidth on-chip through spatial multiplexing. Different forms of spatial multiplexing are experimentally realized, with the inherent challenges behind such implementations analyzed. Device optimization is performed and analyzed with this gained perspective. By leveraging combinations of untapped orthogonal domains on-chip, we can realize even higher aggregate data bandwidth with the available spatial channels. We place MDM in context with existing technologies and show significant power-saving in reducing the number of lasers used for attaining equivalent bandwidth.

In order to satisfy computing demand, silicon photonics offer an industrially attainable solution for alleviating the electronic interconnect bandwidth bottleneck. Spatial multiplexing is illustrated as a rich field with the promise of making the impact of bandwidth gain through adoption of Si Ph technologies even greater. Ultra high capacity on-chip bandwidth enabled through new device technologies, coupled with system design from both a dynamical and device perspective, are leveraged for future generations of computing systems.

Bibliography

- [Abrams *et al.*, 2016] N. Abrams, D. M. Calhoun, C. P. Chen, and K. Bergman. A self-optimizing 4-channel 30 gbaud/s pam-4 packaged silicon photonics subsystem with binary driving signals. *European Conference on Optical Communications*, 2016.
- [Ackert *et al.*, 2015] J. J. Ackert, D. J. Thomson, L. Shen, A. C. Peacock, P. E. Jessop, G. T. Reed, G. Z. Mashanovich, and A. P. Knights. High-speed detection at two micrometres with monolithic silicon photodiodes. *Nature Photonics*, 9, 2015.
- [Anslow, 2013] P. Anslow. *Error performance objective for 400 GbE*. IEEE 400 Gb/s Ethernet Study Group, 2013.
- [Asakura *et al.*, 2015] H. Asakura, T. Yoshida, H. Tsuda, K. Suzuki, K. Tanizawa, M. Toyama, M. Ohtsuka, N. Yokoyama, K. Matsumaro, M. Seki, K. Koshino, K. Ikeda, S. Namiki, and H. Kawashima. A 200-ghz spacing, 17-channel, 1x22 wavelength selective switch using a silicon arrayed-waveguide grating with loopback. *Photonics in Switching*, page 52, 2015.
- [Assefa *et al.*, 2010] S. Assefa, F. Xia, and Y. A. Vlasov. Reinventing germanium avalanche photodetector for nanophotonic on-chip optical interconnects. *Nature Letters*, 464, 2010.
- [Bauters *et al.*, 2013] J. F. Bauters, M. L. Davenport, M. J. R. Heck, J. K. Doylend, A. Chen, A. W. Fang, and J. E. Bowers. Silicon on ultra-low-loss waveguide photonic integration platform. *Optics Express*, 21(1), 2013.
- [Bhattacharya, 1997] P. Bhattacharya. *Semiconductor Optoelectronic Devices*. Pearson, 1997.

- [Borrill *et al.*, 2007] J. Borrill, L. Oliker, J. Shalf, and H. Shan. Investigation of leading hpc i/o performance using a scientific-application derived benchmark. *Supercomputing*, 2007.
- [Bottacchi, 2014] S. Bottacchi. *Theory and Design of Terabit Optical Fiber Transmission Systems*. Cambridge University Press, 2014.
- [Bozinovic *et al.*, 2013] N. Bozinovic, Y. Yue, Y. Ren, M. Tur, P. Kristensen, H. Huang, A. E. Willner, and S. Ramachandran. Terabit-scale orbital angular momentum mode division multiplexing in fibers. *Science*, 340:1545–1548, 2013.
- [Calhoun *et al.*, 2016] D. M. Calhoun, Q. Li, D. Nikolova, C. P. Chen, K. Wen, S. Rumley, and K. Bergman. *Hardware-Software Integrated Silicon Photonics for Computing Systems*. 2016.
- [Cardenas *et al.*, 2008] J. Cardenas, C. B. Poitras, J. T. Robinson, K. Preston, L. Chen, and M. Lipson. Low loss etchless silicon photonic waveguides. *Optics Express*, 17(6):4752–4757, 2008.
- [Chen and Poon, 2006] H. Chen and A. W. Poon. Low-loss multimode-interference-based crossings for silicon wire waveguides. *IEEE Photonics Technology Letters*, 18(21):2260–2262, 2006.
- [Chen *et al.*, 2008] L. Chen, P. Dong, and M. Lipson. High performance germanium photodetectors integrated on submicron silicon waveguides by low temperature wafer bonding. *Optics Express*, 16(15):11513–11518, 2008.
- [Chen *et al.*, 2012] C. P. Chen, K. Padmaraju, and K. Bergman. Analyzing the effect of thermal fluctuations on silicon nanophotonics devices using finite-element simulations. *TECHCON*, 2012.
- [Chen *et al.*, 2013a] C. P. Chen, J. B. Driscoll, R. R. Grote, Y. Liu, R. M. Osgood Jr., and K. Bergman. 60-gb/s mode division multiplexing and wavelength division multiplexing in si multimode waveguides. *European Conference on Optical Communications*, 2013.

- [Chen *et al.*, 2013b] C. P. Chen, J. B. Driscoll, R. R. Grote, Y. Liu, R. M. Osgood Jr., and K. Bergman. Harnessing the properties of optical channel diversity in a multi-mode silicon nanophotonic waveguide for high-speed data. *TECHCON*, 2013.
- [Chen *et al.*, 2014a] C. P. Chen, J. B. Driscoll, R. R. Grote, B. Souhan, R. M. Osgood Jr., and K. Bergman. Mode and polarization multiplexing in a silicon photonic chip at 40gb/s aggregated data bandwidth. *IEEE Photonics Technology Letters*, 2014.
- [Chen *et al.*, 2014b] C. P. Chen, J. B. Driscoll, N. Ophir, R. R. Grote, R. M. Osgood Jr., and K. Bergman. First demonstration of polarization-multiplexing combined with on-chip mode-division multiplexing. *Optical Fiber Communications*, 2014.
- [Chen *et al.*, 2014c] C. P. Chen, J. B. Driscoll, B. Souhan, R. R. Grote, X. Zhu, R. M. Osgood Jr., and K. Bergman. Experimental demonstration of spatial scaling for high-throughput transmission through a si mode-division-multiplexing waveguide. *Integrated Photonics Research*, 2014.
- [Chen *et al.*, 2014d] C. P. Chen, X. Zhu, Y. Liu, T. Shiraishi, T. Baehr-Jones, M. Hochberg, and K. Bergman. Multicasting using a high-radix silicon photonic switch. *TECHCON*, 2014.
- [Chen *et al.*, 2015a] C. P. Chen, J. B. Driscoll, Jr R. M. Osgood, and K. Bergman. Spatial multiplexing through silicon photonic devices for high-bandwidth data transmission. *TECHCON*, 2015.
- [Chen *et al.*, 2015b] C. P. Chen, X. Zhu, Y. Liu, Q. Li, J. Chan, T. Baehr-Jones, M. Hochberg, and K. Bergman. Performing intelligent power distribution in a 4x4 silicon photonic switch fabric. *Optical Interconnects*, 2015.
- [Chen *et al.*, 2016a] C. P. Chen, J. B. Driscoll, R. M. Osgood Jr., and K. Bergman. 240 gb/s mode and wavelength division multiplexed data transmission in si photonics. *Optical Interconnects*, 2016.

- [Chen *et al.*, 2016b] C. P. Chen, B. Souhan, R. M. Osgood Jr., and K. Bergman. Thermo-optic tuning of silicon photonic multimode waveguide for post-fabrication optimization. *Frontier in Optics*, 2016.
- [Chen *et al.*, 2016c] C. P. Chen, X. Zhu, Y. Liu, M-S Chik, T. Baehr-Jones, M. Hochberg, and K. Bergman. Programmable dynamically-controlled silicon photonic switch fabric. *IEEE Journal of Lightwave Technology*, 34(12):2952–2958, 2016.
- [Chen *et al.*, 2016d] W. Chen, P. Wang, T. Yang, G. Wang, T. Dai, Y. Zhang, L. Zhou, X. Jiang, and J. Yang. Silicon three-mode (de)multiplexer based on cascaded asymmetric y-junctions. *Optics Letters*, 41(12):2851–2854, 2016.
- [Chin and Ho, 1998] M. K. Chin and S. T. Ho. Design and modeling of waveguide-coupled single-mode microring resonators. *IEEE Journal of Lightwave Technology*, 16(8):1433–1446, 1998.
- [Chong *et al.*, 2010] Y. Chong, L. Ge, H. Cao, and A. D. Stone. Coherent perfect absorbers: time-reversed lasers. *Physical Review Letters*, 105, 2010.
- [Christen *et al.*, 2009] L. Christen, O. F. Yilmaz, S. Nuccio, X. Wu, I. Fazal, A. E. Willner, C. Langrock, and M. M. Fejer. Tunable 105 ns optical delay for 80 gb/s rz-dqpsk, 40 gb/s rz-dpsk, and 40 gb/s rz-ook signals using wavelength conversion and chromatic dispersion. *Optics Letters*, 34(4), 2009.
- [cvi, 2003] *Optical Transmission Systems Engineering*. Artech House Optoelectronics Library, 2003.
- [Dai *et al.*, 2013] D. Dai, J. Wang, and S. He. Silicon multimode photonic integrated devices for on-chip mode-division-multiplexed optical interconnects. *Progress in Electromagnetics Research*, 143:773–819, 2013.
- [Dally and Towles, 2004] W. J. Dally and B. Towles. *Principles and Practices of Interconnection Networks*. Morgan Kaufmann Series in Computer Architecture and Design, 2004.

- [Daly, 2004] W. J. Daly. *Principles and Practices of Interconnection Networks*. Elsevier, 2004.
- [Dang *et al.*, 2015] D. Dang, B. Patra, and R. Mahapatra. A 2-layer laser multiplexed photonic network-on-chip. *International Symposium on Quality Electronic Design*, 2015.
- [daq,] Daqmx timing and sample rates.
- [Das, 2012] S. Das. *PAC.C: A Unified Control Architecture for Packet and Circuit Network Convergence*. PhD thesis, Stanford, 2012.
- [Ding *et al.*, 2013] Y. Ding, J. Xu, F. D. Ros, B. Huang, H. Ou, and C. Peucheret. On-chip two-mode division multiplexing using tapered directional coupler-based mode multiplexer and demultiplexer. *Optics Express*, 21(8):10376–10382, 2013.
- [Doerr *et al.*, 2010] C. R. Doerr, P. J. Winzer, Y-K. Chen, S. Chandrasekhar, M. S. Rasras, L. Chen, T-Y Liow, K-W Ang, and G-Q Lo. Monolithic polarization and phase diversity coherent receiver in silicon. *IEEE Journal of Lightwave Technology*, 28(4):520–525, 2010.
- [Driscoll *et al.*, 2013] J. B. Driscoll, R. R. Grote, B. H. Souhan, J. I. Dadap, and Jr. R. M. Osgood. Asymmetric y junctions in silicon waveguides for on-chip mode-division multiplexing. *Optics Letters*, 38(11):1854–1856, 2013.
- [Driscoll *et al.*, 2014] J. B. Driscoll, C. P. Chen, R. R. Grote, B. Souhan, J. I. Dadap, A. Stein, M. Lu, K. Bergman, and Jr. R. M. Osgood. A 60 gb/s mdm-wdm si photonic link with ≤ 0.7 db power penalty per channel. *Optics Express*, 22(15):18543–18555, 2014.
- [Dumon *et al.*, 2004] P. Dumon, W. Bogaerts, V. Wiaux, J. Wouters, S. Beckx, J. V. Campenhout, D. Taillaert, B. Luyssaert, P. Bienstman, D. V. Thourhout, and R. Baets. Low-loss soi photonic wires and ring resonators fabricated with deep uv lithography. *IEEE Photonics Technology Letters*, 16(5):1328–1330, 2004.
- [Ebrahimi, 2013] M. Ebrahimi. Fully adaptive routing algorithms and region-based approaches for two-dimensional and three-dimensional networks-on-chip. *IET Computers Digital Techniques*, 7(6), 2013.

- [Eddington and Ray,] C. Eddington and B. Ray. Multi-gigahertz fpga signal processing.
- [Fan and Ramdas, 1959] H. Y. Fan and A. K. Ramdas. Infrared absorption and photoconductivity in irradiated silicon. *Journal of Applied Physics*, 30(112):1127–1134, 1959.
- [Fu *et al.*, 2016] P-H Fu, Y-C Tu, and D-W Huang. Broadband optical waveguide couplers with arbitrary coupling ratios designed using a genetic algorithm. *Optics Express*, 24(26):30547–30561, 2016.
- [Fukuda *et al.*, 2008] H. Fukuda, K. Yamada, T. Tsuchizawa, T. Watanabe, H. Shinojima, and S i. Itabashi. Silicon photonic circuit with polarization diversity. *Optics Express*, 16(7):4872–4880, 2008.
- [Gabrielli *et al.*, 2012] L. H. Gabrielli, D. Liu, S. G. Johnson, and M. Lipson. On-chip transformation optics for multimode waveguide bends. *Nature Communications*, 10(1038), 2012.
- [Gardes *et al.*, 2005] F. Y. Gardes, G. T. Reed, and N. G. Emerson. A sub-micron depletion-type photonic modulator in silicon on insulator. *Optics Express*, 13(22), 2005.
- [Garg and Janyani, 2015] A. K. Garg and V. Janyani. Analysis of ook upstream signal remodulation for different data rates in wdm pon network. *International Journal of Signal Processing Systems*, 3(2):134–138, 2015.
- [Griffiths, 2004] D. J. Griffiths. *Introduction to Quantum Mechanics*, volume 2. Pearson, 2004.
- [Grote *et al.*, 2013a] R. R. Grote, J. B. Driscoll, and Jr. R. M. Osgood. Integrated optical modulators and switches using coherent perfect loss. *Optics Letters*, 38:3001–3004, 2013.
- [Grote *et al.*, 2013b] R. R. Grote, K. Padmaraju, B. Souhan, J. B. Driscoll, K. Bergman, and R. M. Osgood Jr. 10 gb/s error-free operation of all-silicon ion-implanted-waveguide photodiodes at 1.55 μm . *IEEE Photonics Technology Letters*, 25(1):67–70, 2013.
- [Gu *et al.*, 2009] H. Gu, K. H. Mo, J. Xu, and W. Zhang. A low-power low-cost optical router for optical networks-on-chip in multiprocessor systems-on-chip. *IEEE Computer Society Annual Symposium on VLSI*, pages 19–24, 2009.

- [Han *et al.*, 2014] S. Han, T. J. Seok, N. Quack, B-W Yoo, and M. C. Wu. Monolithic 50x50 mems silicon photonic switches with microsecond response time. *OFC*, 2014.
- [Haus, 1984] H. A. Haus. *Waves and Fields in Optoelectronics*. Prentice-Hall Series in Solid State Physical Electronics, 1984.
- [hdp, 2009] Optoelectronics. *Executive Summary*, 2009.
- [Heck *et al.*, 2011] M. J. R. Heck, H-W Chen, A. W. Fang, B. R. Koch, D. Liang, H. Park, M. N. Sysak, and J. E. Bowers. Hybrid silicon photonics for optical interconnects. *IEEE Journal of Selected Topics in Quantum Electronics*, 17(2):333–346, 2011.
- [Hui and O’Sullivan, 2009] R. Hui and M. O’Sullivan. *Fiber Optic Measurement Techniques*. Academic Press, 2009.
- [Jia *et al.*, 2012] D. Jia, H. Zhang, Z. Ji, N. Bai, and G. Li. Optical fiber amplifiers for space-division multiplexing. *Frontier Optoelectronics*, 5(4):351–357, 2012.
- [Joshi *et al.*, 2005] A. Joshi, X. Wang, D. Mohr, D. Becker, and C. Wree. Balanced photoreceivers for analog and digital fiber optic communications. *Enabling Photonics Technologies for Defense, Security, and Aerospace Applications*, 5814, 2005.
- [Kachris *et al.*, 2013] C. Kachris, K. Bergman, and I. Tomkos. *Optical interconnects for future data center networks*. Springer, 2013.
- [Keyvainia *et al.*, 2013] S. Keyvainia, G. Roelkens, D. V. Thourhout, C. Jany, A. L. Liepvre M. Lamponi, F. Lelarge, D. Make, G-H. Duan, D. Bordel, and J-M. Fedeli. Demonstration of a heterogeneously integrated iii-v/soi single wavelength tunable laser. *Optics Express*, 21(3):3784–3792, 2013.
- [Kilper *et al.*, 2011] D. C. Kilper, G. Atkinson, S. K. Korotky, S. Goyal, P. Vetter, D. Suvakovic, and O. Blume. Power trends in communication networks. *IEEE Journal of Selected Topics in Quantum Electronics*, 17(2):275–284, 2011.
- [Kim *et al.*, 2008a] J. Kim, W. J. Dally, S. Scott, and D. Abts. Technology-driven, highly-scalable dragonfly topology. *ISCA*, pages 77–88, 2008.

- [Kim *et al.*, 2008b] J. Kim, M. J. Park, M. H. Perrott, and F. X. Kartner. Photonic sub-sampling analog-to-digital conversion of microwave signals at 40-ghz with higher than 7-enob resolution. *Optics Express*, 16(21):16509–16515, 2008.
- [Kopp *et al.*, 2011] C. Kopp, S. Bernabe, B. B. Bakir, J-M Fedeli, R. Orobtcouk, F. Schrank, H. Porte, L. Zimmermann, and T. Tekin. Silicon photonic circuits: On-cmos integration, fiber optic coupling, and packaging. *IEEE Journal of Selected Topics in Quantum Electronics*, 17(3):489–509, 2011.
- [Kopp *et al.*, 2015] V. I. Kopp, J. Park, M. Wlodawski, E. Hubner, J. Singer, D. Neugroschl, A. Z. Genack, P. Dumon, J. V. Campenhout, and P. Absil. Two-dimension, 37-channel, high-bandwidth, ultra-dense silicon photonics optical interface. *Journal of Lightwave Technology*, 33(3), 2015.
- [Lee and Lipson, 2013] Y. H. Lee and M. Lipson. Back-end deposited silicon photonics for monolithic integration on cmos. *IEEE Journal of Selected Topics in Quantum Electronics*, 19(2), 2013.
- [Lee *et al.*, 2006] B. G. Lee, B. A. Small Q. Xu, M. Lipson, and K. Bergman. Transmission of high-data-rate optical signals through a micrometer-scale silicon ring resonator. *Optics Letters*, 31(18):2701–2703, 2006.
- [Li *et al.*, 2013] Z. Li, A. M. Heidt, J. M. O. Daniel, Y. Jung, S. U. Alam, , and D. J. Richardson. Thulium-doped fiber amplifier for optical communications at 2 nm. *Optics Express*, 21(8):9289–9297, 2013.
- [Li *et al.*, 2014] D. Li, M. Xu, Y. Liu, X. Xie, Y. Cui, J. Wang, and G. Chen. Reliable multicast in data center networks. *IEEE Transactions on Computers*, 63(8), 2014.
- [Lin *et al.*, 2016] T. Lin, Z. Zhou, M. Tornatore, and B. Mukherjee. Demand-aware network function placement. *IEEE Journal of Lightwave Technology*, 34(11):2590–2600, 2016.
- [Lipson, 2005] M. Lipson. Guiding, modulating, and emitting light on silicon-challenges and opportunities. *Journal of Lightwave Technology*, 23(12):4222–4238, 2005.

- [Liu *et al.*, 2007] A. Liu, L. Liao, D. Rubin, H. Nguyen, B. Ciftcioglu, Y. Chetrit, N. Izhaky, and M. Paniccia. High-speed optical modulation based on carrier depletion in a silicon waveguide. *Optics Express*, 15(2):660–668, 2007.
- [Luo *et al.*, 2012] Y. Luo, G. Li, X. Zheng, J. Yao, H. Thacker, J-H Lee, J. E. Cunningham, K. Raj, and A. V. Krishnamoorthy. Low-loss low-crosstalk silicon rib waveguide crossing with tapered multimode-interference design. *Group IV Photonics*, 2012.
- [Luo *et al.*, 2013] L-W Luo, N. Ophir, C. P. Chen, L. H. Gabrielli, C. B. Poitras, K. Bergman, and M. Lipson. Wdm-compatible mode-division multiplexing on a silicon chip. *Nature Communications*, 5(3069), 2013.
- [Marlow Industries,] Inc Marlow Industries. Technical data sheet.
- [Masood *et al.*, 2012] A. Masood, M. Pantouvaki, D. Goossens, G. Lepage, P. Verheyen, D. Van Thourhout, P. Absil, and W. Bogaerts. Cmos-compatible tungsten heaters for silicon photonic waveguides. In *Optical Interconnects IV*, 2012.
- [Masson and B. W. Jordan, 1972] G. M. Masson and Jr B. W. Jordan. Generalized multi-stage connection networks. *John Wiley Son*, pages 191–209, 1972.
- [McDonough, 2007] J. McDonough. Moving standards to 100 gbe and beyond. *IEEE Applications Practice*, 45(11):6–9, 2007.
- [Mengyuan *et al.*, 2014] Y. Mengyuan, Y. Yu, J. Zou, W. Yang, and X. Zhang. On-chip multiplexing conversion between wavelength division multiplexing-polarization division multiplexing and wavelength division multiplexing-mode division multiplexing. *Optics Letters*, 39(4):758–761, 2014.
- [Mo and Walrand, 2000] J. Mo and J. Walrand. Fair end-to-end window-based congestion control. *IEEE/ACM Transactions on Networking*, 8(5):556–567, 2000.
- [Mock, 2012] A. Mock. Low-power all-optical switch based on time-reversed microring laser. *IEEE Photonics Journal*, 4(6), 2012.
- [Moore, 1965] G. E. Moore. Cramming more components onto integrated circuits. *Electronics*, 38(8), 1965.

- [Mrejen *et al.*, 2014] M. Mrejen, H. Suchowski, T. Hatakeyama, C. Wu, L. Feng, K. O'Brien, Y. Wang, and X. Zhang. Adiabatic elimination-based coupling control in densely packed subwavelength waveguides. *Nature Communications*, 6, 2014.
- [Nabet, 2015] B. Nabet. *Photodetectors Materials, Devices, and Applications*. AASTAR, 2015.
- [Nelson *et al.*, 2001] L. E. Nelson, T. N. Nielsen, and H. Kogelnik. Observation of pmd-induced coherent crosstalk in polarization-multiplexed transmission. *IEEE Photonics Technology Letters*, 13(7):738–740, 2001.
- [Nelson *et al.*, 2014] L. E. Nelson, M. D. Feuer, K. Abedin, X. Zhou, T. F. Taunay, J. M. Fini, B. Zhu, R. Isaac, R. Harel, G. Cohen, and D. M. Marom. Spatial superchannel routing in a two-span roadm system for space division multiplexing. *IEEE Journal of Lightwave Technology*, 32(4):783–789, 2014.
- [Nishihara *et al.*, 1989] H. Nishihara, M. Haruna, and T. Suhara. *Optical Integrated Circuits*. McGraw-Hill Book Company, 1989.
- [Ophir *et al.*, 2013] N. Ophir, C. Mineo, D. Mountain, and K. Bergman. Silicon photonic microring links for high-bandwidth-density, low-power chip i/o. *IEEE Micro*, 33(1), 2013.
- [Padmaraju *et al.*, 2013] K. Padmaraju, D. F. Logan, X. Zhu, J. J. Ackert, A. P. Knight, and K. Bergman. Integrated thermal stabilization of a microring modulator. *Optical Fiber Communications*, OM2H.7, 2013.
- [Pat, 1998] *A Switching Theory*. John Wiley Sons, 1998.
- [Patterson and Hennessey, 2007] D. Patterson and J. Hennessey. *Computer Organization and Design*. Morgan Kaufman, 2007.
- [Peerlings, 2003] J. Peerlings. From loss test to fiber certification fiber characterization today part 1: Chromatic dispersion. *Agilent*, 2003.
- [Perrin, 2010] S. Perrin. *The Need for Next-Generation ROADM Networks*. Heavy Reading, 2010.

- [Pinnow *et al.*, 1973] D. A. Pinnow, T. C. Rich, F. W. Ostermayer Jr., and M. DiDomenico Jr. Fundamental optical attenuation limits in the liquid and glassy state with application to fiber optical waveguide materials. *Applied Physics Letters*, 22(10):527–529, 1973.
- [Rabaey *et al.*, 2003] J. M. Rabaey, A. P. Chandrakasan, and B. Nikolic. *Digital integrated circuits: a design perspective*. Pearson Education, 2003.
- [Ramachandran, 2005] S. Ramachandran. Dispersion-tailored few-mode fibers: A versatile platform for in-fiber photonic devices. *IEEE Journal of Lightwave Technology*, 23(11):3426–3443, 2005.
- [Rawaswami *et al.*, 2004] R. Rawaswami, K. Sivarajan, and G. H. Sasaki. *Optical Networks*, volume 3. Morgan Kaufman, 2004.
- [Reed *et al.*, 2010] G. T. Reed, G. Mashanovich, F. Gardes, and D. Thomson. Silicon optical modulators. *Nature Photonics*, 4(518), 2010.
- [Richardson *et al.*, 2013] D. J. Richardson, J. M. Fini, and L. E. Nelson. Space-division multiplexing in optical fibres. *Nature Photonics*, 7:354–362, 2013.
- [Riesen and Love, 2012] N. Riesen and J.D. Love. Design of mode-sorting asymmetric y-junctions. *Applied Optics*, 51(15):2778–2783, 2012.
- [Riesen and Love, 2013] N. Riesen and J. D. Love. Tapered velocity mode-selective couplers. *Journal of Lightwave Technology*, 31(13):2163–2169, 2013.
- [Robinson *et al.*, 2008] J. T. Robinson, K. Preston, O. Painter, and M. Lipson. First-principle derivation of gain in high-index-contrast waveguides. *Optics Express*, 16(21), 2008.
- [Rodrigues *et al.*, 2013] A. Rodrigues, S. Hemmert, D. Resnick, K. Bergman, J. Shalf B. Jacob, P. Hargrove, G. Hendry, D. Quinlan, C. Liao, and S. Yalamanchili. Data movement dominates (dmd) and codex: Codesign for exascale. *ES3 meeting*, 2013.
- [Roelkens *et al.*, 2010] G. Roelkens, L. Liu, D. Liang, R. Jones, A. Fang, B. Koch, and J. Bowers. Iii-v/silicon photonics for on-chip and inter-chip optical interconnects. *Laser Photonics Rev*, 4(6):751–779, 2010.

- [Rothenberg *et al.*, 2015] J. M. Rothenberg, C. P. Chen, J. J. Ackert, A. Ahmed, A. P. Knights, R. R. Grote, K. Bergman, and Jr. R. M. Osgood. Coherent perfect absorption in a silicon photonic ring resonator. *Frontiers in Optics*, 2015.
- [Rothenberg *et al.*, 2016] J. M. Rothenberg, C. P. Chen, J. J. Ackert, A. Ahmed, A. P. Knights, K. Bergman, R. M. Osgood Jr., and R. R. Grote. Experimental demonstration of coherent perfect absorption in a silicon photonic racetrack resonator. *Optics Letters*, 2016.
- [Saeedi *et al.*, 2015] S. Saeedi, B. Abiri, A. Hajimiri, and A. Emami. Differential optical ring modulator: Breaking the bandwidth/quality-factor trade-off. *ECOC*, 2015.
- [Saleh and Teich, 1991] B.E. Saleh and M. C. Teich. *Fundamentals of Photonics*, volume 2. Wiley, 1991.
- [Salisbury,] B. Salisbury. How to set up floodlight and test openflow rules.
- [Selvaraja *et al.*, 2014] S. K. Selvaraja, P. D. Heyn, G. Winroth, P. Ong, G. Lepage, C. Cailler, A. Rigny, K. K. Bourdelle, W. Bogaerts, D. V. Thourhout, J. V. Campenhout, and P. Absil. Highly uniform and low-loss passive silicon photonics devices using a 300mm cmos platform. *OFC*, 2014.
- [Sheng *et al.*, 2016] B. Sheng, H. Zhou, C. Tao, A. Zahid, Z. Ni, Y. Huan, R. Hong, and D. Zhang. Tunable and polarization-independent wedged resonance filter with 2d crossed grating. *IEEE Photonics Technology Letters*, 28(20), 2016.
- [Sherwood-Dros and Lipson, 2011] N. Sherwood-Dros and M. Lipson. Scalable 3d dense integration of photonics on bulk silicon. *Optics Express*, 19(18), 2011.
- [Soref and Bennett, 1987] R. A. Soref and B.R. Bennett. Electrooptical effects in silicon,” iee journal of quantum electronics. *IEEE Journal of Quantum Electronics*, QE-23:123–129, 1987.
- [Soref, 2006] R. Soref. The past, present, and future of silicon photonics. *IEEE Journal of Selected Topics in Quantum Electronics*, 12(6):1678–1687, 2006.

- [Souhan *et al.*, 2013] B. Souhan, C. P. Chen, R. R. Grote, J. B. Driscoll, N. Ophir, K. Bergman, and R. M. Osgood Jr. Error-free operation of an all-silicon waveguide photodiode at 1.9 μm . *CLEO*, 2013.
- [Souhan *et al.*, 2014] B. Souhan, R. R. Grote, C. P. Chen, H.-C. Huang, J. B. Driscoll, M. Lu, A. Stein, H. Bakhru, K. Bergman, W. M. J. Green, and Jr. R. M. Osgood. Si+-implanted si-wire waveguide photodetectors for the mid-infrared. *Optics Express*, 22(22), 2014.
- [Souhan *et al.*, 2016] B. Souhan, C. P. Chen, M. Lu, A. Stein, H. Bakhru, R. R. Grote, K. Bergman, W. M. J. Green, and Jr. R. M. Osgood. Ar+-implanted si-waveguide photodiodes for mid-infrared detection. *MDPI Photonics*, 2016.
- [Stabile and Williams, 2014] R. Stabile and K.A. Williams. Integrated space and wavelength switches. *Advanced Photonics for Communications*, PW2B.1, 2014.
- [Stabile *et al.*, 2016] R. Stabile, A. Albores-Mejia, A. Rohit, and K. A. Williams. Integrated optical switch matrices for packet data networks. *Nature Microsystems and Nanoengineering*, 2, 2016.
- [Stern *et al.*, 2015a] B. Stern, X. Zhu, C. P. Chen, L. Tzuang, J. Cardenas, K. Bergman, and M. Lipson. Integrated switch for mode-division multiplexing (mdm) and wavelength-division multiplexing (wdm). *CLEO*, 2015.
- [Stern *et al.*, 2015b] B. Stern, X. Zhu, C. P. Chen, L. Tzuang, J. Cardenas, K. Bergman, and M. Lipson. On-chip mode division multiplexing switch. *Optica*, 2(6):530–535, 2015.
- [Synopsys, 2013] Synopsys. Rsoft modeprop. *User Guide*, 12, 2013.
- [Tanabe *et al.*, 2012] K. Tanabe, K. Watanabe, and Y. Arakawa. Iii-v/si hybrid photonic devices by direct fusion bonding. *Scientific Reports*, 349, 2012.
- [Tang *et al.*, 2009] Q. Tang, S. K. S. Gupta, and G. Varsamopoulos. Energy-efficient thermal-aware task scheduling for homogeneous high-performance computing data centers: A cyber-physical approach. *IEEE Transactions on Parallel and Distributed Systems*, 19(11), 2009.

- [Thomson *et al.*, 2012] D. J. Thomson, F. Y. Gardes, J-M Fedeli, S. Zlatanovic, Y. Hu, B. P. P. Kuo, E. Myslivets, N. Alic, S. Radic, G. Z. Mashanovich, and G. T. Reed. 50-gb/s silicon optical modulator. *IEEE Photonics Technology Letters*, 24(4), 2012.
- [Uenuma and Motooka, 2009] M. Uenuma and T. Motooka. Temperature-independent silicon waveguide optical filter. *Optics Letters*, 34(5):599–601, 2009.
- [Vantrease *et al.*, 2008] D. Vantrease, R. Schreiber, M. Monchiero, M. McLaren, N. P. Jouppi, M. Fiorentino, A. Davis, N. Binkert, R. G. Beausoleil, and J. H. Ahn. Corona: System implications of emerging nanophotonic technology. *ISCA*, 2008.
- [Verge, 2013] J. Verge. Study: Data center downtime costs 7,900perminute. *NETInteractive*, 2013.
- [Viana *et al.*, 2013] C. Viana, J-L. Polleux, and C. Algani. Vcsel characterizations at the circuit- and system-level for low-cost rof applications. *IEEE Microwave Symposium*, 2013.
- [Wang and Kowalczyk, 2010] L. L. Wang and T. Kowalczyk. A versatile bias control technique for any-point locking in lithium niobate mach-zehnder modulators. *IEEE Journal of Lightwave Technology*, 28(11):1703–1706, 2010.
- [Wang *et al.*, 2015] J. Wang, Y. Xuan, M. Qi, H. Huang, Y. Li, M. Li, X. Chen, Z. Sheng, A. Wu, W. Li, X. Wang, S. Zou, and F. Gan. Broadband and fabrication-tolerant on-chip scalable mode-division multiplexing based on mode-evolution counter-tapered couplers. *Optics Letters*, 40(9):1956–1959, 2015.
- [Wang *et al.*, 2016] S. Wang, H. Wu, H. K. Tsang, and D. Dai. Monolithically integrated reconfigurable add-drop multiplexer for mode-division-multiplexing systems. *Optics Letters*, 41(22):5298–5301, 2016.
- [Watts *et al.*, 2005] M. R. Watts, M. Qi, T. Barwicz, L. Socci, P. T. Rakich, E. P. Ippen, H. I. Smith, and H. A. Haus. Towards integrated polarization diversity: Design, fabrication and characterization of integrated polarization splitters and rotators. *OFC*, 2005.

- [Wen *et al.*, 2012] Y. H. Wen, O. Kuzucu, M. Fridman, A. L. Gaeta, L-W Luo, and M. Lipson. All-optical control of an individual resonance in a silicon microresonator. *Physical Review Letters*, 108(22), 2012.
- [Wen *et al.*, 2016a] K. Wen, S. Rumley, P. Samadi, C. P. Chen, and K. Bergman. Silicon photonics in post moore’s law era: Technological and architectural implications. *IEEE Micro*, 2016.
- [Wen *et al.*, 2016b] K. Wen, P. Samadi, S. Rumley, C. P. Chen, M. Bahadori, Y. Shen, J. Wilkes, and K. Bergman. Flexfly: Enabling a reconfigurable dragonfly through silicon photonics. *Supercomputing*, 2016.
- [Winzer *et al.*, 2005] P. J. Winzer, M. Pfennigbauer, and R-J. Essiambre. Coherent crosstalk in ultradense wdm systems. *IEEE Journal of Lightwave Technology*, 23(4), 2005.
- [Xu *et al.*, 2011] L. Xu, J. Chan, A. Biberman, H. L. Lira, M. Lipson, and K. Bergman. Dpsk transmission through silicon microring switch for photonic interconnection networks. *IEEE Photonics Technology Letters*, 23(16):1103–1105, 2011.
- [Yang and Masson, 1991] Y. Yang and G. M. Masson. Nonblocking broadcast switching networks. *IEEE Transactions on Computers*, 40(9):1005–1015, 1991.
- [Yang *et al.*, 2010] M. Yang, W. M. J. Green, S. Assefa, J. V. Campenhout, B. G. Lee, C. V. Janes, F. E. Doany, C. L. Schow, J. A. Kash, and Y. A. Vlasov. Non-blocking 4x4 electro-optic silicon switch for on-chip photonic networks. *Optics Express*, 19(1):47–54, 2010.
- [Yang, 1998] Y. Yang. A class of interconnection networks for multicasting. *IEEE Transactions on Computers*, 47(8):899–906, 1998.
- [Yariv, 2002] A. Yariv. Critical coupling and its control in optical waveguide-ring resonator systems. *IEEE Photonics Technology Letters*, 14(4):483–485, 2002.
- [Yasuoka *et al.*, 2015] N. Yasuoka, M. Ishida, M. Yamaguchi, A. Uetake, T. Yamamoto, and Y. Arakawa. 1.3 um external-cavity quantum-dot comb laser for temperature control free operation. *OFC*, 2015.

- [Yok, 2011] *Yokogawa OSA User Manual*. 2011.
- [Young and Vaughan, 2009] S. A. Young and M. A. Vaughan. The retrieval of profiles of particulate extinction from cloud-aerosol lidar infrared pathfinder satellite observations (calipso) data: Algorithm description. *American Meteorological Society*, pages 1105–1119, 2009.
- [Zhu *et al.*, 2013] X. Zhu, M. Wang, K. Bergman, H. L. R. Lira, L-W Luo, and M. Lipson. Fpga controlled microring based tunable add-drop filter. *OI*, 2013.
- [Zhu *et al.*, 2015] Z. Zhu, S. Zhong, L. Chen, and K. Chen. Fully programmable and scalable optical switching fabric for petabyte data center. *Optics Express*, 23(3):3563–3571, 2015.

Appendix: List of Publications

I. Peer Reviewed Journals

1. B. Souhan, **C. P. Chen**, R. R. Grote, R. R. Grote, J. B. Driscoll, K. Bergman, R. M. Osgood, Jr., "Error Free Operation of an All-Silicon Waveguide Photodiode at 1.9 μm ," *IEEE Photonics Technology Letters*, 25.21 (Aug. 2013).
2. L. W. Luo, N. Ophir, **C. P. Chen**, L. H. Gabrieli, C. B. Poitra, K. Bergman, M. Lipson, "WDM-Compatible mode-division multiplexing on a silicon chip," *Nature Communications*, 5 (Jan. 2014).
3. J. B. Driscoll, **C. P. Chen**, R. R. Grote, B. Souhan, J. I. Dadap, A. Stein, M. Liu, K. Bergman, R. M. Osgood, Jr., "MDM and MDM-WDM transmission through a Si waveguide with power penalties < 0.7 dB/channel," *Optics Express*, 22.15, pp. 18543-18555 (Jul. 2014).
4. **C. P. Chen**, J. B. Driscoll, R. R. Grote, B. Souhan, R. M. Osgood, Jr., K. Bergman, "Mode and Polarization Multiplexing in a Silicon Photonic Chip at 40Gb/s Aggregated Data Bandwidth," *IEEE Photonics Technology Letters*, 27.1, pp. 22-25 (Sept. 2014).
5. B. Souhan, R. R. Grote, **C. P. Chen**, H.-C. Huang, J. B. Driscoll, M. Lu, A. Stein, H. Bakhru, K. Bergman, W. M. J. Green, R. M. Osgood Jr., "Si⁺-implanted Si-wire waveguide photodetectors for the mid-infrared," *Optics Express* 22.22, pp. 27415-27424 (Oct 2014).

6. B. Stern, X. Zhu, **C. P. Chen**, L. Tzuang, J. Cardenas, K. Bergman, M. Lipson, "On-chip mode-division multiplexing switch," *Optica*, 2.6, pp. 530-535 (Jun. 2015).
7. **C. P. Chen**, X. Zhu, Y. Liu, M-S Chik, T. Baehr-Jones, M. Hochberg, K. Bergman, "Programmable Dynamically-Controlled Silicon Photonic Switch Fabric," *IEEE Journal of Lightwave Technology*, (Dec. 2015, Optical Interconnect Special Issue).
8. J. M. Rothenberg*, **C. P. Chen***, J. J. Ackert, A. Ahmed, A. P. Knights, K. Bergman, R. M. Osgood, Jr., R. R. Grote, "Experimental Demonstration of Coherent Perfect Absorption in a Silicon Photonic Racetrack Resonator," *Optics Letters*, 41.11, pp. 2537-2540 (Jun. 2016) [*First Authorship shared].
9. B. Souhan, **C. P. Chen**, M. Lu, A. Stein, H. Bakhru, R. R. Grote, K. Bergman, W. M. J. Green, and R. M. Osgood, Jr., "Ar+-implanted Si-waveguide photodiodes for mid-infrared detection," *MDPI* (Jul. 2016).

II. Conference Proceedings

1. **C. P. Chen**, K. Padmaraju, K. Bergman, "Analyzing the Effect of Thermal Fluctuations on Silicon Nanophotonic Devices using Finite-Element Simulations," Semiconductor Research Corporation (SRC) Techcon 2012, (poster, Sept. 2012).
2. B. Souhan*, **C. P. Chen***, R. R. Grote, J. B. Driscoll, N. Ophir, K. Bergman, R. M. Osgood, Jr., "Error-Free Operation of an All-Silicon Waveguide Photodiode at 1.9 μm ," CLEO 2013 CTh3L.4 (presented, Jun. 2013). [*First Authorship shared].
3. **C. P. Chen**, J. B. Driscoll, R. R. Grote, Y. Liu, R. M. Osgood, Jr., K. Bergman, "60-Gb/s Mode Division Multiplexing and Wavelength Division Multiplexing in Si Multi-mode Waveguides," European Conference on Optical Communications (ECOC) 2013 P.2.2

(poster, Sept. 2013).

4. **C. P. Chen**, J. B. Driscoll, R. R. Grote, Y. Liu, R. M. Osgood, Jr., K. Bergman, "Harnessing the Properties of Optical Channel Diversity in a Multi-mode Silicon Nanophotonic Waveguide for High-Speed Data," Semiconductor Research Corporation (SRC) Techcon 2013, (presented, Sept. 2013).

5. **C. P. Chen**, J. B. Driscoll, N. Ophir, R. R. Grote, R. M. Osgood, Jr., K. Bergman, "First Demonstration of Polarization-Multiplexing Combined with On-Chip Mode-Division Multiplexing," Optical Fiber Communication (OFC) 2014 Th4A.3 (presented, Mar. 2014).

6. L. W. Luo, N. Ophir, **C. P. Chen**, L. H. Gabrieli, C. B. Poitra, K. Bergman, M. Lipson, "On-Chip Mode Transformation using Mode-Selective Microring Resonators," International Conference on Metamaterials Photonic Crystals and Plasmonics (Meta 2014). (May 2014).

7. **C. P. Chen**, J. B. Driscoll, B. Souhan, R. R. Grote, X. Zhu, R. M. Osgood, Jr., K. Bergman, "Experimental Demonstration of Spatial Scaling for High-Throughput Transmission Through a Si Mode-Division-Multiplexing Waveguide," Integrated Photonics Research (IPR) 2014 (presented, Jul. 2014).

8. **C. P. Chen**, X. Zhu, Y. Liu, T. Shiraishi, T. Baehr-Jones, M. Hochberg, K. Bergman, "Multicasting Using a High-Radix Silicon Photonic Switch," Semiconductor Research Corporation (SRC) Techcon 2014, (presented, Sept. 2014).

9. R. M. Osgood Jr., J. B. Driscoll, **C. P. Chen**, R. R. Grote, B. E. Souhan, J. I. Dadap, A. Stein, M. Lu, K. Bergman, "Devices and system measurements of mode- and wavelength-division multiplexing in the Si wire platform," SPIE Photonics West (Feb. 2015).

10. **C. P. Chen**, X. Zhu, Y. Liu, Q. Li, J. Chan, T. Baehr-Jones, M. Hochberg, K. Bergman, "Performing Intelligent Power Distribution in a 4x4 Silicon Photonic Switch Fabric," Opti-

cal Interconnects (OI) 2015 (presented, Apr. 2015).

11. M. Bahadori, D. Nikolova, S. Rumley, **C. P. Chen**, K. Bergman, "Optimization of Microring-based Filters for Dense WDM Silicon Photonic Interconnects," IEEE Optical Interconnects Conference (Apr. 2015).

12. B. Stern, X. Zhu, **C. P. Chen**, L. Tzuang, J. Cardenas, K. Bergman, M. Lipson, "Integrated Switch for Mode-Division Multiplexing (MDM) and Wavelength-Division Multiplexing (WDM)," CLEO 2015 STh1F.2 (May 2015).

13. **C. P. Chen**, J. B. Driscoll, R. M. Osgood, Jr., K. Bergman, "Spatial Multiplexing through Silicon Photonic Devices for High-Bandwidth Data Transmission," [Best in Session: Process & Design for Extreme Energy Efficient Computing], Semiconductor Research Corporation (SRC) Techcon 2015, (presented, Sept. 2015).

14. J. M. Rothenberg*, **C. P. Chen***, J. J. Ackert, A. Ahmed, A. P. Knights, R. R. Grote, K. Bergman, R. M. Osgood, Jr., "Coherent Perfect Absorption in a Silicon Photonic Ring Resonator," Frontiers in Optics (FiO) 2015 (Oct. 2015) [*First Authorship shared].

15. **C. P. Chen**, J. B. Driscoll, R. M. Osgood, Jr., K. Bergman, "240 Gb/s Mode and Wavelength Division Multiplexed Data Transmission in Si Photonics," Optical Interconnects (OI) 2016, (presented, May 2016).

16. **C. P. Chen**, J. B. Driscoll, B. Souhan, R. M. Osgood, Jr., and K. Bergman, "Spatially-Multiplexed Data in Silicon Photonics," [Best Talk, Telecommunications], International OSA Network of Students (IONS) (presented, May 2016).

17. N. C. Abrams, D. M. Calhoun, **C. P. Chen**, and K. Bergman, "A Self-Optimizing 4-Channel 30 GBaud/s PAM-4 Packaged Silicon Photonics Subsystem with Binary Driving Signals," European Conference on Optical Communications (ECOC) (Sept. 2016).

18. **C. P. Chen**, B. Souhan, R. M. Osgood, Jr., and K. Bergman, "Thermo-optic Tuning of Silicon Photonic Multimode Waveguide for Post-Fabrication Optimization," *Frontier in Optics (FiO)* 2016, (poster, Oct. 2016).
19. K. Wen, P. Samadi, S. Rumley, **C. P. Chen**, Y. Shen, M. Bahadori, J. Wilke, and K. Bergman, "Flexfly: Enabling a Reconfiguration Dragonfly through Silicon Photonics," [Best Student Paper], *IEEE Supercomputing Conference* (Nov. 2016).
20. K. Wen, S. Rumley, P. Samadi, **C. P. Chen**, K. Bergman, "Silicon Photonics in Post Moore's Law Era: Technological and Architectural Implications," *IEEE Micro* (Nov. 2016).

III. Book Chapters

1. D. M. Calhoun, Q. Li, D. Nikolova, **C. P. Chen**, K. Wen, S. Rumley, K. Bergman, "Hardware-Software Integrated Silicon Photonics for Computing Systems [Book Chapter]," *Silicon Photonics III of the series Topics in Applied Physics*, 122, pp. 157-189 (Jan. 2016).